

Titre: Mode Composite Waveguide for 5G and Future Wireless
Communication Systems

Auteur: Jiapin Guo

Date: 2018

Type: Mémoire ou thèse / Dissertation or Thesis

Référence: Guo, J. (2018). Mode Composite Waveguide for 5G and Future Wireless
Communication Systems [Thèse de doctorat, École Polytechnique de Montréal].
Citation: PolyPublie. <https://publications.polymtl.ca/3159/>

 **Document en libre accès dans PolyPublie**
Open Access document in PolyPublie

URL de PolyPublie: <https://publications.polymtl.ca/3159/>
PolyPublie URL:

**Directeurs de
recherche:** Ke Wu
Advisors:

Programme: génie électrique
Program:

UNIVERSITÉ DE MONTRÉAL

MODE COMPOSITE WAVEGUIDE FOR 5G AND FUTURE WIRELESS
COMMUNICATION SYSTEMS

JIAPIN GUO

DÉPARTEMENT DE GÉNIE ÉLECTRIQUE
ÉCOLE POLYTECHNIQUE DE MONTRÉAL

THÈSE PRÉSENTÉE EN VUE DE L'OBTENTION
DU DIPLÔME DE PHILOSOPHIAE DOCTOR
(GÉNIE ÉLECTRIQUE)

JUIN 2018

UNIVERSITÉ DE MONTRÉAL

ÉCOLE POLYTECHNIQUE DE MONTRÉAL

Cette thèse intitulée :

MODE COMPOSITE WAVEGUIDE FOR 5G AND FUTURE WIRELESS
COMMUNICATION SYSTEMS

présentée par : GUO Jiapin

en vue de l'obtention du diplôme de : Philosophiae Doctor

a été dûment acceptée par le jury d'examen constitué de :

M. NERGUIZIAN Chahé, Ph. D., président

M. WU Ke, Ph. D., membre et directeur de recherche

M. AKYEL Cevdet, Ph. D., membre

M. KOUKI Ammar, Ph. D., membre externe

DEDICATION

To my wife Shiyu Cai

To my daughter Anna Xinyan Guo

To my parents and my brother

ACKNOWLEDGEMENTS

I would like to thank my PhD research director, Prof. Ke Wu for giving me this opportunity to pursue my PhD study at Ecole Polytechnique de Montreal in Canada. His guidance helped me to understand and think of solutions for the challenges in the 5G and future wireless communication.

I would like to thank the technical personnel Mr. Jules Gauthier, Mr. Traian Antonescu, Mr. Steve Dube and Mr. Maxime Thibault in Poly-Grames Research Centre for the help in fabrication and measurement of the prototypes.

I would like to thank Mr. Jean-Sébastien Décarie for the assistance of software problems, also Mrs. Rachel Lortie and Mrs. Nathalie Lévesque for the administrative procedures of the department.

I would like to thank Dr. Tarek Djerafi, Dr. Fang Zhu and Dr. Jianfeng Gu for the valuable discussions and helpful suggestions during my struggles in the PhD study, and Dr. Pascal Burasa for helping me with the French translation of the abstract.

I would like to thank my friends Kuangda Wang, Yangping Zhao, Lianfeng zou, Shabnam Ladan, Jaber Moghaddasi, Ajay Babu Guntupalli, Yifan Yin, Wencui Zhu, Xiaoqiang Gu, Desong Wang, etc., who made my stay at Ecole Polytechnique de Montreal memorable.

I would like to thank my father Jian Guo and mother Bin Xu, who taught me a lot and supported my decision at every stage of my life and encouraged me to pursue PhD degree in Canada.

Last but most importantly, my heart-felt gratitude goes to my wife Shiyu Cai and my daughter Anna Xinyan Guo, who have accompanied me through my PhD study. I would like to thank my wife for her enduring love and support during the highs and lows of the past several years. Without her encouragements all along, I may not achieve what I have today.

RÉSUMÉ

Dans les systèmes de communication sans fil modernes, les fonctionnalités haut-débit et multi-bande des circuits RF et micro-ondes sont de plus en plus requises dans des systèmes intégrés et compacts. La bande de fréquence actuellement utilisée pour les communications sans fil commerciales comprend les bandes aux alentours de 900 MHz, 1,9 GHz, 2,45 GHz, 3,5 GHz et 5,8 GHz pour la téléphonie mobile, l'Internet sans fil et la connectivité des capteurs. Les nouvelles bandes millimétriques comme la bande de fréquence V (57-66 GHz) et la bande E (71-76 GHz et 81-86 GHz) sont utilisées pour la connectivité des microcellules et du cœur du réseau.

Le nouveau standard des communications sans fils 5G nécessite l'exploitation parallèle de bandes de fréquences, à savoir les basses et les hautes fréquences, permettant ainsi d'aller au-delà de la capacité des systèmes de communications actuels. D'une part, la demande croissante pour un meilleur débit de données nécessite une bande de fréquence beaucoup plus large, ce qui justifie le recours vers la bande de fréquences millimétriques. D'autre part, le standard LTE ainsi que les autres systèmes de communication à grande couverture doivent être développés de manière compatible avec les bandes de fréquences en bas de 6 GHz et celles qui sont au-delà de 6 GHz. Par conséquent, la mise au point de nouveaux systèmes intégrés et à bas coût capables d'opérer sur fréquences UHF et millimétriques s'avère essentielle pour le standard sans fil émergent (5G).

Dans cette thèse, une nouvelle méthode de conception de circuits intégrés RF large bande et multi-bande, appelée guide d'ondes à modes composites (MCW), est proposée et étudiée. Le MCW est constitué d'une structure à double guide d'ondes interne et externe, où la structure externe agit comme une ligne coaxiale rectangulaire adaptée pour les basses fréquences, tandis que la structure interne fonctionne comme un guide d'onde rectangulaire pour les hautes fréquences, ce qui rend la structure plus simple, plus compacte et à faibles pertes d'insertion. Le MCW est susceptible de propager des signaux au sein du guide d'ondes interne suivant le mode TE_{10} et/ou au sein du guide d'onde externe avec le mode TEM en fonction de la fréquence, permettant ainsi d'aboutir à des performances optimales pour les deux bandes de fréquences (basse et haute). Pour ce faire, les paramètres fondamentaux du guide d'ondes et les modes d'ordre supérieur du MCW sont théoriquement étudiés. Des équations pour les constantes de propagation, les impédances, les pertes et les fréquences de coupure du mode supérieur des guides d'ondes interne et externe du MCW sont calculés.

Les prototypes MCW sont fabriqués au sein de notre centre de recherches Poly-Grames en utilisant la technique des circuits intégrés multicouches (3 couches). Les règles de conception MCW, commençant par le choix du substrat (la permittivité et l'épaisseur), le calcul des dimensions ainsi que les bandes de fréquences d'opération, sont étudiés en détail. Cependant, ce concept MCW n'est pas limité seulement à la technique du guide d'onde intégré au substrat (GIS), mais il peut également être mis en œuvre en utilisant d'autres technologies telles que LTCC, CMOS et l'impression 3D. Deux types de réseaux d'alimentation (à savoir le type I et le type II) sont d'abord conçus pour les mesures et l'intégration du MCW avec d'autres circuits planaires. Dans les deux cas, les réseaux d'alimentation MCW multicouches sont transférés sur des lignes micro-rubans standards, ce qui est pratique pour les mesures.

En utilisant ces réseaux d'alimentation, divers circuits multicouches basés sur le MCW sont développés grâce à l'exploitation de ses différentes propriétés. Un coupleur directionnel MCW à 10 GHz est développé, où la conversion des modes en relation avec le couplage de puissance du guide d'ondes interne et externe est étudiée. Le principe de fonctionnement du coupleur est théoriquement analysé pour obtenir les équations régissant le comportement des ondes aux différents ports du coupleur.

Un filtre MCW bi-mode à 10 GHz utilisant le guide d'ondes interne comme alimentation d'entrée-sortie, et le guide d'onde externe comme résonateur, est également développé. Les deux modes dégénérés dans le résonateur à guide d'ondes externe sont utilisés pour le fonctionnement du filtre bi-mode, ce qui aboutit à deux pôles de transmission et un zéro de transmission finie.

Un T magique planaire est également développé à 10 GHz en se basant sur la technique MCW, utilisant le guide d'ondes interne comme port de sommation et le guide d'onde externe comme port de soustraction du T magique. Le signal du guide d'onde externe est divisé équitablement mais en opposition de phase entre les deux ports de sortie, tandis que le signal du guide d'onde interne est couplé avec la même phase aux deux ports de sortie.

Grâce à la géométrie et la symétrie des modes du MCW, un guide d'onde composite demi-mode (HMCW) est également proposé et étudié. Comme le MCW, le HMCW dispose également d'un guide d'ondes interne et externe, dont chacun fonctionne en demi-mode. Dans la structure HMCW, le signal se propage dans le guide d'ondes interne avec le mode quasi-TE_{0.5-0} et tout au long du guide d'onde externe avec le mode quasi-TEM. Comparé au MCW, le HMCW n'occupe que la

moitié de l'espace requis, en ayant une performance comparable en termes de perte d'insertion. Un réseau d'alimentation pour le HMCW est également développé dans le but de simplifier les mesures et l'intégration, où les deux guides d'ondes (interne et externe) sont transférés à des lignes micro-ruban à une seule couche.

ABSTRACT

In modern wireless communication systems, broadband and multiband functionalities of RF and microwave circuits are often required in a highly integrated and geometrically compact front-end systems. The currently used frequency band for commercial wireless communication includes the lower bands of 900 MHz, 1.9 GHz, 2.45 GHz, 3.5 GHz and 5.8 GHz for mobile phone, wireless internet and sensor connectivity, as well as the emerging millimeter-wave (mmW) bands of V-band (57-66 GHz) and E-band (71-76 GHz and 81-86 GHz) for small cell and backhaul connectivity. The emerging 5G wireless communication system requires the deployment of both low- and high-dual frequency bands in a simultaneous manner, which should extend far beyond the capability of existing mobile communication systems. On one hand, the increasing demand for higher speed wireless data transmission requires a much larger bandwidth, where the mmW bands shall be exploited to accommodate such a bandwidth increase. On the other hand, the LTE and other long-ranged wireless platforms need to be developed in a backwards-compatible way, and it is also very important to accommodate the frequency bands below 6 GHz or sub-6-GHz frequency ranges. Therefore, the development of a low-cost and integrated hardware solution is essential for the 5G and future wireless communication systems, which should be able to support the emerging wireless deployments over an unprecedented wide UHF-to-mmW frequency range.

In this thesis, the development of a broadband or multi-band hardware design platform or building technology, called mode composite waveguide (MCW), is proposed and addressed. The MCW consists of inner and outer wave-guiding duo structures, where the outer structure acts as a rectangular coaxial line suitable for lower frequency operation for its compact size, while the inner structure works as a rectangular waveguide suitable for higher frequency operation thanks to its simple structure and low loss. The MCW can propagate signals in the inner waveguide with TE_{10} mode and/or the outer waveguide with TEM mode depending on frequency to achieve optimal performance for both low and high frequency operations.

To begin with, the fundamental waveguide parameters and higher order modes of MCW are theoretically analyzed. Equations for propagation constants, impedances, losses, and higher order mode cutoff frequencies of both the inner and outer waveguides of MCW are provided respectively. The MCW prototypes are fabricated on three layers of substrates using the multilayer substrate integration techniques in our Poly-Grames Research Center. The MCW design rules, from the

substrate selection such as permittivity and thickness to the choice of MCW dimensions and operation frequency bands, are discussed in detail. However, this MCW concept is not only limited to the substrate integration technique, and other technologies such as LTCC, RF CMOS and 3D printing can also be used for implementation.

Two types of joint feeding networks (namely type I and type II) are first developed for MCW measurement and integration with other planar circuits. In both cases, the multilayer MCWs are transitioned to single layer microstrip lines, which are convenient for measurements. Using these joint feeding networks, various multilayer circuits based on the MCW are developed through the exploitation of its different properties. A MCW directional coupler at 10 GHz is developed, where the mode conversion regarding the inner and outer waveguide power coupling is studied. The operation principle of the coupler is mathematically formulated in achieving the required power summation and cancellation. A MCW based dual-mode filter at 10 GHz is developed, which uses the inner waveguide as the input and output feedings, and the outer waveguide as the dual-mode resonator. The two degenerate modes in the outer waveguide resonator are used for the dual-mode filter operation, which generates two transmission poles and one finite transmission zero. A MCW based planar magic tee at 10 GHz is also developed, which uses the inner waveguide as the summation port and the outer waveguide as the difference port for the magic tee operation. The outer waveguide signal is equally divided and goes into the two output ports out of phase, while the inner waveguide signal is coupled to the two output ports in phase through the two slots on the middle layer.

Taking advantages of the geometrical and mode symmetry of MCW, a half-mode composite waveguide (HMCW) is also proposed and studied. Like the MCW, the HMCW also has an inner and outer waveguide, each working in its half-mode operation, respectively. In the HMCW structure, the signal propagates in the inner waveguide with quasi- $TE_{0.5-0}$ mode and in the outer waveguide with quasi-TEM mode. Compared to its full-size counterpart, the HMCW only occupies half the space, while exhibits a comparable transmission loss performance. A joint feeding network for the HMCW is also developed for measurement and integration, where both the inner and outer waveguides are transitioned to single layer microstrip lines.

TABLE OF CONTENTS

DEDICATION	III
ACKNOWLEDGEMENTS	IV
RÉSUMÉ.....	V
ABSTRACT	VIII
LIST OF TABLES	XIII
LIST OF FIGURES.....	XIV
LIST OF SYMBOLS AND ABBREVIATIONS.....	XX
CHAPTER 1 INTRODUCTION.....	1
1.1 Background and Motivation.....	1
1.1.1 Rectangular Waveguide and Substrate Integrated Waveguide	1
1.1.2 Coaxial Line and Substrate Integrated Coaxial Line	2
1.1.3 Mode Composite Waveguide	3
1.2 Outline of thesis	5
CHAPTER 2 THEORETICAL ANALYSIS AND FABRICATION PROCESS.....	7
2.1 Theoretical Analysis of Mode Composite Waveguide	7
2.1.1 Outer Waveguide Parameters.....	7
2.1.2 Inner Waveguide Parameters	10
2.2 Parametric Study of Mode Composite Waveguide	11
2.2.1 Impedance Parametric Study.....	11
2.2.2 Loss Parametric Study.....	13
2.3 Higher Order Mode Analysis	16
2.3.1 Higher Order Mode Cutoff Frequency.....	17
2.3.2 Monomode Frequency Region	20

2.4	Fabrication of Mode Composite Waveguide	21
2.5	Dimension of Mode Composite Waveguide	23
2.6	Conclusion.....	24
CHAPTER 3 JOINT FEEDING NETWORK OF MODE COMPOSITE WAVEGUIDE.....		25
3.1	Outer Waveguide Feeding Network.....	25
3.2	Inner Waveguide Feeding Network	28
3.3	Type I MCW Joint Feeding Network.....	30
3.3.1	Feeding Network Design.....	30
3.3.3	Fabrication and Measurement	32
3.4	Type II MCW Joint Feeding Network	36
3.4.1	Feeding Network Design.....	36
3.4.2	Fabrication and Measurement	39
3.5	Conclusion.....	43
CHAPTER 4 MODE COMPOSITE WAVEGUIDE CIRCUITS.....		44
4.1	MCW Directional Coupler	45
4.1.1	Coupler Operation Principle.....	46
4.1.2	Coupler Analysis and Design.....	47
4.1.3	Fabrication and Measurement	52
4.2	MCW Dual-Mode Filter.....	54
4.2.1	Dual-Mode Filter Design	55
4.2.2	Fabrication and Measurement	61
4.4	MCW Magic Tee.....	63
4.4.1	Magic Tee Analysis and Design.....	64
4.4.2	Fabrication and Measurement	67

4.5	Conclusion.....	70
CHAPTER 5 HALF-MODE COMPOSITE WAVEGUIDE		72
5.1	HMCW Theoretical Analysis.....	72
5.2	HMCW Parametric Study	74
5.3	Joint Feeding Network Design.....	82
5.4	Fabrication and Measurement	86
5.5	Conclusion.....	90
CHAPTER 6 MULTILAYER CIRCUIT AND ANTENNA		91
6.1	Variable Propagation Constant Directional Coupler.....	91
6.1.1	Coupler Operation Principle.....	91
6.1.2	Coupler Analysis and Design.....	93
6.1.3	Fabrication and Measurement	96
6.2	Balanced Antipodal Linear Tapered Slot Antenna	99
6.2.1	Balanced ALTSA Design.....	100
6.2.2	Integrated Feeding Network Design	103
6.2.3	Fabrication and Measurement	106
6.3	Conclusion.....	108
CHAPTER 7 CONCLUSION AND FUTURE WORK.....		110
7.1	Conclusion.....	110
7.2	Future Work	112
REFERENCES.....		114

LIST OF TABLES

Table 1.1: Comparison of different types of waveguides and transmission lines.....	4
Table 2.1: Comparison of outer waveguide higher order mode cutoff frequencies.....	19
Table 4.1: Design parameters of MCW forward and backward directional couplers.....	48
Table 4.2: Dimensions of type I and type II dual-mode filters.	58
Table 5.1: Comparison of HMCW, waveguides and transmission lines.	74
Table 6.1: Forward and backward directional coupler design parameters.....	95
Table 6.2: Dimensions of balanced ALTSA.	102
Table 6.3: Dimensions of CPW to double layer SIW transition.	105

LIST OF FIGURES

Figure 1.1: 3D illustration of SIW.	2
Figure 1.2: 3D illustration of SICL.	3
Figure 1.3: (a) 3D illustration of MCW, the E and H field distributions of its two fundamental modes: (b) TEM mode in outer waveguide, (c) TE ₁₀ mode in inner waveguide.	4
Figure 2.1: Outer and inner waveguides of MCW and their fundamental modes: (a) TEM mode in outer waveguide, (b) TE ₁₀ mode in inner waveguide.....	7
Figure 2.2: Unit length capacitance distribution in a thin rectangular coaxial line.	9
Figure 2.3: Dimensions of the inner and outer waveguides of MCW.....	11
Figure 2.4: Simulated impedance of the inner and outer waveguides at different width and permittivity (Z_{in} inner waveguide impedance and Z_{out} outer waveguide impedance).	12
Figure 2.5: Simulated impedance of the inner and outer waveguides at different height and permittivity (inner waveguide impedance Z_{in} and outer waveguide impedance Z_{out}).	13
Figure 2.6: Calculated dielectric and conductor losses of inner and outer waveguides of MCW at different widths (RT/duroid 6002, $\epsilon_r=2.94$, $h=0.508$ mm at 50 GHz).	14
Figure 2.7: Calculated dielectric and conductor losses of both inner and outer waveguides at different frequencies (RT/duroid 6002, $\epsilon_r=2.94$, $h=0.508$ mm, $w=2.54$ mm).....	15
Figure 2.8: Fundamental and higher order modes E field distributions of outer waveguide (a) fundamental mode, (b) folded TE ₂₀ I, (c) folded TE ₂₀ II, (d) folded TE ₄₀ I, (e) folded TE ₄₀ II.	16
Figure 2.9: Simulated dispersion diagram of outer waveguide, including the fundamental TEM mode and first four higher order modes (RT/duroid 6002, $\epsilon_r=2.94$, $w=2.54$ mm, $h=0.508$ mm).	17
Figure 2.10: Outer waveguide cross section and its equivalent circuit for TRM.....	18
Figure 2.11: Calculated monomode regions for the inner and outer waveguides at different width.	21
Figure 2.12: Fabrication process of the substrate integrated MCW.....	22

Figure 2.13: 3D view and dimensions of substrate integrated MCW.	23
Figure 3.1: 3D view, dimensions of microstrip line to outer waveguide transition in back-to-back setup, and the E field distributions and impedances at each denoted position.....	26
Figure 3.2: Pictures of the front side (a) and back side (b) of the fabricated MCW with microstrip to outer waveguide transition.	27
Figure 3.3: Simulated and measured S-parameters of the back-to-back microstrip line to outer waveguide transition.	27
Figure 3.4: 3D view and dimensions of the microstrip line to inner waveguide transition.	28
Figure 3.5: Pictures of the front side (a) and back side (b) of the fabricated microstrip to inner waveguide transition.	29
Figure 3.6: Simulated and measured S-parameters of the back-to-back microstrip line to inner waveguide transition.	29
Figure 3.7: 3D view and dimensions of type I MCW joint feeding network.....	31
Figure 3.8: Pictures of the front side (a) and back side (b) of the fabricated MCW.....	32
Figure 3.9: MCW four-port back-to-back measurement setup	33
Figure 3.10: Simulated E field distribution at 9 GHz (top), and simulated and measured S-parameters of the type I MCW joint feeding network for low frequency operation (bottom).	34
Figure 3.11: Simulated E field distribution at 33 GHz (top), and simulated and measured S-parameters of the type I MCW joint feeding network for high frequency operation (bottom).	35
Figure 3.12: 3D view and dimensions of the type II joint feeding network.	37
Figure 3.13: Fundamental modes of the inner (a) and outer (b) waveguides, and the first two higher order modes of the outer waveguide (c) and (d).	38
Figure 3.14: Pictures of front (a) and back (b) of the fabricated joint feeding network.	40

Figure 3.15: Simulated E field distribution at 9 GHz (top), and simulated and measured S-parameters of the type II MCW joint feeding network for low frequency operation (bottom).	41
Figure 3.16: Simulated E field distribution at 19 GHz (top), and simulated and measured S-parameters of the type II MCW joint feeding network for high frequency operation (bottom).	42
Figure 4.1: Two fundamental propagating modes in the MCW: (a) TE ₁₀ mode in inner waveguide and (b) TEM mode in outer waveguide.	44
Figure 4.2: Dispersion diagram of the outer and inner waveguides of MCW.	45
Figure 4.3: Diagram of a general two-hole directional coupler.	46
Figure 4.4: Dimensions of MCW backward directional coupler and its joint feeding network. ...	50
Figure 4.5: Simulated coupling power levels at different diameters of the circular slot at 10 GHz.	51
Figure 4.6: Simulated feeding network transmission loss of the outer waveguide's fundamental and higher order modes.....	51
Figure 4.7: Pictures of fabricated MCW backward directional coupler: (a) top view, (b) bottom view.	52
Figure 4.8: Comparison of measured and simulated MCW backward directional coupler return loss (S ₁₁) and insertion loss (S ₂₁).	53
Figure 4.9: Comparison of measured and simulated MCW backward directional coupler isolation (S ₃₁) and coupling (S ₄₁).	54
Figure 4.10: Fundamental modes of the inner (a) and outer (b) waveguides, and the first two higher order modes of the outer waveguide (c) and (d).	55
Figure 4.11: Simulated E-field distributions of the folded TE ₂₀₂ I mode (a) and folded TE ₂₀₂ II mode (b) in the dual-mode resonator.	56
Figure 4.12: 3D view and dimensions of MCW based dual-mode filter and its corresponding resonator coupling scheme.	57

Figure 4.13: Simulated S21 of type I filter, exhibiting its left transmission zero location at different slot offset.	59
Figure 4.14: Simulated S21 of type II filter, exhibiting its right transmission zero location at different slot offset.	60
Figure 4.15: Simulated S-parameters of type I and type II dual-mode filters.....	61
Figure 4.16: Pictures of the fabricated type I dual-mode filter: front side view (a) and back side view (b).	62
Figure 4.17: Simulated and measured S-parameters of fabricated type I dual-mode filter.	62
Figure 4.18: E-field transformation of outer ((a)->(c)->(e)) and inner ((b)->(d)->(f)) waveguides at magic tee junction.	63
Figure 4.19: 3D view and dimensions of the MCW magic tee.	65
Figure 4.20: Pictures of the front side (a) and back side (b) of the fabricated MCW magic tee. ...	68
Figure 4.21: Simulated and measured S-parameters at the difference port P ₁ of the magic tee. ...	69
Figure 4.22: Simulated and measured S-parameters at the summation port P ₂ of the magic tee...	69
Figure 5.1: Cross section view and basic mode profile of HMCW and MCW structures with modes propagating in the inner and outer waveguides: (a) quasi-TEM mode, (b) TEM mode, (c) quasi-TE _{0.5,0} mode, (d) TE ₁₀ mode.	73
Figure 5.2: Dimensions of the HMCW inner and outer waveguides, where the distance between the inner and outer conductors is kept the same.....	75
Figure 5.3: Comparison of calculated and simulated fringe effect of the outer waveguide at different width to height ratio.	77
Figure 5.4: Comparison of calculated and simulated fringe effect of the outer waveguide at different relative permittivity.	78
Figure 5.5: Comparison of simulated HMCW and MCW inner and outer waveguide impedances versus normalized width.....	78
Figure 5.6: Comparison of simulated HMCW and MCW inner and outer waveguide losses as a function of frequency.	79

Figure 5.7: Field distribution of the 1 st higher order mode of the HMCW outer waveguide and comparison of simulated outer waveguide dispersion diagram of the HMCW and the MCW.	80
Figure 5.8: Field distribution of the 1 st higher order mode of the HMCW inner waveguide and comparison of simulated inner waveguide dispersion diagram of the HMCW and the MCW.	81
Figure 5.9 : 3D, cross-sectional and top views of the HMCW joint feeding network.	83
Figure 5.10: Mode transformation of a two-stage dual taper structure of the HMCW outer waveguide feeding network with E field distribution at each denoted position.	84
Figure 5.11: Mode transformation of a super compact right angle bend of the HMCW inner waveguide feeding network with E field distribution.	85
Figure 5.12: Pictures of fabricated HMCW joint feeding network front side (a) and back side (b).	87
Figure 5.13: E field distribution in the outer waveguide at 9 GHz, and simulated and measured S-parameters of the back-to-back HMCW joint feeding network for low frequency operation.	88
Figure 5.14: E field distribution in the inner waveguide at 25 GHz, and simulated and measured S-parameters of the back-to-back HMCW joint feeding network for high frequency operation.	89
Figure 6.1: 3D view and dimensions of the proposed directional coupler (a) 3D view, (b) top view, (c) bottom view.	94
Figure 6.2: Pictures of fabricated forward and backward directional couplers: (a-b) top and bottom view of forward directional coupler, (c-d) top and bottom view of backward directional coupler.	96
Figure 6.3: Measured and simulated forward directional coupler: (a) return loss (S11) and insertion loss (S21), (b) isolation (S31) and coupling (S41).	97
Figure 6.4: Measured and simulated backward directional coupler: (a) return loss (S11) and insertion loss (S21), (b) isolation (S31) and coupling (S41).	98

Figure 6.5: E-field distribution at the cross section: (a) conventional ALTSA, (b) balanced ALTSA.	101
Figure 6.6: Top and 3D view of the proposed balanced ALTSA.	101
Figure 6.7: Simulated radiation patterns and cross-polarizations of conventional and balanced ALTSA at 28 GHz.....	102
Figure 6.8: Top and 3D view of the proposed transition for antenna feeding.	104
Figure 6.9: Simulated S-parameters and phase difference of the proposed transition.....	105
Figure 6.10: Top (a) and bottom (b) view of the fabricated balanced ALTSA.....	106
Figure 6.11: Measured and simulated antenna return losses.....	107
Figure 6.12: Measured and simulated radiation patterns and cross-polarizations at 28 GHz.	107

LIST OF SYMBOLS AND ABBREVIATIONS

AL TSA	Antipodal Linearly Tapered Slot Antenna
CPW	Coplanar Waveguide
HMCW	Half-Mode Composite Waveguide
MCW	Mode Composite Waveguide
MIMO	Multiple-Input and Multiple-Output
mmW	millimeter-wave
PCB	Printed Circuit Board
RF	Radio Frequency
SIW	Substrate Integrated Waveguide
SICL	Substrate Integrated Coaxial Line
TRM	Transverse Resonance Method
TE	Transverse Electric
TEM	Transverse Electromagnetic
UHF	Ultra High Frequency
VPC	Variable Propagation Constant
5G	Fifth Generation

CHAPTER 1 INTRODUCTION

1.1 Background and Motivation

Modern development in wireless communication systems requires highly integrated and geometrically compact radio frequency (RF) and microwave circuits and modules featuring broadband and multiband functionalities. The most widely used frequency bands for commercial wireless communications such as mobile phone and wireless internet connectivity are allocated in the low microwave frequency ranges up to 6.0 GHz, covering popular or legacy bands of 900 MHz, 1.9 GHz, 2.45 GHz, 3.5 GHz and 5.8 GHz [1].

To enable agile and ubiquitous connectivity for a wide range of heterogeneous data transmission scenarios including environment- or user-defined smart radio platforms and for internet of things (IoT) with the integration of variable wireless functionalities, the emerging fifth generation (5G) wireless techniques should extend far beyond the capability of existing and current mobile communication systems. One of the 5G speculated technologies is to deploy both low and high frequency bands in a simultaneous manner. Within the 5G platform, some of the key enabling technologies include massive MIMO, carrier aggregation, low-latency technique, device-to-device link, and mmW cellular architecture. On one hand, the demand for high speed (> 10 Gbit/s) data transmission requires a larger bandwidth. To accommodate such a bandwidth increase, the carrier frequency over the mmW range is being considered for small cell and backhaul connectivity such as V-band (57-66 GHz) and E-band (71-76 GHz and 81-86 GHz) [2]. On the other hand, LTE and other long-ranged wireless platforms continue to evolve in a backwards-compatible way and will be an important part of the 5G wireless ecosystem for frequency bands below 6 GHz. Therefore, it is imperative to create low-cost and integrated hardware solutions, which should be able to support emerging wireless deployments over an unprecedented wide UHF-to-mmW frequency range. To this end, the development of a broadband or multi-band design platform is addressed in this thesis.

1.1.1 Rectangular Waveguide and Substrate Integrated Waveguide

The rectangular waveguide is widely used in the design and development of high frequency circuits and systems thanks to its simple structure, low loss, high quality factor, and high-power handling capability. Also as a fully-shielded structure, the interference between neighboring

waveguide circuits can be ignored completely. However, as a single-conductor structure, the rectangular waveguide presents a geometry-dependent cut-off frequency for its fundamental propagation TE_{10} mode, which limits its use at low frequencies. Furthermore, the integration of such a three-dimensional rectangular waveguide with planar circuits is an important challenge.

To mitigate the underlying problems of integration, a substrate integrated rectangular waveguide was proposed and demonstrated in [3]. The resulting planar topology provides a very promising solution for the development of microwave and mmW circuits and antennas, and today it has been widely known as Substrate Integrated Waveguide (SIW). The SIW consists of two rows of metallized vias embedded in a dielectric substrate that connects the top and bottom metal plates, thereby forming the side walls (shown in Figure 1.1). Due to its similarity with reference to rectangular waveguide, the SIW has a fundamental TE_{10} propagation mode. The SIW inherits the above-mentioned advantages of rectangular waveguide while fully realized in planar form and easily integrated with other planar circuits. A wide range of low-cost and high-performance SIW circuits and antennas have been developed [3], [4], [5] and [6].

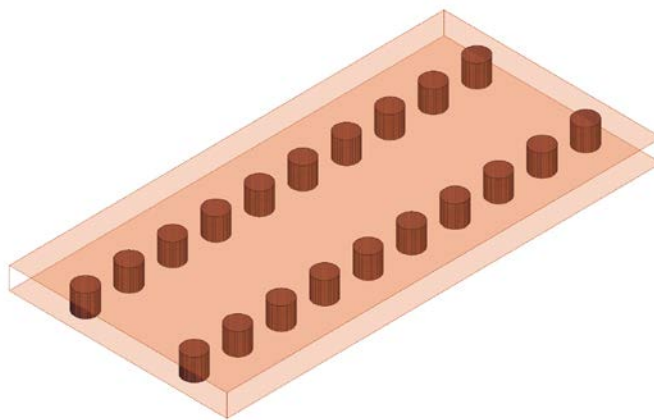


Figure 1.1: 3D illustration of SIW.

1.1.2 Coaxial Line and Substrate Integrated Coaxial Line

On the other hand, the coaxial line is a well-established popular type of non-dispersive TEM mode transmission line with zero cut-off frequency, which makes it suitable for low frequency operation. Unlike the rectangular waveguide having a geometrical dimension related to its cut-off frequency, the dimension of coaxial line can be designed to be small in support of low-to-high frequency operations. The coaxial line is also a fully-shielded structure, which is desirable for

minimizing interference in a high-density circuit. However, the coaxial line is difficult to integrate with planar circuits because of its fully enclosed inner conductor. Besides the integration, as frequency goes higher into mmW, the loss of coaxial line increases significantly, and a high fabrication precision of the inner and outer conductors is also required.

To overcome the integration issue of coaxial line with planar circuits, a substrate integrated form of coaxial line was proposed in [7], called Substrate Integrated Coaxial Line (SICL). The SICL consists of a printed rectangular coaxial structure, laterally shielded by metallized via arrays (shown in Figure 1.2). Like coaxial line, the SICL has a fundamental TEM propagation mode. The SICL also inherits most of the advantages of coaxial line. The SICL is fabricated in a planar form and can be easily integrated with other passive and active circuits and antennas. Numerous SICL-based components and techniques have been demonstrated with different processing techniques [7], [8], [9], [10], [11], [12] and [13].

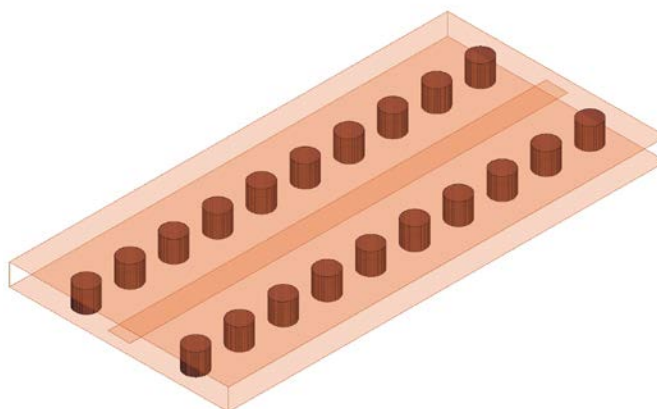


Figure 1.2: 3D illustration of SICL.

1.1.3 Mode Composite Waveguide

As discussed in the previous section, the advantages and disadvantages of coaxial line, rectangular waveguide and their substrate integrated counterparts are summarized in Table 1.1.

To make use of the advantages of both rectangular waveguide and rectangular coaxial line in support of simultaneous low and high frequency design and development, a new transmission line called Mode Composite Waveguide (MCW) is proposed in this thesis as shown in Figure 1.3.

Table 1.1: Comparison of different types of waveguides and transmission lines.

Characteristic/Type	Coaxial Line	SICL	Rectangular Waveguide	SIW
Conductor Loss	Medium	Medium	Low	Low
Dielectric Loss	Medium	Medium	None	Medium
Radiation Loss	None	Low	None	Low
Dispersion	None	None	Medium	Medium
Size	Small	Small	Large	Medium
Integration	Difficult	Easy	Difficult	Easy

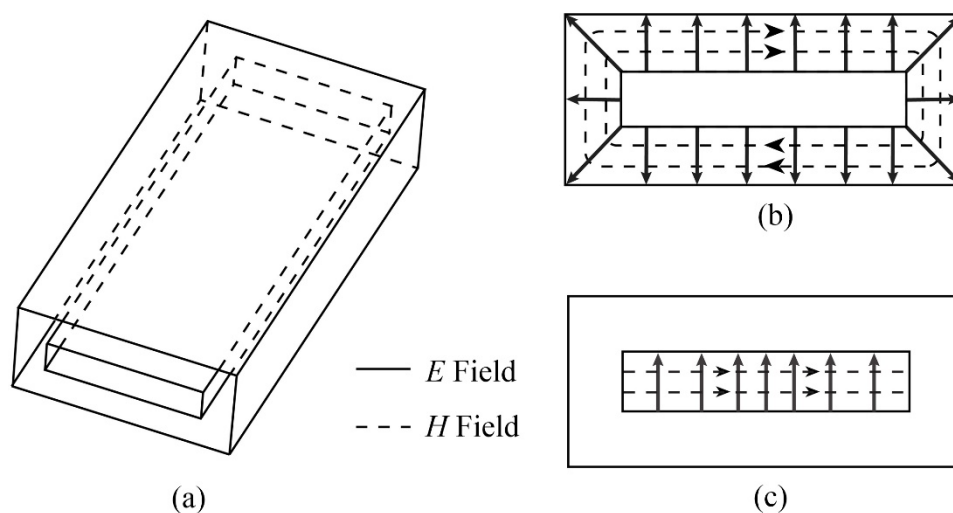


Figure 1.3: (a) 3D illustration of MCW, the E and H field distributions of its two fundamental modes: (b) TEM mode in outer waveguide, (c) TE₁₀ mode in inner waveguide.

The MCW consists of an inner rectangular metallic structure and an outer rectangular metallic enclosure. Under this arrangement, the outer structure acts as a rectangular coaxial line and supports the TEM mode, while the inner structure works as a rectangular waveguide and supports the TE₁₀ mode as shown in Figure 1.3. Due to the different nature of the TEM and TE₁₀ modes, the outer waveguide is suitable for lower frequency operation for its compact size, while the inner

waveguide is suitable for higher frequency operation thanks to its simple structure and low loss. Furthermore, the MCW can also be implemented in multilayer substrate integrated format, which organically combines the geometry of both SIW and SICL.

1.2 Outline of thesis

This thesis proposes a low-cost integrated hardware platform, namely MCW, for future 5G wireless systems and beyond. The MCW can support wireless front-end design and deployments over an extremely wide UHF-to-mmW frequency range. The thesis work covers multiple aspects of MCW related theoretical analysis and fabrication, MCW joint feeding network design, MCW circuits development, Half-Mode Composite Waveguide (HMCW) development, and other multilayer circuit and antenna development. The thesis is organized as follows:

Chapter 2 presents the theoretical analysis and fabrication process of the MCW. The MCW signal propagation properties of the TE_{10} mode in the inner waveguide and the TEM mode in the outer waveguide are discussed, demonstrating its capability to achieve optimal performance for both low and high frequency operations. Then, each of the waveguide parameters such as propagation constants, impedances, losses, and higher order modes of both the inner and outer waveguides are analyzed, respectively. Finally, the fabrication process of MCW is presented in detail, using the multilayer substrate integration techniques. Partial results of this chapter have been published in [14].

Chapter 3 develops two types of joint feeding networks for the integration and measurement of MCW. In both joint feeding networks, the inner and outer waveguides of MCW are transitioned into microstrip lines, respectively. The operation principles and design methodologies of the two joint feeding networks are discussed in detail. The joint feeding networks are fabricated and measured, and their application limitations in different scenarios are also discussed. Partial results of this chapter have been published in [14] [15].

Chapter 4 develops several MCW-based circuits through the exploitation of its different properties. A MCW directional coupler is proposed to achieve the interaction between the inner and outer waveguides. The mode conversion mechanism and the coupler operation principle are discussed in detail. A MCW based dual-mode filter is proposed, using the inner waveguide as the input and output feedings, and the outer waveguide as the dual-mode resonator. Two types of dual-

mode filters are designed to demonstrate the capability to control the filter bandwidth and improve the out of band selectivity. A MCW based planar magic tee is also proposed, which uses the inner waveguide as the summation port and the outer waveguide as the difference port for the circuit operation. Equally divided in phase and out of phase signals are achieved using the inner and outer waveguide mode diversity of MCW. Partial results of this chapter have been published in [16] [17].

Chapter 5 presents the theoretical analysis and fabrication of HMCW, which only occupies approximately half the size of MCW. In HMCW, the quasi- $TE_{0.5-0}$ mode signal propagates in the inner waveguide and the quasi-TEM mode signal propagates in the outer waveguide. The HMCW operation principle, impedance, loss, propagation characteristics and higher-order modes are analyzed. A joint feeding network is developed for the simultaneous excitation of the inner and outer waveguides of HMCW. Partial results of this chapter have been published in [18].

Chapter 6 presents double layer circuit and antenna using the multilayer substrate integration technique. Two different double layer variable propagation constant (VPC) directional couplers are proposed using variable waveguide propagation constants as an extra degree of design freedom. Both the forward and backward operations of coupler are achieved using different propagation constants, respectively. Then, a double layer balanced antipodal linear tapered slot antenna (ALTSA) is proposed with an improved cross-polarization performance. An integrated feeding network is also presented to excite the double layer antenna from a single layer CPW line. Partial results of this chapter have been published in [19] [20].

Chapter 7 concludes the thesis work and suggests some future directions of research in the development of MCW and HMCW based circuits and antennas.

CHAPTER 2 THEORETICAL ANALYSIS AND FABRICATION PROCESS

The MCW consists of an inner rectangular waveguide and an outer rectangular coaxial line, which creates a perfect composite duo waveguide structure. In the inner waveguide, the fundamental mode is TE_{10} mode like a dielectric-loaded rectangular waveguide or SIW, while in the outer waveguide, the fundamental mode is TEM mode in a similar way as in the rectangular coaxial line or SICL (shown in Figure 2.1). Due to the difference of modes nature, the outer waveguide TEM mode is suitable for lower frequency operation, while the inner waveguide TE_{10} mode is suitable for higher frequency operation. With the proposed MCW, both low and high frequency signals can be transmitted simultaneously in their desirable waveguide modes within two different cross sections.

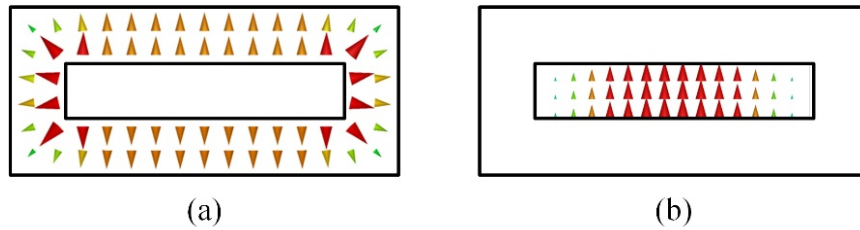


Figure 2.1: Outer and inner waveguides of MCW and their fundamental modes: (a) TEM mode in outer waveguide, (b) TE_{10} mode in inner waveguide.

2.1 Theoretical Analysis of Mode Composite Waveguide

The MCW consists of duo waveguide structures where the inner waveguide and the outer waveguide are electrically shielded from each other. This scenario of isolation allows the development of two independent analyses of the inner and outer waveguides of MCW. Therefore, the following waveguide parameters are analysed for the two waveguides, respectively: impedance, propagation constant, conductor and dielectric losses.

2.1.1 Outer Waveguide Parameters

The outer waveguide is a TEM mode rectangular coaxial line. Therefore, the characteristic formulas for rectangular coaxial line can be directly applied to the modeling of the outer

waveguide. Its fundamental TEM mode propagation constant is independent of the geometry of the line cross section, and the propagation constant can be directly calculated using (2.1)

$$\beta_{TEM} = 2\pi f \sqrt{\mu\varepsilon} \quad (2.1)$$

where f is the operation frequency of signal, μ and ε are the permeability and permittivity of the outer waveguide dielectric material filling, respectively. For the TEM mode characteristic impedance of the outer waveguide, it can be calculated by (2.2)

$$Z_{TEM} = \frac{1}{v_p C} = \frac{\sqrt{\mu\varepsilon}}{C} \quad (2.2)$$

where v_p is the phase velocity of the propagating signal and C is the transmission line capacitance per unit length. Once the unit length capacitance of the outer waveguide is known, the impedance can then be calculated.

Since the MCW waveguide structure is made of a multilayer PCB process, the thickness of the waveguide is relatively small compared to its width. So the outer waveguide capacitance can be calculated through a conformal mapping method for a thin inner conductor rectangular coaxial line with the inner conductor centrally located [21]. The line unit length capacitance is formulated by (2.3)

$$C_{total} = 2C_1 + 4C_2 \quad (2.3)$$

where

$$C_1 = \varepsilon \frac{2W_i}{H_o - H_i}$$

$$C_2 = \varepsilon \cdot \frac{H_o}{H_o - H_i} \cdot \ln \frac{2H_o - H_i}{H_i} \cdot \frac{\ln \left(1 + \coth \frac{\pi(W_o - W_i)}{2H_o} \right)}{\pi \ln 2}$$

$$+ \varepsilon \cdot \ln \frac{H_i(2H_o - H_i)}{(H_o - H_i)^2} \cdot \frac{\ln \left(1 + \coth \frac{\pi(W_o - W_i)}{2H_o} \right)}{\pi \ln 2}$$

The geometrical parameters are shown in Figure 2.2, where two equivalent capacitors of the regions inside the outer waveguide enclosed by dashed lines are also shown. When the unit length capacitance of the outer waveguide is known, the impedance can be directly calculated.

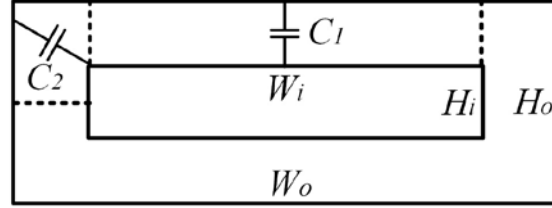


Figure 2.2: Unit length capacitance distribution in a thin rectangular coaxial line.

The total loss of outer waveguide consists of conductor and dielectric losses. The outer waveguide conductor loss is dependent on conductor property, line cross section geometry, and operating frequency. Using the Wheeler's method, the formula for the conductor loss of rectangular coaxial line is derived in [22], where it can also be applied to the outer waveguide conductor loss calculation as in (2.4)

$$\alpha_c = \frac{R_s \sqrt{\epsilon_r}}{\eta_0 Z_{TEM}} \left(\frac{\partial Z}{\partial W_o} + \frac{\partial Z}{\partial H_o} - \frac{\partial Z}{\partial W_i} - \frac{\partial Z}{\partial H_i} \right) \quad (2.4)$$

where $R_s = \sqrt{\frac{\pi f \mu}{\sigma}}$ is the surface resistivity (σ is the conductivity of metal), Z_{TEM} is the outer waveguide impedance as derived in the previous impedance analysis. ϵ_r is the relative dielectric permittivity and η_0 is the intrinsic impedance of free space, and the outer waveguide dimensional parameters W_i , W_o , H_i and H_o are the same as shown in Figure 2.2.

The dielectric loss of the outer waveguide is independent of the waveguide geometry, which is calculated by

$$\alpha_d = \frac{\beta_{TEM} \tan \delta}{2} \quad (2.5)$$

where $\tan \delta$ is the loss tangent of substrate. A comparison of the two formulas of outer waveguide conductor and dielectric losses suggests that the dielectric loss increases faster than the conductor loss as frequency increases.

2.1.2 Inner Waveguide Parameters

The inner waveguide is similar to a rectangular waveguide, where its fundamental mode is the TE₁₀ mode. Thanks to their similarity, characteristic formulas for rectangular waveguide can also be directly applied to the inner waveguide. The cutoff frequency of the fundamental TE₁₀ mode is calculated by

$$f_{c(TE_{10})} = \frac{1}{2w\sqrt{\mu\varepsilon}} \quad (2.6)$$

where w is the width of waveguide, μ and ε are the permeability and permittivity of the inner waveguide dielectric material filling respectively. The inner waveguide propagation constant of the fundamental TE₁₀ mode can be calculated by (2.7)

$$\beta_{TE_{10}} = 2\pi f \sqrt{\mu\varepsilon} \sqrt{1 - (f_c/f)^2} \quad (2.7)$$

where f is the operating frequency. The TE₁₀ mode impedance formula can be calculated by (2.8) from the E and H field equations derived in [23].

$$Z_{TE_{10}} = \frac{k\eta}{\beta} = \alpha \frac{h}{w} \sqrt{\frac{\mu}{\varepsilon}} \frac{1}{\sqrt{1 - (f_c/f)^2}} \quad (2.8)$$

where h and w are respectively the height and width of the rectangular waveguide, α is a coefficient determined by the choice of impedance definition and integration path. In this work, a power-current definition is selected where $\alpha = \frac{\pi^2}{8}$ [23].

Again, the inner waveguide loss consists of conductor and dielectric contributions. Analytical formulas in [24] for both the dielectric and conductor losses are derived and adopted for the present waveguide structure as in (2.9) and (2.10).

$$\alpha_d = \frac{k^2 \tan \delta}{2\beta} = \frac{\pi f \sqrt{\varepsilon_r} \tan \delta}{c \sqrt{1 - (f_c/f)^2}} \quad (2.9)$$

$$\alpha_c = \frac{\sqrt{\pi f \varepsilon_0 \varepsilon_r}}{h \sqrt{\sigma}} \frac{1 + 2(f_c/f)^2 h/w}{\sqrt{1 - (f_c/f)^2}} \quad (2.10)$$

2.2 Parametric Study of Mode Composite Waveguide

Based on the previous analysis, the selection of MCW dimensions (width and height), material of substrate, and operating frequency will have significant effects on both the inner and outer waveguide impedances as well as their loss performances. Parametric study of these parameters and their effects on MCW is conducted, where the MCW dimensions under study in this section are shown in Figure 2.3.

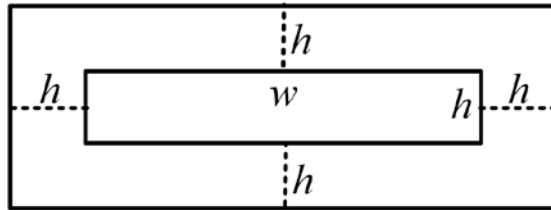


Figure 2.3: Dimensions of the inner and outer waveguides of MCW.

2.2.1 Impedance Parametric Study

Because the impedance of the outer waveguide is mostly determined by the capacitance between the top and bottom conductors to the inner conductor (given that width is much larger than height in our case), and the gap distance on the two sides has little effect on the total outer waveguide impedance. To simplify the analysis, the top and bottom distance of the outer waveguide, as well as the left and right-side gap distance between the inner and outer conductors is kept the same as the inner waveguide thickness (shown in Figure 2.3). This relationship between the inner and outer waveguides will be used in all the following analysis in this section. In this case, the MCW has the total width of $w+2h$ and the total height of $3h$.

When the height of the inner waveguide is fixed at $h=0.508$ mm (thickness of a 20 mil substrate) and frequency at 50 GHz (to ensure that the signal is above the cutoff frequency), both waveguide impedances for different w are shown in Figure 2.4 with three different dielectric material fillings ($\epsilon_r=1$, $\epsilon_r=3$, $\epsilon_r=5$) and inner waveguide width w normalized by its height h . From Figure 2.4, one can observe that the impedance of both waveguides decreases as w increases, with the inner waveguide impedance decreasing relatively faster than that of the outer waveguide. A higher permittivity material yields a lower impedance for the waveguide duo, and at the same time, it

pushes downward the cutoff frequency of the inner waveguide. The impedance of the inner waveguide increases rapidly as its operation frequency approaches its width related cutoff frequency.

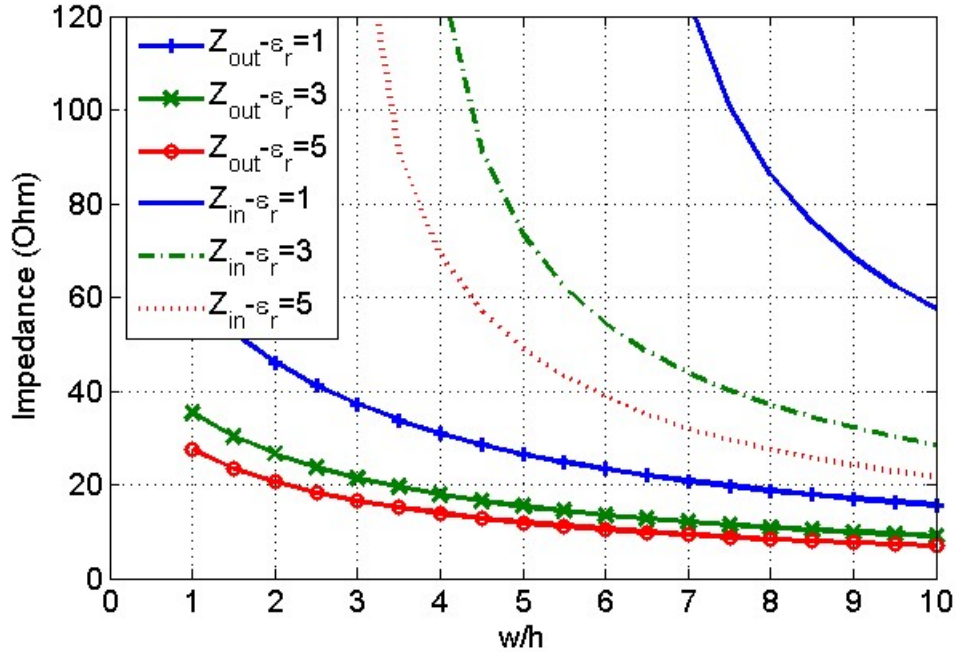


Figure 2.4: Simulated impedance of the inner and outer waveguides at different width and permittivity (Z_{in} inner waveguide impedance and Z_{out} outer waveguide impedance).

On the other hand, the waveguide height also influences the inner and outer waveguide impedances. When the width of the inner waveguide is fixed at $w=5.08$ mm and frequency at 50 GHz, both waveguide impedances for different h are shown in Figure 2.5 with three different dielectric material fillings ($\epsilon_r=1$, $\epsilon_r=3$, $\epsilon_r=5$). Both waveguide impedances increase as the height increases, with the inner waveguide impedance increasing relatively faster than that of the outer waveguide. A similar influence of material permittivity on the impedances is also observed.

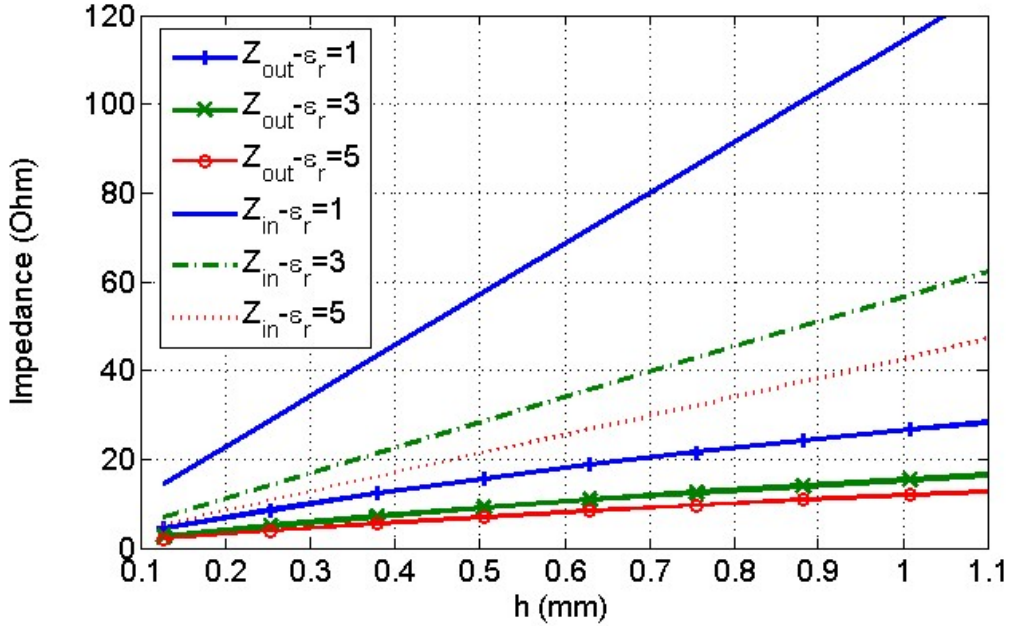


Figure 2.5: Simulated impedance of the inner and outer waveguides at different height and permittivity (inner waveguide impedance Z_{in} and outer waveguide impedance Z_{out}).

The inner waveguide impedance is generally larger than that of the outer waveguide, given that the inner waveguide is fully enclosed in the outer structure and physically smaller than the outer waveguide. To increase w , both waveguide impedances will decrease simultaneously; while to increase h , both waveguide impedances will increase simultaneously. The impedance changes of both waveguides have the same trend (but at different rates) as the width and height change. So, it is not feasible to change one waveguide impedance in one direction while keeping the other constant or changing in the opposite direction, by only changing geometrical dimensions (under the condition that substrates of the same thickness are used for a multilayer structure construction).

2.2.2 Loss Parametric Study

In addition to the effect on the impedance of the waveguide duo, the dimension of the MCW would also affect both inner and outer waveguide losses. To study the dimension effect on the losses, the 0.508 mm thick RT/Duroid 6002 substrate ($\epsilon_r=2.94$) with copper metallization is used here for demonstration. The loss of inner and outer waveguides of MCW consists of both dielectric and conductor contributions. The losses of both waveguides for different w are calculated at 50

GHz using equations (2.4), (2.5), (2.9) and (2.10) respectively, and their comparison results are shown in Figure 2.6.

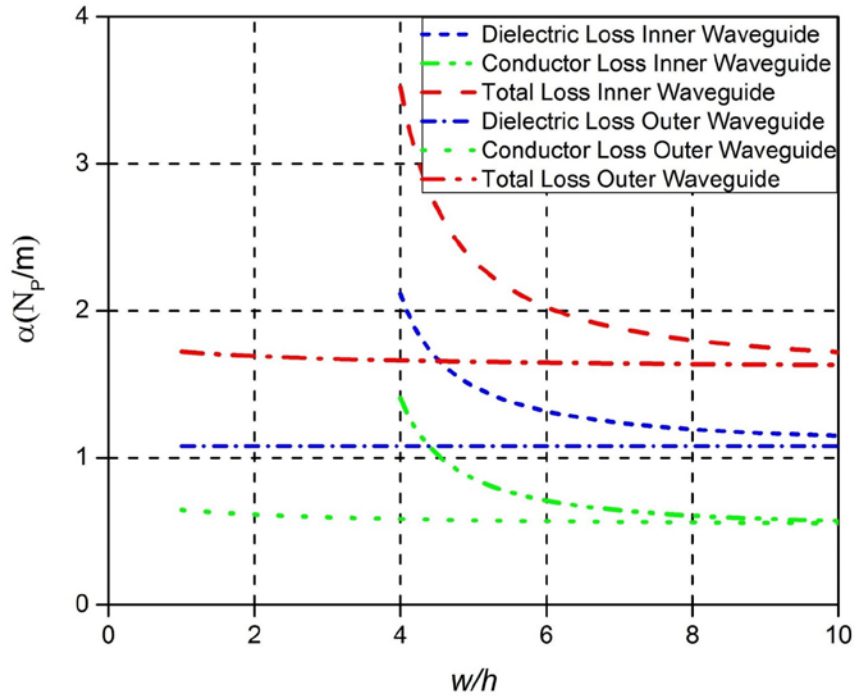


Figure 2.6: Calculated dielectric and conductor losses of inner and outer waveguides of MCW at different widths (RT/duroid 6002, $\epsilon_r=2.94$, $h=0.508$ mm at 50 GHz).

For the conductor loss, when w increases the current density decreases, thus the conductor losses of both inner and outer waveguides decreases as well. For the dielectric loss, the outer waveguide dielectric loss is geometry-independent, and only changes with frequency due to its TEM fundamental mode nature. The inner waveguide dielectric loss decreases as w increases due to the decrease of the cutoff frequency.

Besides the MCW geometry, the loss behavior of the inner and outer waveguides also changes at different frequency. Using the same substrate with width $w=2.54$ mm, the calculated dielectric and conductor losses of both waveguides against frequency are shown in Figure 2.7. For the outer waveguide, both the dielectric and conductor losses increase as frequency increases. The dielectric loss increases linearly with frequency, while the conductor loss increases at a lower rate. In a high

frequency region, the dielectric loss dominates the outer waveguide total loss. For the inner waveguide, both the dielectric and conductor losses are high around the cutoff frequency due to a large attenuation of the cutoff effect. Both the dielectric and conductor losses first decrease as they leave the vicinity of cutoff frequency region and then increase as frequency goes higher. In a high frequency region, the dielectric loss also dominates the inner waveguide total loss.

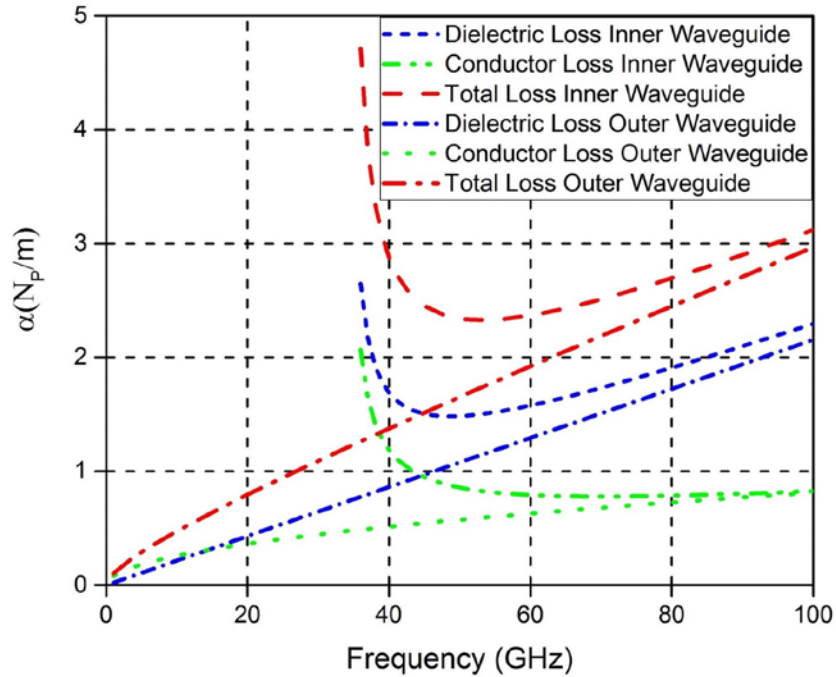


Figure 2.7: Calculated dielectric and conductor losses of both inner and outer waveguides at different frequencies (RT/duroid 6002, $\epsilon_r=2.94$, $h=0.508$ mm, $w=2.54$ mm).

At low frequencies, the total loss (conductor + dielectric) of the outer waveguide is low, while the total loss of the inner waveguide is high due to the cutoff effect as shown in Figure 2.7. However, at high frequencies, the total loss of the outer waveguide increases faster than that of the inner waveguide, giving the inner waveguide an advantage of better loss performance. In this example, the total loss of the outer waveguide is still lower than that of the inner waveguide even over the high frequency region of interest. This is because the inner waveguide is fully enclosed in the outer waveguide, and the total size of the inner waveguide is significantly smaller. If both waveguides are scaled to the same size, the inner waveguide does exhibit a lower loss at high frequencies.

2.3 Higher Order Mode Analysis

Besides the fundamental modes, higher order modes of both the inner and outer waveguides of MCW may also exist at higher frequencies. The knowledge of the cutoff frequencies of these higher order modes is important for the band selections in design of both the inner and outer waveguides MCW. The RT/duroid 6002 substrate with $h=0.508$ mm and $w=2.54$ mm is re-used here as an example for demonstration purpose.

The outer waveguide is simulated with HFSS and the E field distributions of the fundamental and first four higher order modes at cross-section are shown in Figure 2.8.

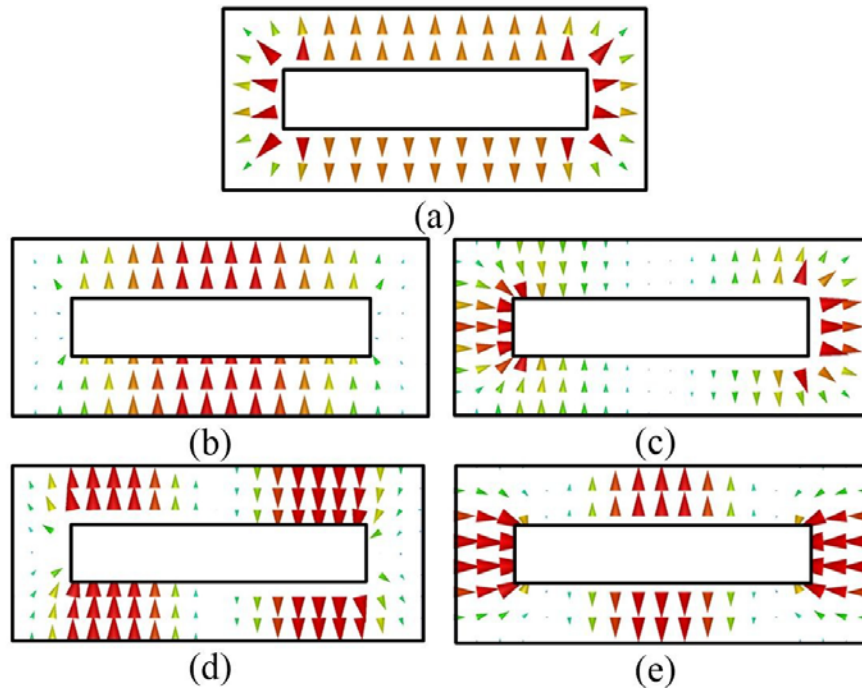


Figure 2.8: Fundamental and higher order modes E field distributions of outer waveguide (a) fundamental mode, (b) folded TE_{20} I, (c) folded TE_{20} II, (d) folded TE_{40} I, (e) folded TE_{40} II.

Furthermore, corresponding dispersion curves of each mode are shown in Figure 2.9, where the either 1st and 2nd or 3rd and 4th higher order modes have similar cutoff frequencies to each other, respectively. Based on the field distributions, the first four higher order modes of the outer waveguide are called folded TE_{20} I mode, folded TE_{20} II mode, folded TE_{40} I mode and folded TE_{40}

II mode, respectively in this thesis. This terminology is used because each of the field distributions exhibits a folded version of conventional TE_{20} or TE_{40} mode in a rectangular waveguide. The folded TE modes of odd indexes such as TE_{10} and TE_{30} do not exist as they cannot satisfy the geometrical symmetry of the outer waveguide cross section.

2.3.1 Higher Order Mode Cutoff Frequency

As the first four outer waveguide higher order modes are all TE modes, their cutoff frequencies can be calculated using the transverse resonance method (TRM). To take advantage of the symmetrical field distribution, only the first quadrant of the outer waveguide cross section is considered in the TRM calculation, and the corresponding equivalent circuit is shown in Figure 2.10, where T and T' are two reference plane used in calculation. The two boundary conditions are either open or short dependent on the corresponding higher order mode. The equations in [25] are used to calculate the reactive corner effect, which is denoted as $-jB$ in our case.

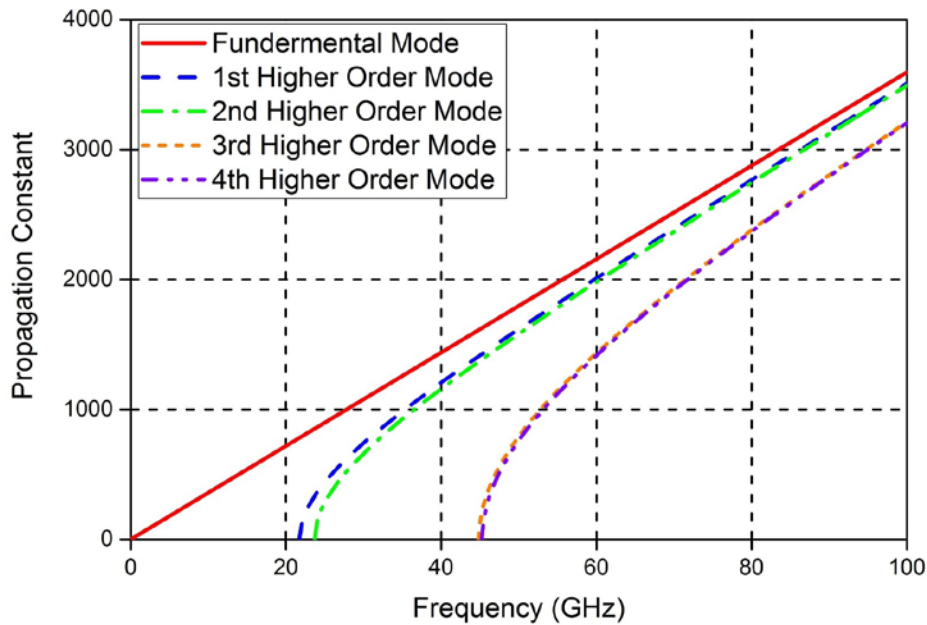


Figure 2.9: Simulated dispersion diagram of outer waveguide, including the fundamental TEM mode and first four higher order modes (RT/duroid 6002, $\epsilon_r=2.94$, $w=2.54$ mm, $h=0.508$ mm).

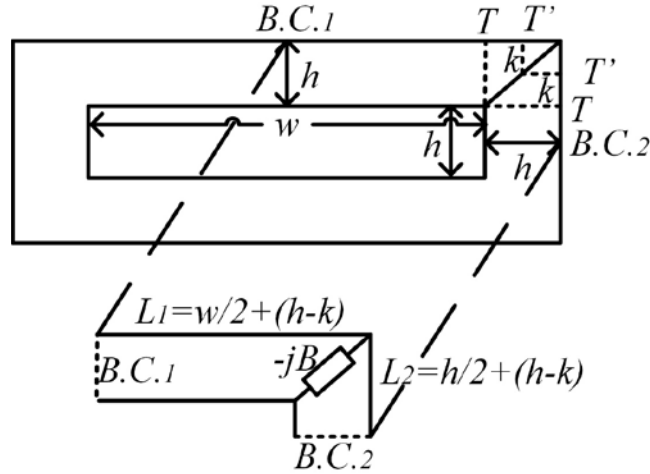


Figure 2.10: Outer waveguide cross section and its equivalent circuit for TRM.

$$\frac{B}{Y_0} = \frac{\left(\frac{B_a}{Y_0}\right)^2 + 1}{\frac{B_b}{Y_0}} - 2\frac{B_a}{Y_0} \quad (2.11)$$

$$\frac{2\pi(h-k)}{\lambda_g} = \cot^{-1}\left(2\frac{B_b}{Y_0} - \frac{B_a}{Y_0}\right) \quad (2.12)$$

$$\frac{B_a}{Y_0} = \frac{2h}{\lambda_g} \left(0.878 + 0.498\left(\frac{2h}{\lambda_g}\right)^2\right) \quad (2.13)$$

$$\frac{B_b}{Y_0} = \frac{\lambda_g}{2\pi h} \left(1 - 0.114\left(\frac{2h}{\lambda_g}\right)^2\right) \quad (2.14)$$

where λ_g is the guided wavelength in the transverse direction. Based on the boundary conditions for each higher order mode listed in Table 2.1, the corresponding TRM equations are shown below (in the order of folded TE₂₀ I, folded TE₂₀ II, folded TE₄₀ I and folded TE₄₀ II mode).

Table 2.1: Comparison of outer waveguide higher order mode cutoff frequencies.

Cutoff Frequency	Folded TE ₂₀ I	Folded TE ₂₀ II	Folded TE ₄₀ I	Folded TE ₄₀ II
B.C.1	Open	Short	Short	Open
B.C.2	Short	Open	Short	Open
TRM Calculation	21.8 GHz	23.8 GHz	45.0 GHz	45.5 GHz
HFSS Simulation	21.8GHz	23.8 GHz	44.9 GHz	45.3 GHz

$$\tan\left(\frac{2\pi}{\lambda_g}(w/2 + (h-k))\right) - \frac{B}{Y_0} - \cot\left(\frac{2\pi}{\lambda_g}(h/2 + (h-k))\right) = 0 \quad (2.15)$$

$$-\cot\left(\frac{2\pi}{\lambda_g}(w/2 + (h-k))\right) - \frac{B}{Y_0} + \tan\left(\frac{2\pi}{\lambda_g}(h/2 + (h-k))\right) = 0 \quad (2.16)$$

$$-\cot\left(\frac{2\pi}{\lambda_g}(w/2 + (h-k))\right) - \frac{B}{Y_0} - \cot\left(\frac{2\pi}{\lambda_g}(h/2 + (h-k))\right) = 0 \quad (2.17)$$

$$\tan\left(\frac{2\pi}{\lambda_g}(w/2 + (h-k))\right) - \frac{B}{Y_0} + \tan\left(\frac{2\pi}{\lambda_g}(h/2 + (h-k))\right) = 0 \quad (2.18)$$

The choice of the boundary conditions can be confirmed by observing each higher order mode field distribution shown in Figure 2.8, where maximum E field implies open and minimum E field implies short. By solving the above nonlinear equations under each boundary condition, each higher order mode cutoff frequency can be calculated. To demonstrate the proposed TRM method, the calculated cutoff frequencies of the higher order modes are compared to the simulated dispersion curves as shown in Table 2.1. The calculated and simulated results with HFSS agree

very well with each other within the variation less than 0.5%. This method provides an accurate prediction for the upper limit of the monomode frequency region of the outer waveguide.

The cutoff frequencies of inner waveguide higher order modes are relatively easy to calculate due to its similarity to the rectangular waveguide or SIW. In our case, the waveguide width is much large than the height, and the first several higher order modes are all TE_{n0} modes ($n=2, 3, 4\dots$). Therefore, the inner waveguide cutoff frequencies can be calculated by:

$$f_{c_{n0}} = \frac{n}{2w\sqrt{\mu\epsilon}} \quad (2.19)$$

where n is the mode index and w is the waveguide width.

2.3.2 Monomode Frequency Region

It is always desirable to have a monomode frequency operation for both the inner and outer waveguides, where all the higher order modes are not propagating. Based on the higher order modes analysis above, the monomode frequency region of the outer waveguide ranges from DC to its first higher order mode cutoff frequency $f_{c_folded_TE20}$, while that of the inner waveguide ranges from its fundamental mode cutoff frequency f_{c_TE10} to the first higher order mode cutoff frequency f_{c_TE20} . The frequency region from $f_{c_folded_TE20}$ to f_{c_TE10} is denoted as the monomode forbidden region where no monomode propagation can be achieved in either waveguide.

To show each of the mentioned regions, MCW with the same specifications in the previous analysis is re-used here with 0.508 mm thick RT/duroid 6002 substrate. When $w=2.54$ mm, the outer waveguide monomode frequency region is from DC to $f_{c_folded_TE20}=21.8$ GHz, and the inner waveguide monomode frequency region is from $f_{c_TE10}=34.4$ GHz to $f_{c_TE20}=68.8$ GHz. In this case, the monomode forbidden region is from 21.8 GHz to 34.4 GHz, where the higher order mode starts to show up in the outer waveguide while frequency is still below the cutoff frequency of the inner waveguide. This monomode forbidden region will change as w changes as shown in Figure 2.11. When the w/h ratio increases, the monomode forbidden region reduces correspondingly.

For the MCW constructed with the same substrates in both waveguides, it always holds that $f_{c_folded_TE20}$ is smaller than f_{c_TE10} , regardless of the choice of their dimensions. The existence of the monomode forbidden region is inevitable if the substrate permittivity is constant across the whole structure. However, there are some possible ways to narrow down or even eliminate the forbidden

region at the cost of using different permittivity substrates and increasing fabrication complexity. These methods can be either to bring down f_{c_TE10} by increasing the permittivity of the inner waveguide or to push up $f_{c_folded_TE20}$ by decreasing the permittivity of the outer waveguide. The physical implementation of these methods is not discussed here.

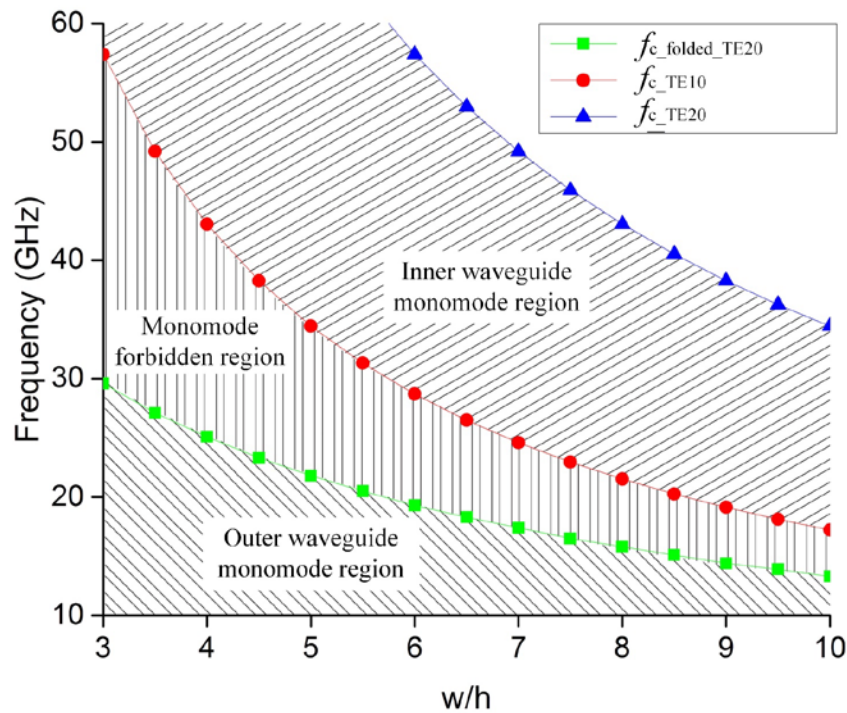


Figure 2.11: Calculated monomode regions for the inner and outer waveguides at different width.

2.4 Fabrication of Mode Composite Waveguide

The MCW in this thesis is fabricated using three layers of PCB substrates with multilayer substrate integrating technique, which is made available in our Poly-Grames Research Center. The fabrication process uses middle layer to construct the inner waveguide and all three layers to construct the outer waveguide of MCW as shown in Figure 2.12, following the four steps below:

- Step I: Choose the middle substrate with its thickness equal to the height of the inner waveguide. Metalize the top and bottom surfaces of the substrate to form the top and bottom metallic covers of the inner waveguide.
- Step II: Insert via arrays at the middle substrate along the propagation direction to form the side walls of the inner waveguide and the inner conductor of the outer waveguide.

- Step III: Glue the top and bottom substrates to the middle substrate to form the triple layer MCW structure. Metallize the top and bottom surfaces of the structure to form the top and bottom metallic covers of the outer waveguide.
- Step IV: Insert via arrays at the triple layer MCW structure along propagation direction to form the side walls of the outer waveguide.

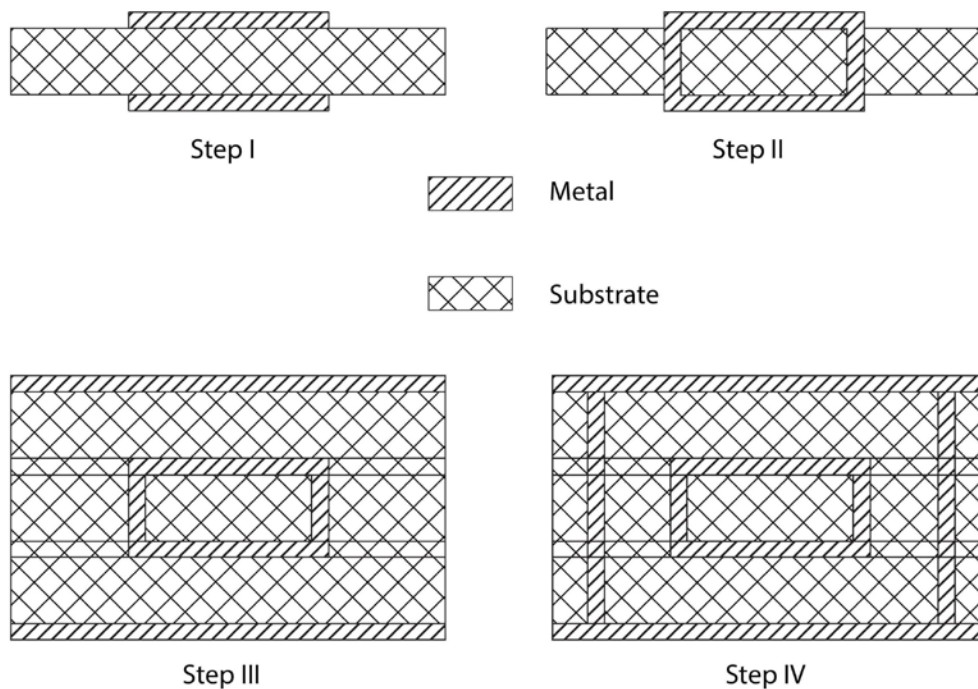


Figure 2.12: Fabrication process of the substrate integrated MCW

The above-described four steps define structural and electrical constraints and limits, which should be considered to achieve a desired performance, starting from the substrate and size selections (permittivity and thickness) to the choice of the metalized via parameters (shape, dimension and position). Of course, the fabrication of a MCW depends on the processing techniques. In some cases, the bilateral walls of the inner waveguide can be synthesized with continuous metallic walls. In the above theoretical analysis, the substrate via effects are assumed to be negligible provided that the design of such via arrays meets the requirement of substrate integrated side walls without leakage. It worth to mention that, this concept of MCW is not only

limited to substrate integrated technique, and other technologies such as LTCC, RF CMOS and 3D printing can also be used for fabrication.

2.5 Dimension of Mode Composite Waveguide

According to the previous parametric study, the choice of substrate and dimensions for MCW is a tradeoff in impedance, loss, operation frequency, and fabrication complexity. To achieve the optimal performances of both inner and outer waveguides, the width, height and permittivity of MCW shall be carefully chosen. Due to the substrate integration nature, the height and permittivity of MCW are determined by the substrate property in use, which is limited by its market availability. Also, the total thickness of the multilayer circuit is limited by our laboratory fabrication process to be less than 2.54 mm (100 mil) for prototyping. Compared to the height and permittivity restrictions, the choice of the MCW width is much more flexible, which only depends on the inner and outer waveguide vias positions in design. After tradeoff analysis with performance, robustness, fabrication and cost, we use three layers of 0.508 mm thick RT/duroid 6002 substrates ($\epsilon_r=2.94$) to construct the MCW, where the inner waveguide is built on the middle layer and the outer waveguide is built on all three layers.

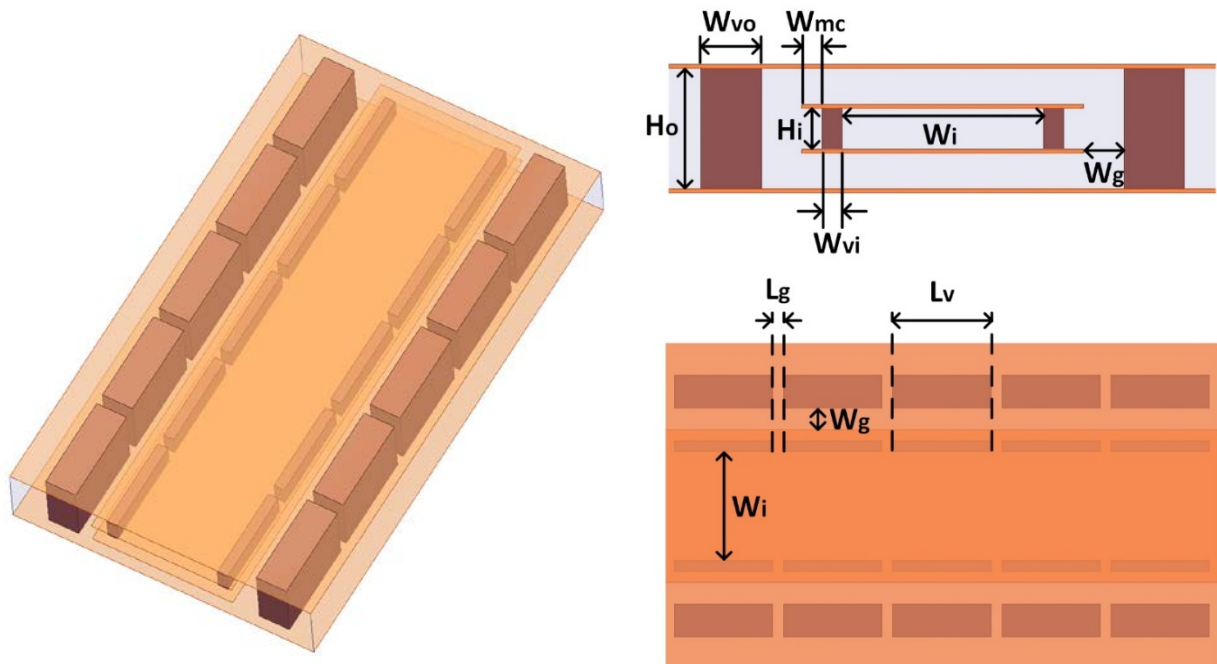


Figure 2.13: 3D view and dimensions of substrate integrated MCW.

The dimensions of substrate integrated MCW are shown in Figure 2.13, where the heights of the inner and outer waveguides are $H_i=0.508$ mm and $H_o=1.524$ mm respectively, based on the substrate selection. The width of inner and outer metalized vias are $W_{vi}=0.254$ mm and $W_{vo}=0.762$ mm respectively, where the outer via is three times wider than the inner counterpart due to the fabrication restriction that via width shall be at least half the substrate total thickness for metallization purposes. The metal width of the inner waveguide is also slightly extended by $W_{mc}=0.254$ mm to meet the via metallization requirement in our laboratory. The side gap distance $W_g=0.508$ mm is selected such that both the vertical and horizontal gap distances between the inner and outer conductors are kept the same. Instead of using circular vias, the rectangular vias are used in the thesis to achieve better accuracy in waveguide width control. Both the inner and outer waveguide vias are periodic with length $L_v=2.286$ mm and gap $L_g=0.254$ mm. The via gap is the minimum allowable size in fabrication, to minimize the gap leakage loss.

The dimensions of MCW selected above will be used in all the circuits in this thesis, unless otherwise mentioned, and the inner waveguide width W_i will be the only parameter that differs in different applications. According to the previous inner waveguide analysis, the inner waveguide width W_i is directly related to its fundamental mode cutoff frequency. Though the parameter W_i can be arbitrarily chosen according to the circuit designer, the choice is crucial to determine the operating frequency of inner waveguide. Therefore, based on the inner waveguide operation band in each MCW circuit implementation, the optimal W_i can be selected accordingly. This selection of substrate and related dimensions will be applied to all the following MCW circuits in this thesis.

2.6 Conclusion

In this chapter, the inner and outer waveguides of MCW are analyzed respectively using the mode isolation property of MCW. The key waveguide parameters such as propagation constants, impedances, losses, and higher order mode cutoff frequencies of both the inner and outer waveguides of MCW are analyzed. Equations are summarized for each waveguide parameter of MCW respectively. Parametric study is conducted using simulation and calculation results, where the effects of different MCW parameters are presented. The MCW dimension selection is discussed based on the parametric study, and the corresponding fabrication process is also provided.

CHAPTER 3 JOINT FEEDING NETWORK OF MODE COMPOSITE WAVEGUIDE

To measure the MCW or connect the MCW to other planar circuits, guiding signal in the proposed MCW need to be transitioned to planar transmission lines such as microstrip line or CPW. The standalone transitions of inner and outer waveguides to microstrip line are first presented, respectively. Then two types of joint feeding networks of MCW are presented, which can excite both the inner and outer waveguides from different microstrip line feedings simultaneously.

3.1 Outer Waveguide Feeding Network

The outer waveguide is fabricated on a triple layer structure, where the inner conductor is sandwiched between the top and bottom layers. To match the triple layer outer waveguide to the single layer microstrip line, a multilayer transition with various tapering structures is designed (shown in Figure 3.1).

In this demonstration, the inner waveguide width $W_i=2.54$ mm is selected for the MCW. This transition can match both the impedance and field distribution at the same time, where their gradual changes at each denoted cross section are also shown in Figure 3.1. The field distribution of microstrip line (P_1) which is mostly confined in the first layer is gradually converted to the field distribution of the outer waveguide (P_4), where the fields are symmetrically distributed in all the three layers. The transition cross sections of P_2 and P_3 in between P_1 and P_4 are also shown here, exhibiting a smooth evolution of both the impedance and field distribution. The design parameters of the outer waveguide to microstrip line transition are $W_{ms}=1.321$ mm, $W_{t1}=3.556$ mm, $W_{t2}=0.762$ mm, $L_t=8.763$ mm, and the total MCW length is $L_{tot}=13.21$ mm as shown in Figure 3.1. The total length of tapering structure is dependent on the operation frequency, where a longer taper is needed when the circuit is operating at a lower frequency band.

The fabricated microstrip line to outer waveguide transition in back-to-back is shown in Figure 3.2. TRL calibration is used to de-embed the connector effect in the two-port measurement. The simulated and measured results are in a good agreement as shown in Figure 3.3. Good matching of the transition for low frequency operation is achieved from 7 GHz to 13 GHz ($S_{11}<-10$ dB), and total insertion loss (including two back-to-back transitions and a certain length of outer waveguide) is better than -0.6 dB in the operation band.

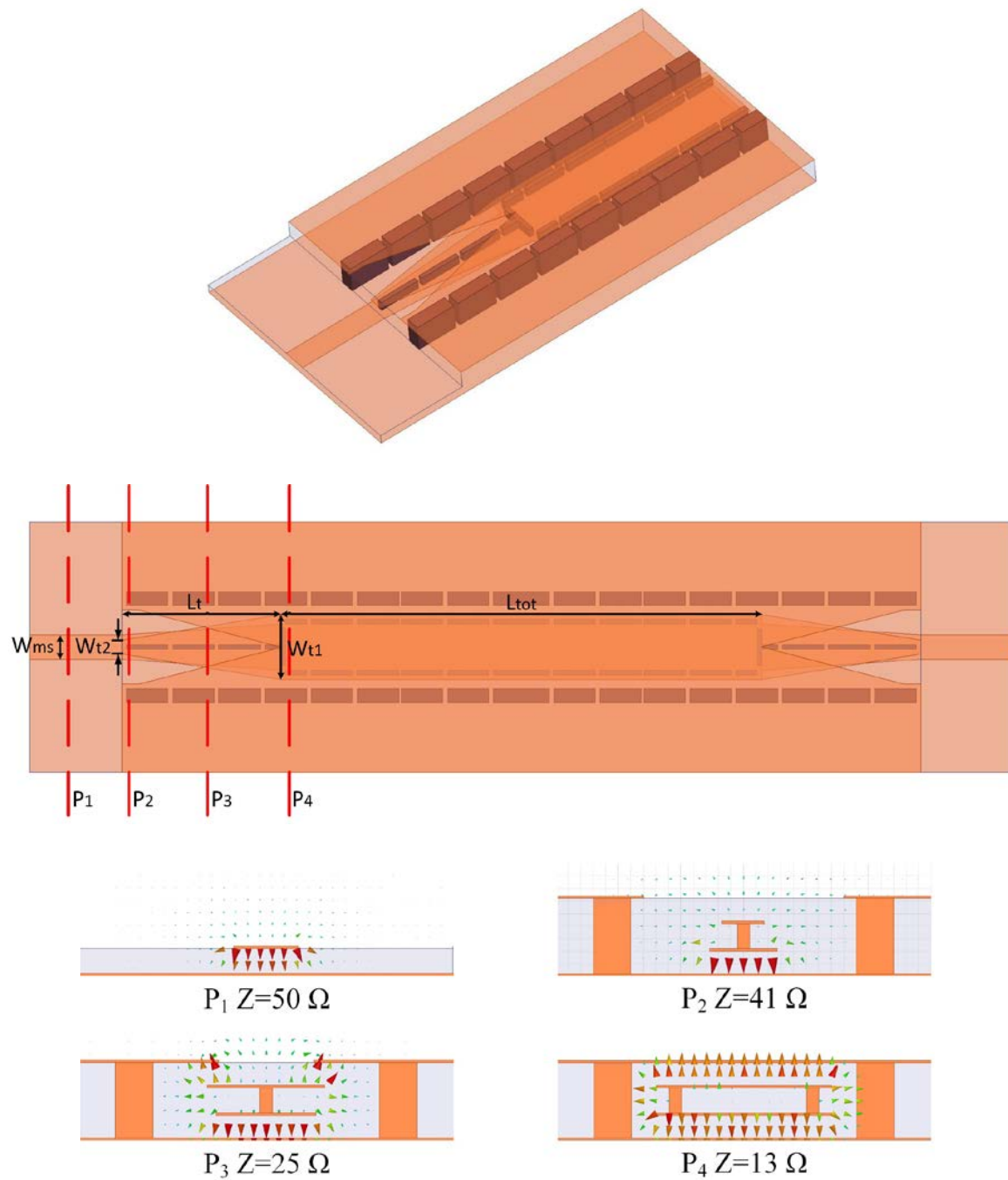
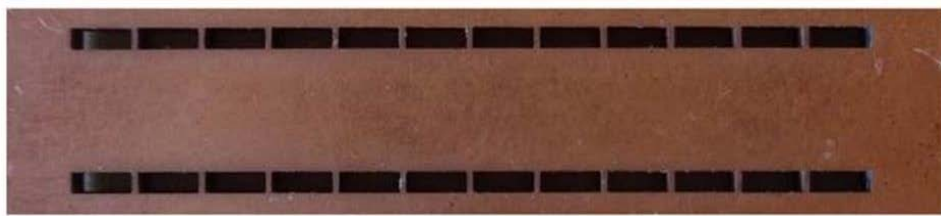


Figure 3.1: 3D view, dimensions of microstrip line to outer waveguide transition in back-to-back setup, and the E field distributions and impedances at each denoted position.



(a)



(b)

Figure 3.2: Pictures of the front side (a) and back side (b) of the fabricated MCW with microstrip to outer waveguide transition.

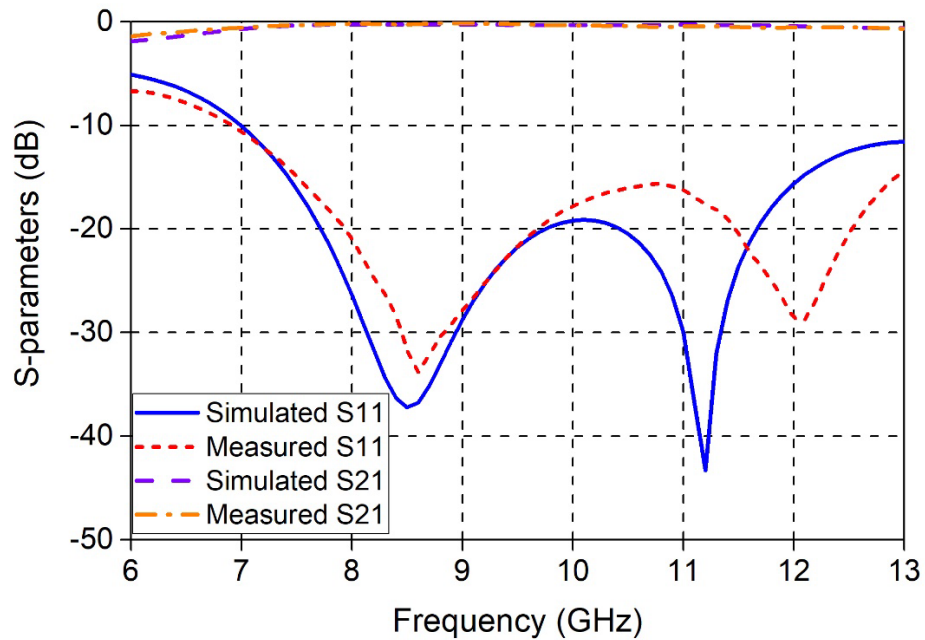


Figure 3.3: Simulated and measured S-parameters of the back-to-back microstrip line to outer waveguide transition.

3.2 Inner Waveguide Feeding Network

For the inner waveguide transition, microstrip line to SIW transitions in [3], [26], [27] and [28] can be directly applied here. In this thesis, the tapered microstrip to SIW transition in [3] is used for its wide bandwidth and easy fabrication. For the inner waveguide measurement at high frequencies, the $50\ \Omega$ microstrip line will exhibit higher order mode [23], and the $75\ \Omega$ microstrip line is used instead. Since the impedances of $75\ \Omega$ microstrip line and inner waveguide with width $W_i=2.54\ \text{mm}$ are very close to each other, a direct connection without tapering structure between them is used. The design parameters of the inner waveguide to microstrip line transition are $W_{ms}=0.61$, $W_i=2.54\ \text{mm}$, $L_i=2.54\ \text{mm}$, and the total MCW length is $L_{tot}=13.21\ \text{mm}$ as shown in Figure 3.4. The extended length of inner waveguide is used to minimize the potential coupling between microstrip line and outer waveguide.

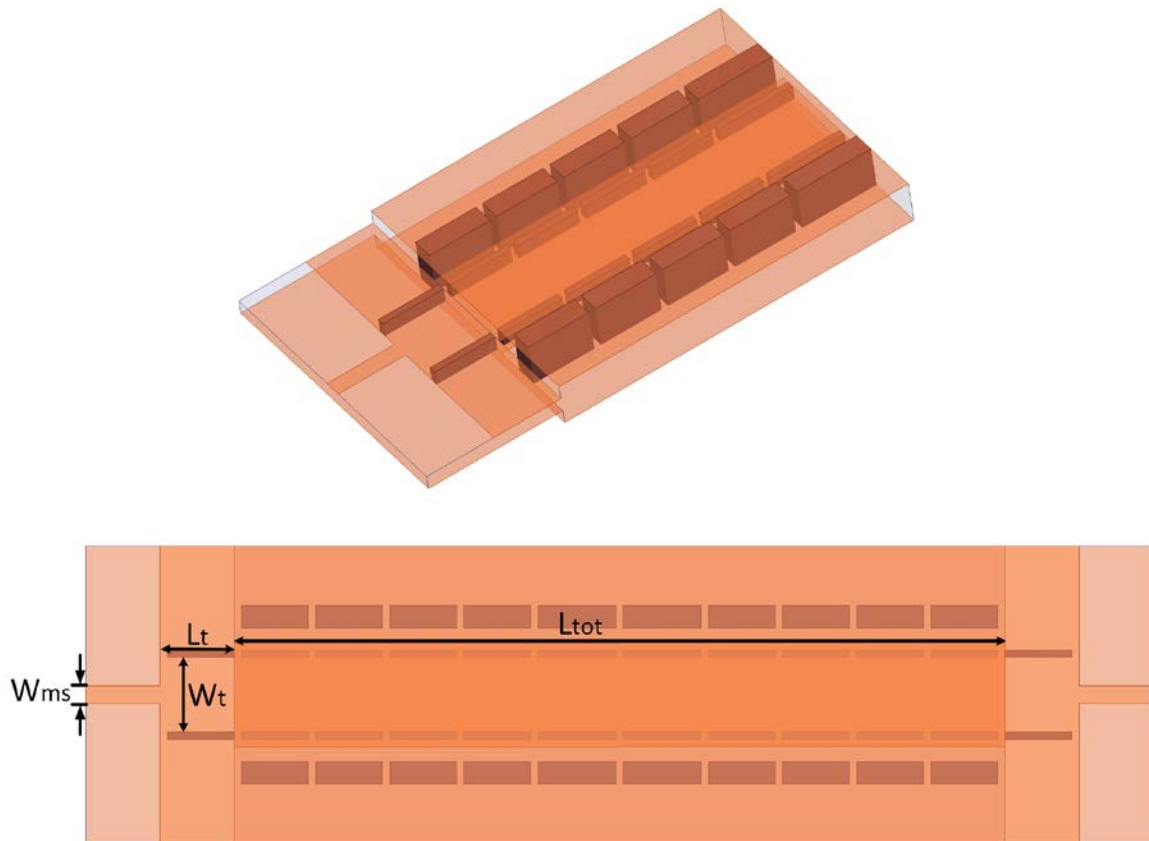
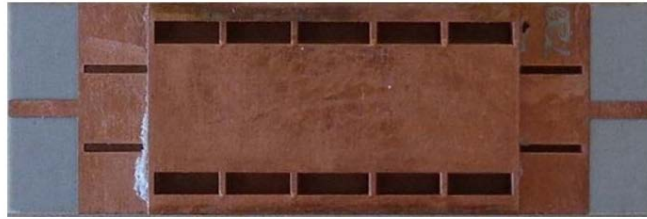
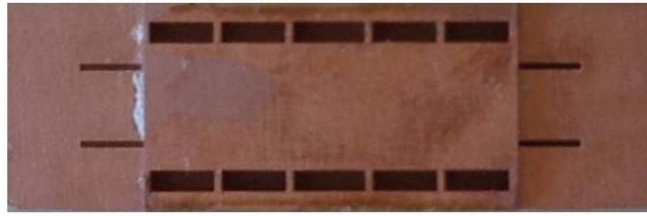


Figure 3.4: 3D view and dimensions of the microstrip line to inner waveguide transition.



(a)



(b)

Figure 3.5: Pictures of the front side (a) and back side (b) of the fabricated microstrip to inner waveguide transition.

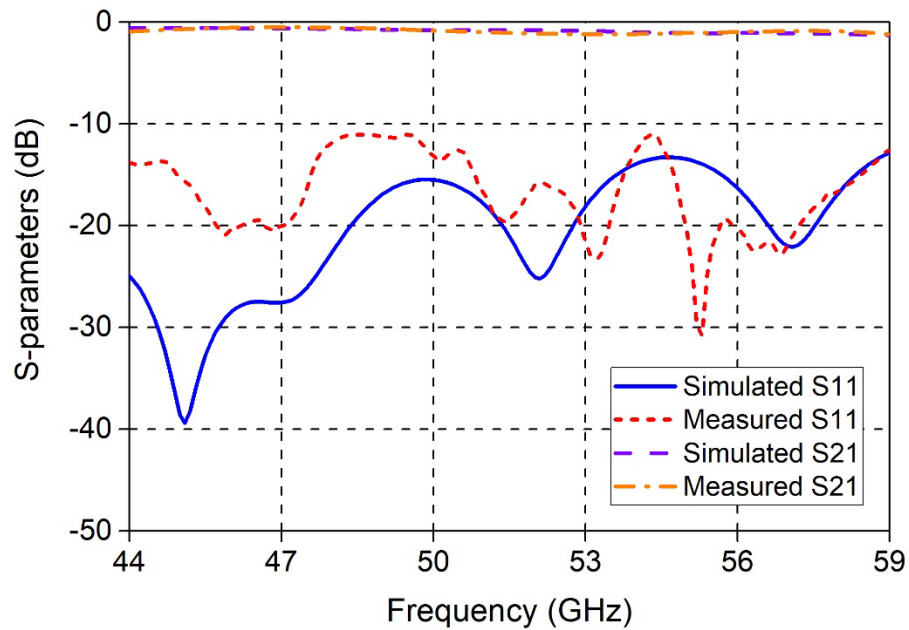


Figure 3.6: Simulated and measured S-parameters of the back-to-back microstrip line to inner waveguide transition.

The fabricated microstrip line to inner waveguide transition in back to back is shown in Figure 3.5. TRL calibration is used to de-embed the connector effect in the two-port measurement. The simulated and measured results are in a good agreement as shown in Figure 3.6. Good matching of the transition at high frequency is achieved from 44 GHz to 59 GHz ($S_{11} < -10$ dB), and total insertion loss (including two back-to-back transitions and a certain length of inner waveguide) is better than -1.2 dB during operation band. The larger insertion loss compared to the outer waveguide transition is mainly due to the higher loss at higher frequency band.

3.3 Type I MCW Joint Feeding Network

3.3.1 Feeding Network Design

To use both the inner and outer waveguides at the same time for different applications, type I joint feeding network for the MCW is first proposed. This joint feeding network is also constructed on the same platform as the MCW, using three layers of 0.508 mm thick RT/Duroid 6002 substrates. In this demonstration, the operation frequency of the inner waveguide is shifted downward to facilitate the fabrication and measurement of the triple layer circuit. To lower the cutoff frequency of the inner waveguide of MCW, the width $W_i=4.37$ mm is selected here, and the outer waveguide width is then increased to $W_o=6.4$ mm correspondingly to maintain the same side distance between the inner and outer vias. In this design, the aforementioned inner and outer waveguide transitions are combined together into a single joint feeding network as shown in Figure 3.7 (circuit dimensions are: $W_{ms}=1.32$ mm, $W_{i1_o}=5.38$ mm, $W_{i2_o}=0.76$ mm, $L_{t_o}=8.76$, $W_{t_i}=1.93$ mm, $L_{t_i}=1.27$ mm, $L_p=1.37$ mm $W_p=1.37$ mm, $L_{s_i}=5.97$ mm, $L_{s_o}=6.73$ mm, $W_i=4.37$ mm, $W_o=6.4$ mm, $L_{tot_i}=24.79$ mm and $L_{tot_o}=35.56$ mm). The dimensions of joint feeding network are determined by the selection of lower and higher frequency bands for the MCW.

In the joint feeding network, the outer waveguide is still transitioned to the microstrip line along the direction of propagation, while the inner waveguide is transitioned to the microstrip line from the side through a right-angle bend structure. For the inner waveguide, the bend effect is canceled by the introduction of an inductive post (0.508 mm in diameter) near the corner. Because the inner waveguide also acts as the inner conductor of the outer waveguide, this bend structure will also affect the outer waveguide performance. To solve this issue, the outer waveguide side stub is short terminated around a quarter of its electrical wavelength at the transition center frequency. The

electric wall for the short termination is achieved by introducing vias at the bottom and top layers (as shown in Figure 3.7), so the signal propagation of the inner waveguide at the middle layer will not be affected.

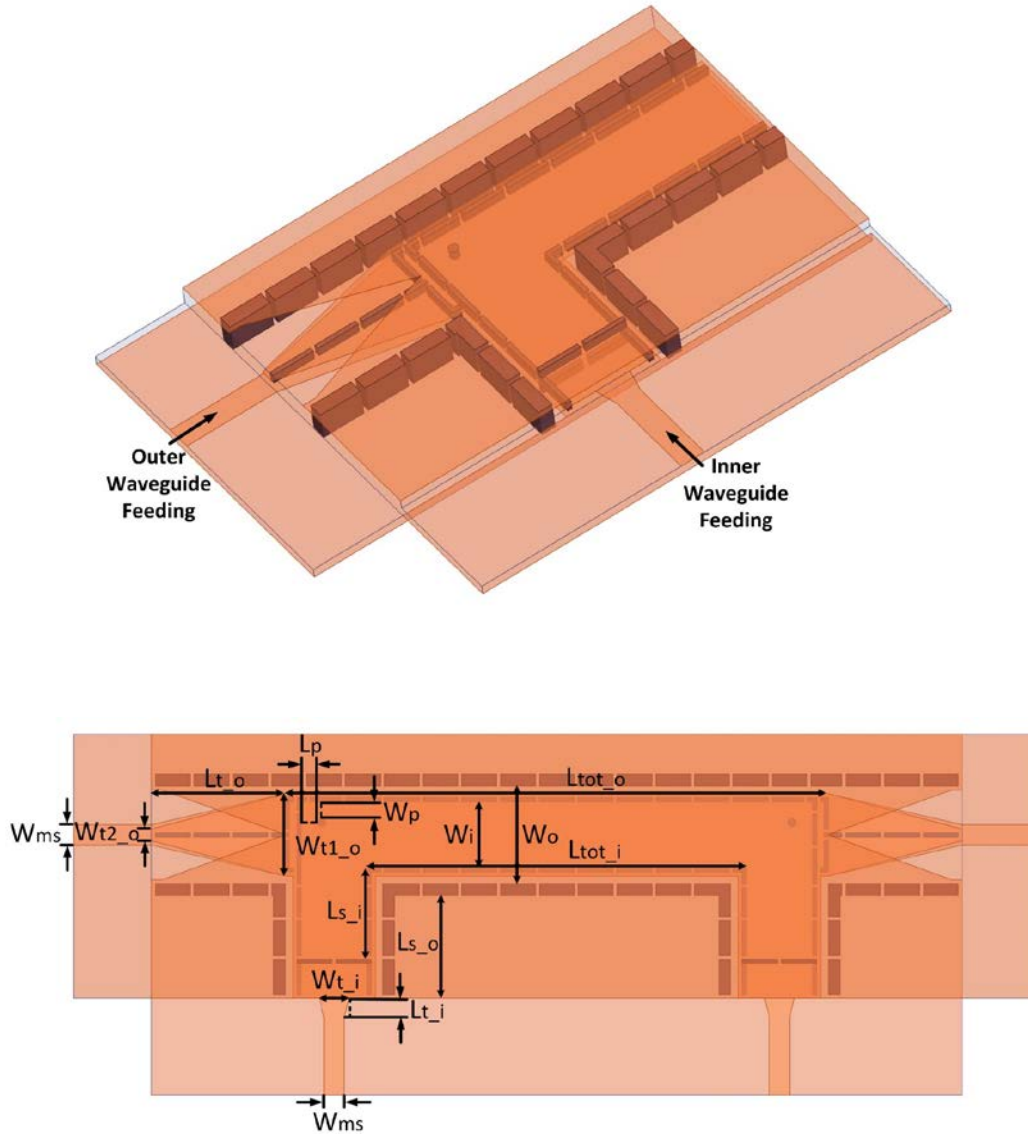
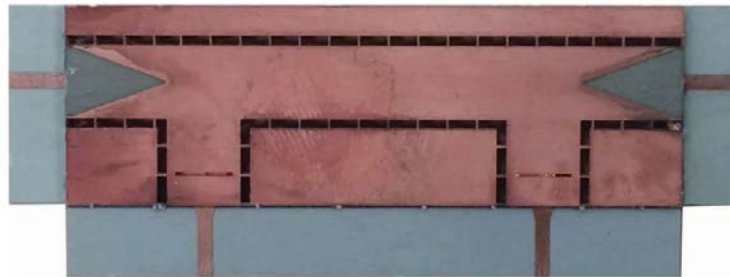


Figure 3.7: 3D view and dimensions of type I MCW joint feeding network.

3.3.3 Fabrication and Measurement

The pictures of fabricated type I MCW joint feeding network in back-to-back setup is shown in Figure 3.8. The circuit is connected to the vector network analyzer (VNA) for measurement using our home-made movable fixtures in Poly-Grames Research Center (shown in Figure 3.9), where any fixture angle combination can be easily achieved. The four-port circuit is measured using a two-port VNA, where each pair of ports is measured with the rest ports terminated with standard 50Ω loads as shown in Figure 3.9. The two-port TRL calibration is used to de-embed the connector effect in measurement.



(a)



(b)

Figure 3.8: Pictures of the front side (a) and back side (b) of the fabricated MCW.

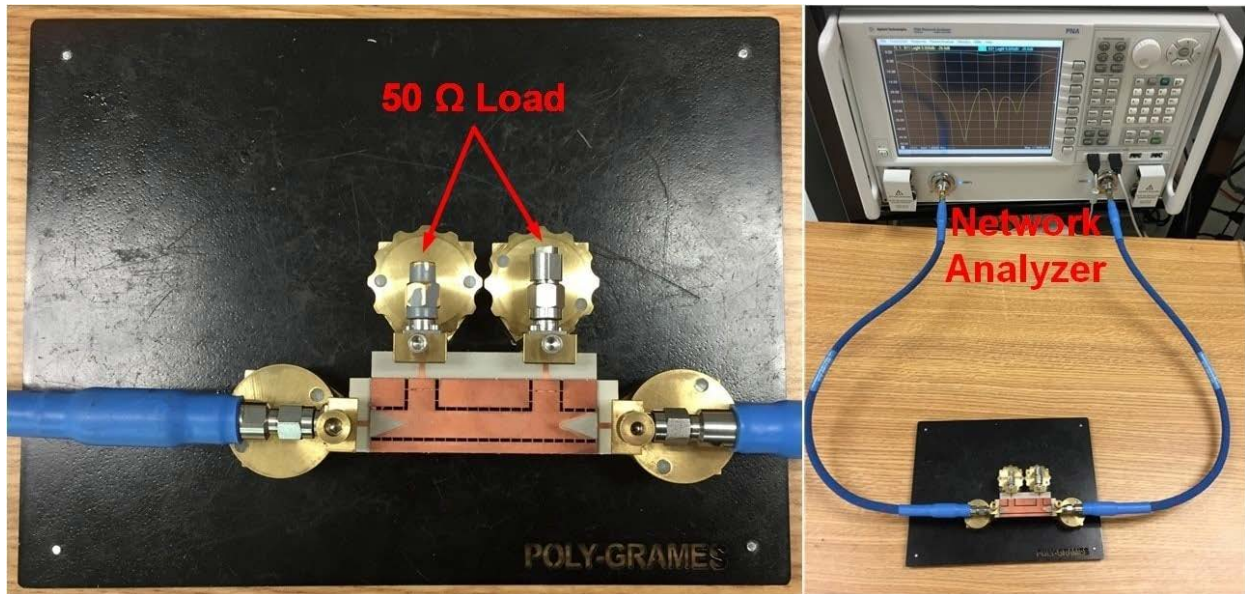


Figure 3.9: MCW four-port back-to-back measurement setup

The simulated and measured results for outer waveguide at low frequency band are shown in Figure 3.10, where a good

agreement is achieved within the operation band. Good matching is achieved from 7.6 GHz to 10.6 GHz with a relative bandwidth of 33% for the outer waveguide transition (shown in Figure 3.10). Due to the bandwidth limiting nature of the outer waveguide stub, the bandwidth of the type I joint feeding network for low frequency operation is narrower compared to the previous direct outer waveguide to microstrip line transition. When the MCW is excited from the two outer waveguide ports on the left and right, the corresponding E field distribution in the circuit is also plotted in Figure 3.10, where the TEM mode signal is propagating only in the outer waveguide.

The simulated and measured results for inner waveguide at high frequency band are shown in Figure 3.11, where a good agreement is achieved within the operation band. Good matching is achieved from 26 GHz to 38.2 GHz with a relative bandwidth of 38% for the inner waveguide transition (shown in Figure 3.11). When the MCW is excited from the two inner waveguide ports from the side, the corresponding E field distribution in the circuit is also plotted in Figure 3.11, where the TE_{10} signal is propagating only in the inner waveguide.

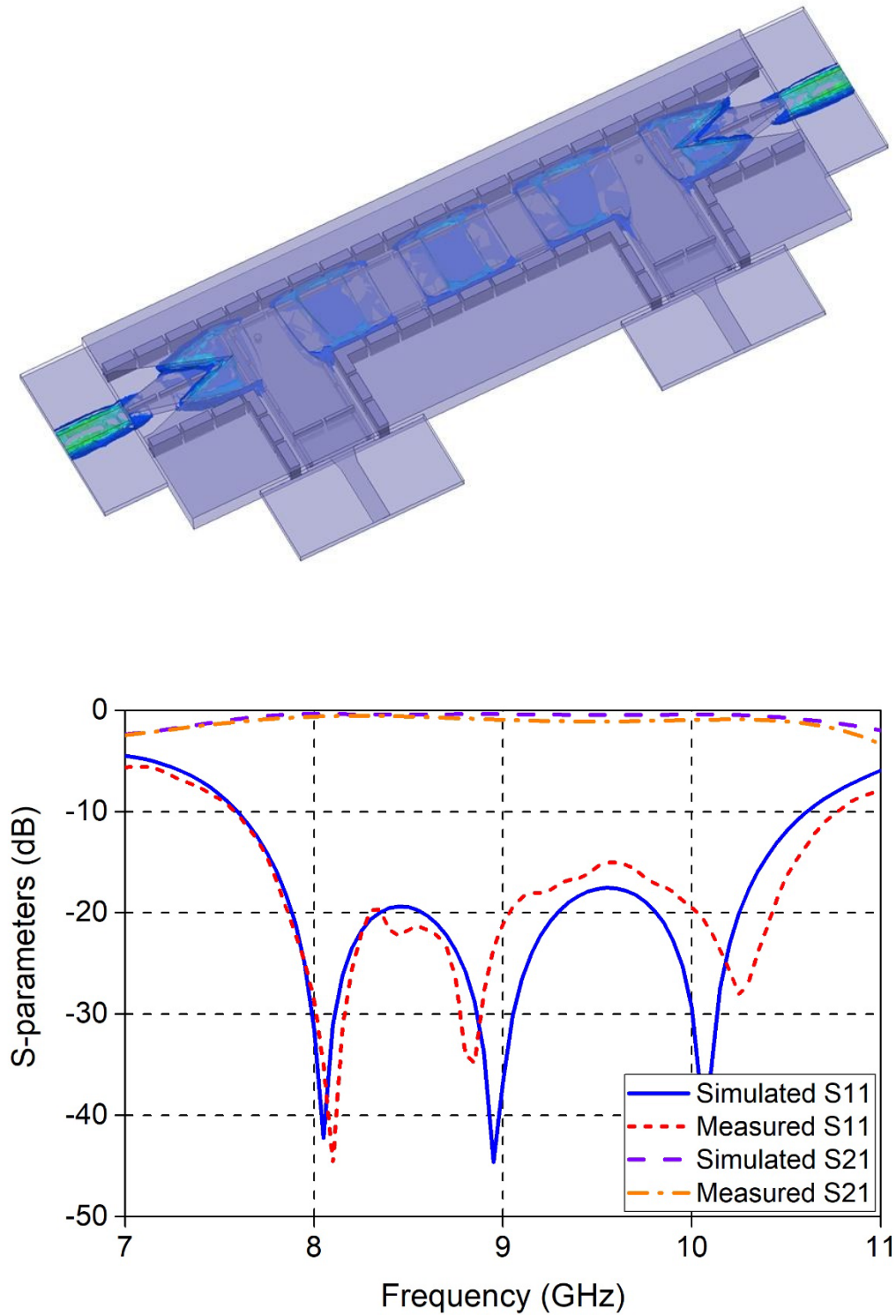


Figure 3.10: Simulated E field distribution at 9 GHz (top), and simulated and measured S-parameters of the type I MCW joint feeding network for low frequency operation (bottom).

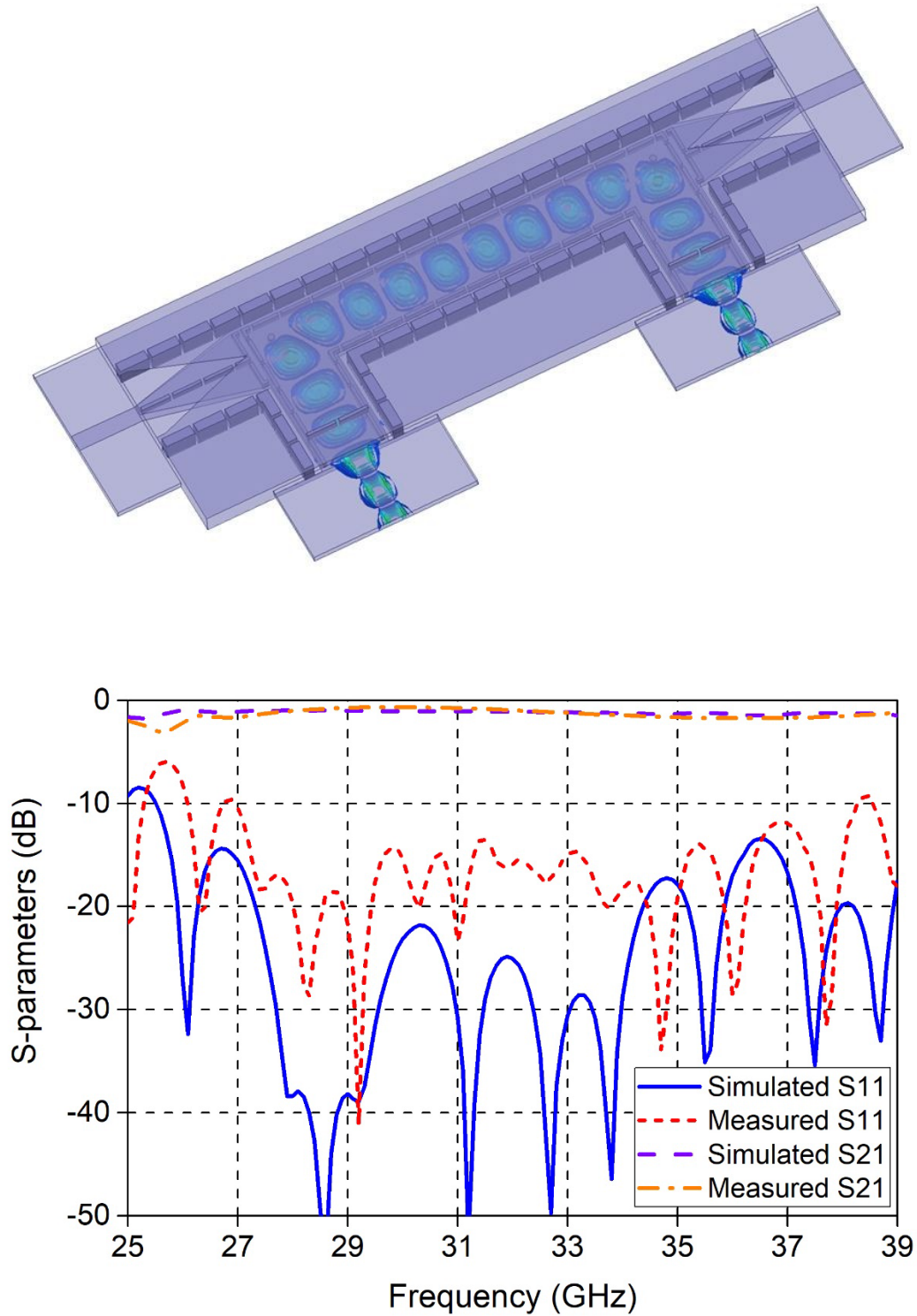


Figure 3.11: Simulated E field distribution at 33 GHz (top), and simulated and measured S-parameters of the type I MCW joint feeding network for high frequency operation (bottom).

3.4 Type II MCW Joint Feeding Network

3.4.1 Feeding Network Design

In the previous section, the type I joint feeding network for MCW was presented with its outer waveguide operating for a low frequency region and the inner waveguide operating for a high frequency region, respectively. This joint feeding network successfully integrates the inner and outer waveguide transitions into a single triple layer structure, allowing the simultaneous feeding of both waveguides of MCW without interference. However, due to the use of an outer waveguide quarter wavelength stub in the design, the bandwidth of outer waveguide operation frequency is inevitably limited. Besides band limitation in the outer waveguide feeding, the inner waveguide feeding structure is also an indivisible part of the outer waveguide feeding, which significantly increases its design complexity.

To solve this issue and improve the feeding network performance, a type II joint feeding network is proposed here for the simultaneous feeding of the inner and outer waveguide of MCW. This joint feeding network is also constructed on the same platform as the MCW, using three layers of 0.508 mm thick Rogers RT/Duroid 6002 substrates, and its dimensions are shown in Figure 3.12. Based on the selection of MCW lower and higher operation bands, the inner waveguide width $W_i=9.29$ mm is selected, under which the center frequency of the outer waveguide is set at 9 GHz and the inner waveguide is at 18 GHz for demonstration purpose. The dimensions of type II MCW joint feeding are: $W_{ms1}=1.32$ mm, $L_{adp}=3.81$ mm, $L_{ms1}=9.68$ mm, $D_{ms}=4.57$ mm, $L_{slot}=10.29$ mm, $W_{slot}=0.3$ mm, $D_{slot}=1.47$ mm, $W_{ms2}=0.76$ mm, $L_{stub}=4.67$ mm, $L_{ms2}=6.38$ mm, $L_{b1}=1.02$ mm, $L_{b2}=1.27$ mm, $L_{ms3}=5.08$ mm, $W_{ms3}=2.21$ mm, $L_p=2.46$ mm, $L_{to}=4.57$ mm, $W_{to}=7.82$ mm, $W_o=9.32$ mm, $W_i=9.29$ mm, $W_{ti}=2.44$ mm, $L_{ti}=2.77$ mm, $L_{gap}=0.25$ mm, $L_{via}=2.54$ mm.

For the inner waveguide feeding structure, the inner waveguide is first transitioned to the side through a right-angle bend structure similar to type I joint feeding network, where the bending effect is canceled by an inductive post (0.508 mm in diameter) at the corner. Then, it is further transitioned to a microstrip line for measurement purpose through a widely used taper structure for mode and impedance matching [29].

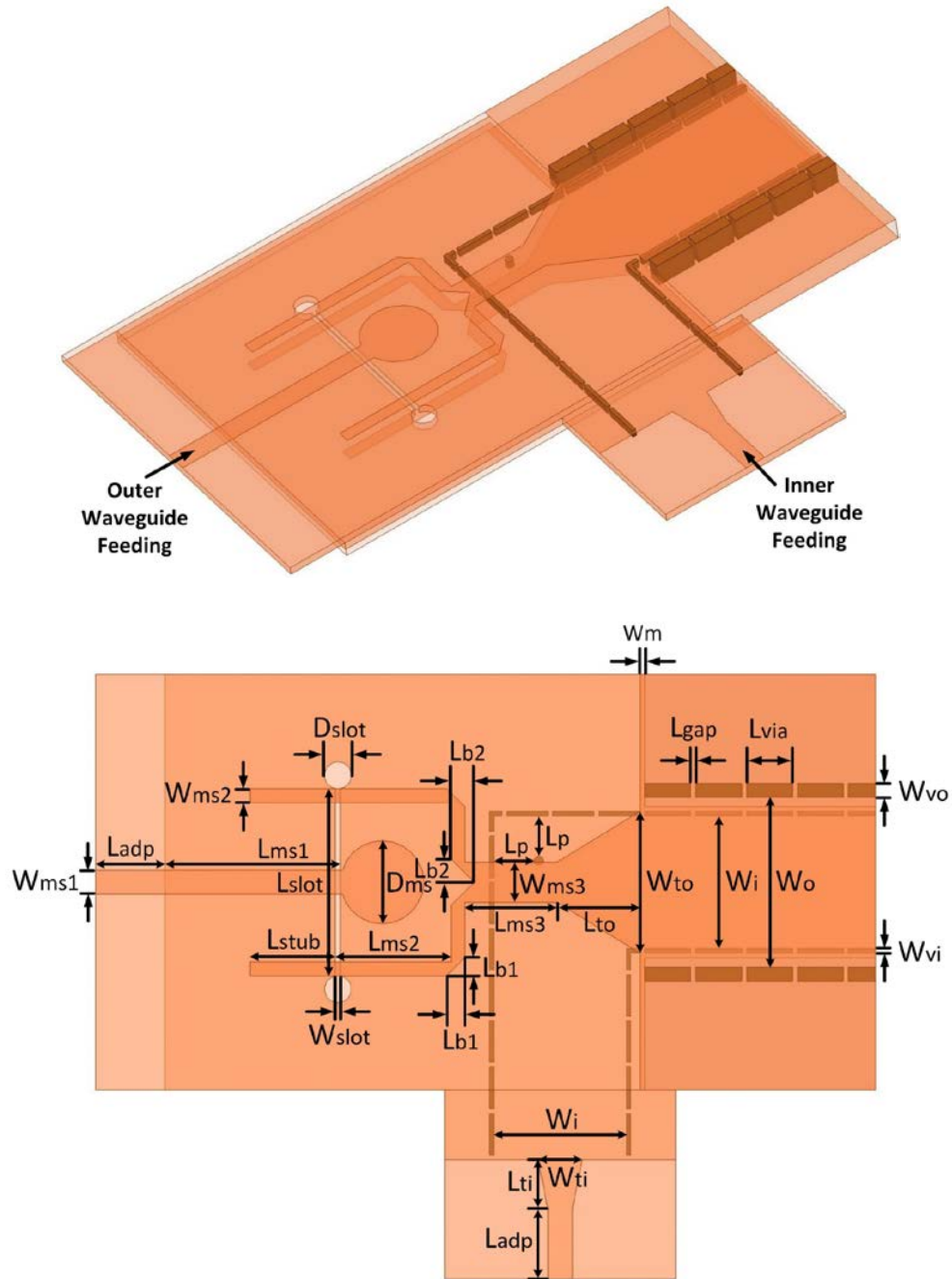


Figure 3.12: 3D view and dimensions of the type II joint feeding network.

For the outer waveguide feeding structure, it consists of a multilayer power divider in series with a dual taper structure. As analyzed in chapter 2, when the outer waveguide operation band is close to or overlapping with the inner waveguide operation band, the 1st and 2nd higher order modes of the outer waveguide will appear. In this case, higher order mode suppression is essential in the

feeding network design. The proposed mode suppression method comes from the observation of the outer waveguide's fundamental and higher order mode patterns (shown in Figure 3.13). From (b) and (c) in Figure 3.13, both the outer waveguide fundamental and 1st higher order modes are horizontally symmetrical, so a symmetrical excitation at the center may excite both modes simultaneously. To suppress the 1st higher order mode, two excitations with equal magnitude and opposite E -field orientation are introduced from the top and bottom layers simultaneously, resembling the E -field distribution of the fundamental mode. With this excitation arrangement, the excited fundamental modes from the top and bottom layers will add up to each other, while the excited 1st higher order modes will cancel out each other, achieving the perfect 1st higher order mode suppression. From (d) in Figure 3.13, the outer waveguide 2nd higher order mode is horizontally asymmetrical; therefore, it is intrinsically suppressed by this horizontally symmetrical feeding.

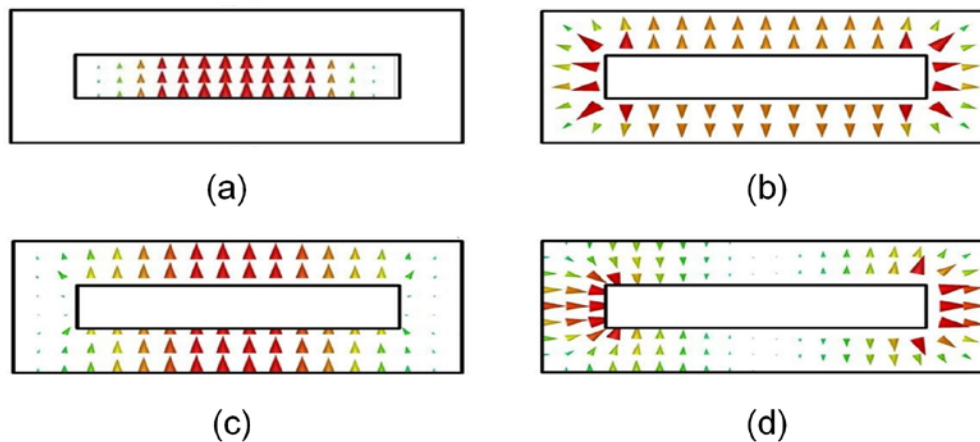


Figure 3.13: Fundamental modes of the inner (a) and outer (b) waveguides, and the first two higher order modes of the outer waveguide (c) and (d).

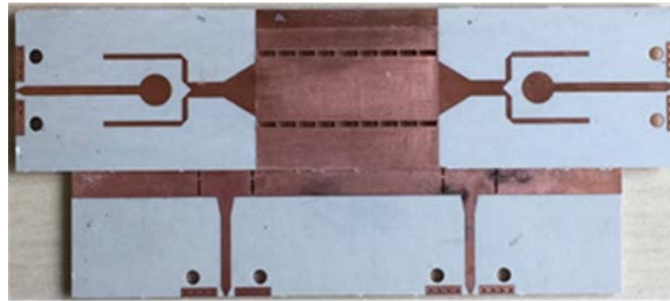
To achieve this excitation scheme, the input signal shall be equally divided into the top and bottom layers with exact 180 phase difference through a multilayer power divider. Slotline transitions are widely used in multilayer power dividers to achieve via-less vertical power transitions [30], [31] and [32]. Most of the multilayer power dividers are constructed on an even number of substrate layers (two or four layers, for example), where the slotline is directly etched

on the metal surface. However, this feeding network consists of three layers, therefore, a 3D slotline is designed in this case. Instead of etching on the metal surface, this 3D slotline is carved on the middle substrate layer with all its side walls metalized using conventional via metallization technique. The input microstrip line signal is first coupled to the 3D slotline and then equally coupled to the four output microstrip lines at the top and bottom. In order to obtain a flat frequency response, the input microstrip line is terminated by an open circular stub. The 3D slotline is about a half wavelength long, and terminated by two short circular stubs. The four symmetrically positioned microstrip lines extend about a quarter wavelength over the slotline to achieve the optimal coupling on one end, and combined into two identical wider microstrip lines on the top and bottom through a microstrip line T-junctions on the other end, respectively. Under this arrangement, the combined signals on the top and bottom layers are of equal magnitude and 180 phase difference. At last, they are fed from the top and bottom into the outer waveguide through a dual taper structure, where it is optimized to provide both the impedance and mode matching.

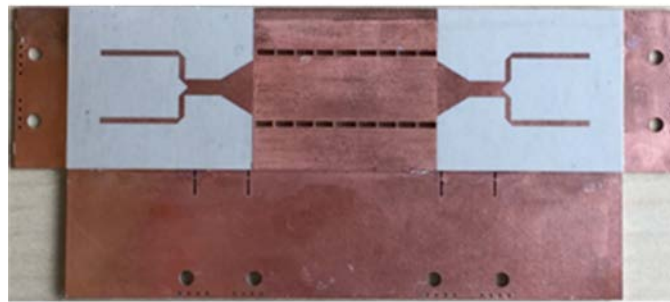
In this feeding network, the outer waveguide feeding structure is solely confined in the top and bottom layers except for the dumbbell shaped slot; while the inner waveguide feeding structure is solely confined in the middle layer. Therefore, as long as the dumbbell shaped slot is positioned on the left of the bend structure of the inner waveguide, the two feeding structures can be independently designed. Also, due to its higher order modes suppressing nature, this feeding network can be implemented in an arbitrary combination of the inner and outer waveguide operation bands, regardless of the higher order mode cutoff frequencies in the outer waveguide.

3.4.2 Fabrication and Measurement

The feeding network measurement was performed using a two port VNA and four Southwest End Launch connectors, where TRL calibration is used to de-embed the connector effects. Pictures of the fabricated type II MCW joint feeding network in back to back setup are shown in Figure 3.14, where extra screw holes are also fabricated to adopt the connectors.



(a)



(b)

Figure 3.14: Pictures of front (a) and back (b) of the fabricated joint feeding network.

When the left and right ports are excited, the signal is coupled to the top and bottom layers, and feed into the outer waveguide (shown in Figure 3.15). The simulated and measured S-parameters are shown in Figure 3.15, and they agree well with each other. Good matching is achieved in measurements for the outer waveguide feeding from 6.9 GHz to 11.8 GHz ($S_{11} < -10$ dB) with a relative bandwidth of 54.5%.

When the two bottom ports are excited, the signal is coupled to the middle layer, and feed into the inner waveguide (shown in Figure 3.16). The simulated and measured S-parameters are also shown in Figure 3.16, and they also agree well with each other. Good matching is achieved in measurements for this inner waveguide feeding from 13.5 GHz to 24.1 GHz ($S_{11} < -10$ dB) with a relative bandwidth of 58.8%.

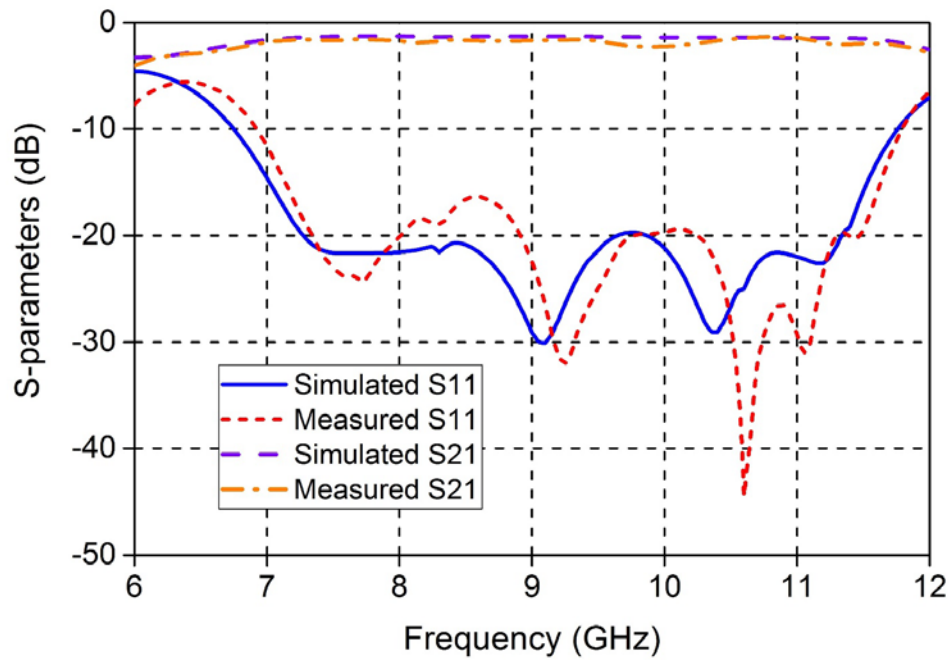
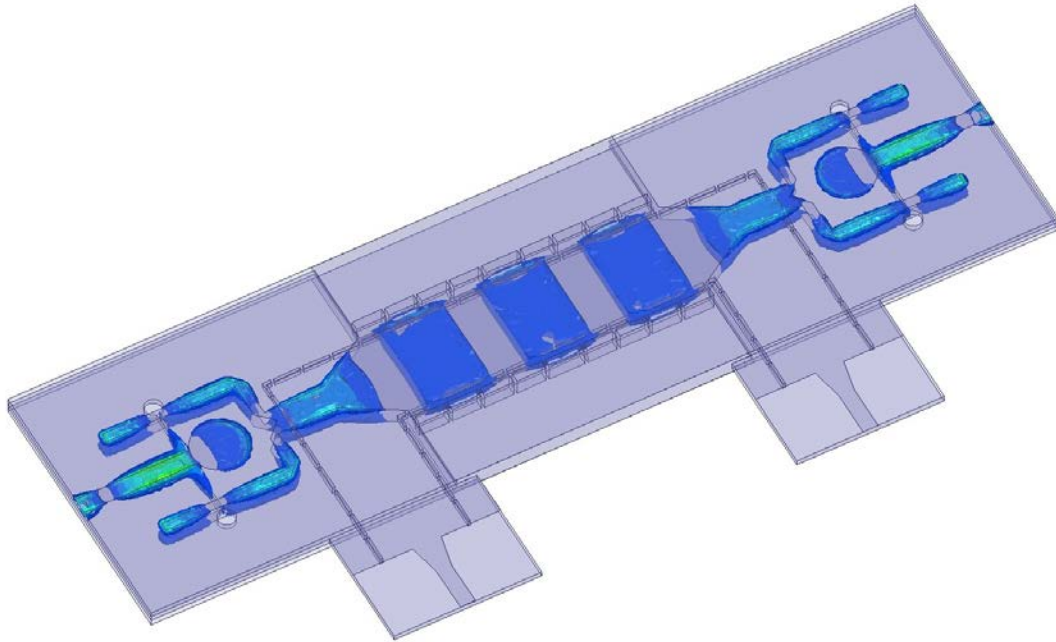


Figure 3.15: Simulated E field distribution at 9 GHz (top), and simulated and measured S-parameters of the type II MCW joint feeding network for low frequency operation (bottom).

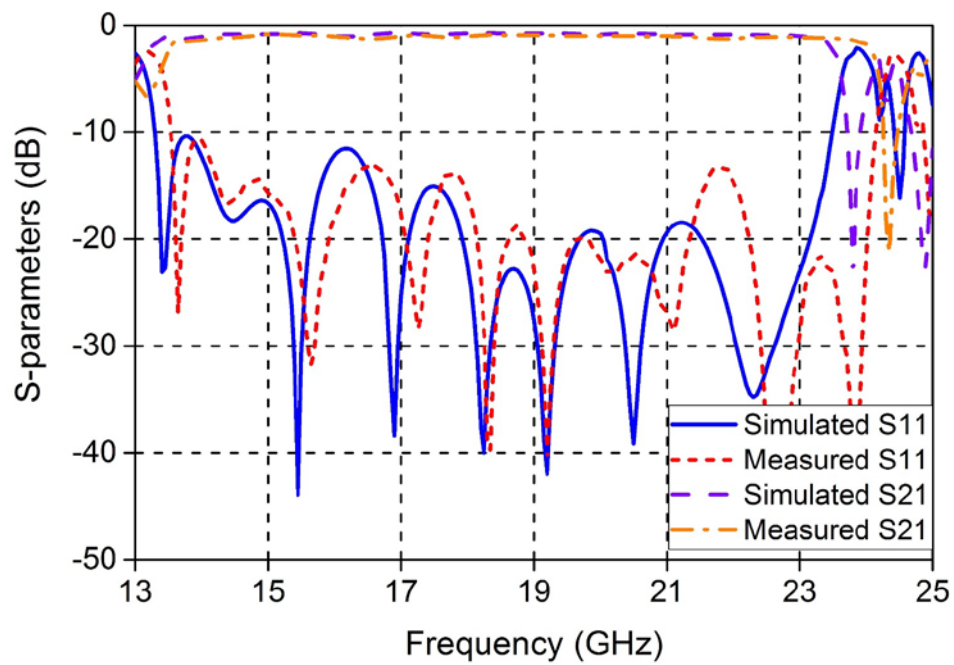
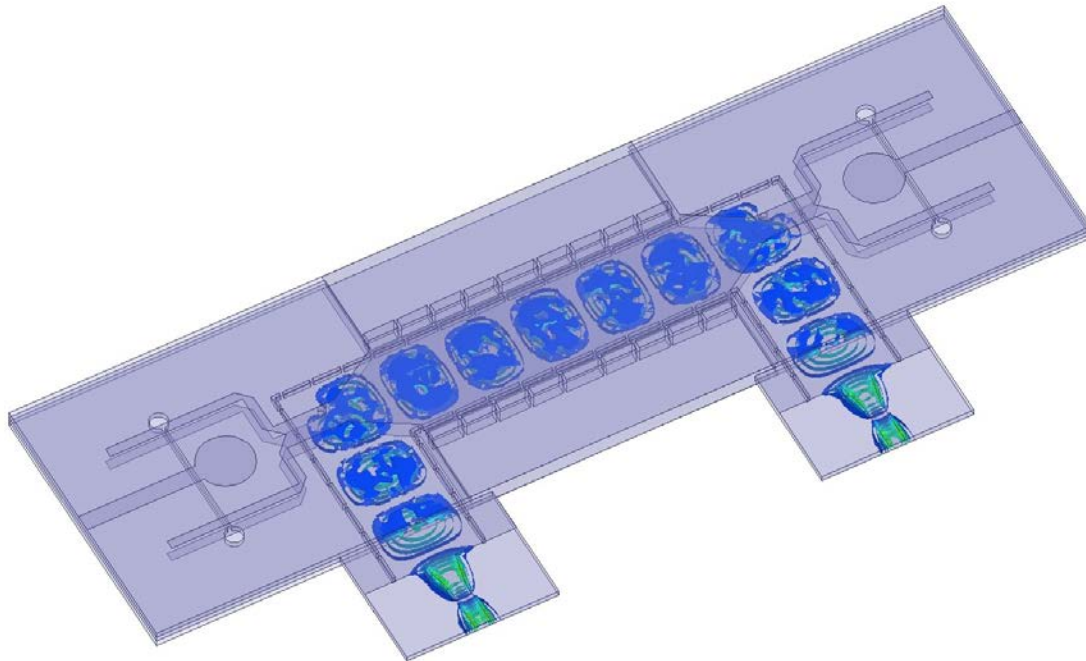


Figure 3.16: Simulated E field distribution at 19 GHz (top), and simulated and measured S-parameters of the type II MCW joint feeding network for high frequency operation (bottom).

3.5 Conclusion

In this chapter, various feeding networks for the inner and outer waveguides of MCW are proposed for measurement and circuit integration. Transitions from microstrip line to the inner and outer waveguides of MCW are presented in both standalone feeding networks and integrated joint feeding networks, respectively. Both the two-port and four-port circuits are measured using two-port VNA, and TRL calibration is used to de-embed the connector effect in measurement. Good agreements between the simulation and measurement are achieved, demonstrating the feeding networks' capability to excite the triple layer MCW from conventional single layer microstrip lines.

In comparison, the type I joint feeding network has narrower bandwidth of outer waveguide transition due to the use of outer waveguide quarter wavelength stub, while the type II feeding network has slightly higher insertion loss of outer waveguide transition due to extra radiation loss at the slotline in transition. The type I and type II joint feeding networks use similar feeding structures for the inner waveguide, therefore, similar performance in terms of bandwidth and loss are observed.

CHAPTER 4 MODE COMPOSITE WAVEGUIDE CIRCUITS

As described above, the MCW consists of an outer waveguide supporting fundamental mode of TEM and an inner waveguide supporting fundamental mode of TE_{10} (shown in Figure 4.1). One of the main advantage of MCW compared to other conventional transmission lines is that the signal can be optimally transmitted in either inner or outer waveguides depending on its operation frequency. The outer waveguide is suitable for lower frequency operation for its zero-cutoff frequency and compact size, while the inner waveguide is suitable for higher frequency operation thanks to its simple structure and low loss.

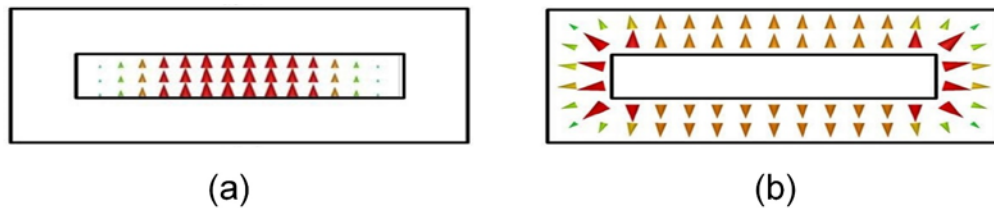


Figure 4.1: Two fundamental propagating modes in the MCW: (a) TE_{10} mode in inner waveguide and (b) TEM mode in outer waveguide.

Besides the optimal performance for both low and high frequency operation, the MCW also exhibits interesting propagation properties due to its dual-mode nature. The fundamental mode dispersion diagram of the inner and outer waveguides of MCW are shown in Figure 4.2. Two assistant dashed lines (one vertical and one horizontal) are also plotted in the figure, intersecting with the inner and outer waveguide propagation constant curves respectively. At the two intersecting points of the vertical line, signals of the inner and outer waveguides are operating at the same frequency, while with different propagation constants. At the two intersecting points of the horizontal line, signals of the inner and outer waveguides are operating with the same propagation constants, while at different frequencies. This dual propagation feature makes the MCW an excellent candidate for dual- or multi-band circuits applications.

Furthermore, as the inner waveguide in the center is completely enclosed by the outer waveguide, a perfect symmetry exists at the cross section. With this symmetry, the interaction between the inner and outer waveguides can be realized in all four directions, which provides a lot

of diversities in the MCW based circuit and antenna designs. To demonstrate the different properties of MCW in potential applications, MCW based circuits of directional coupler, dual-mode filter and magic tee are prototyped in our lab. In this chapter, the center frequency of 10 GHz is used for all the circuits due to the tradeoff between the circuit size and fabrication complexity.

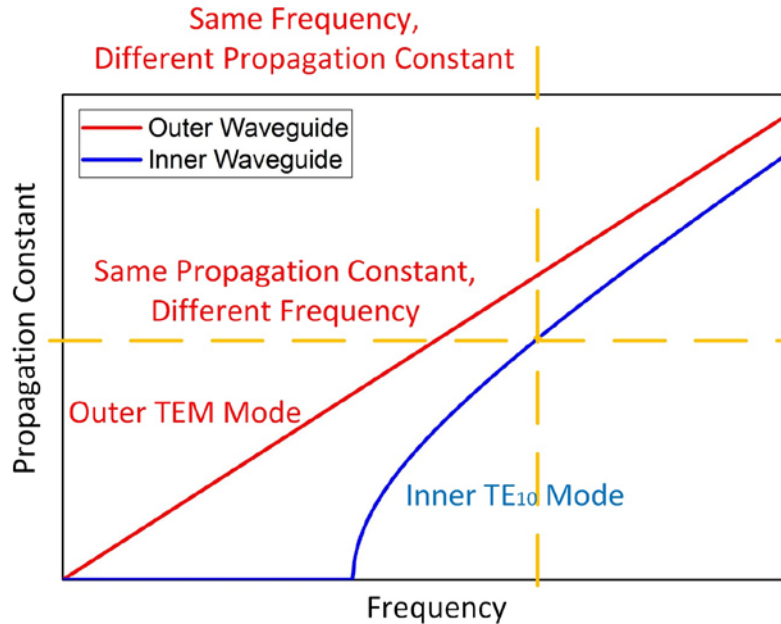


Figure 4.2: Dispersion diagram of the outer and inner waveguides of MCW.

4.1 MCW Directional Coupler

Directional couplers are widely used in various microwave applications for power routing and rerouting operations. The substrate integrated technique is widely used to implement planar directional couplers. Based on this technique, various single-layer SIW directional couplers [33] [34] and multi-layer SIW directional coupler [35] [36] were studied. In this section, a MCW directional coupler is presented, with TEM mode propagating in its outer waveguide and TE_{10} mode propagating in its inner waveguide. The mode conversion during the coupling between the inner and outer waveguides is studied. The generated higher order modes at the outer waveguide are suppressed using the proposed joint feeding network. Furthermore, the propagation constants in the inner and outer waveguides are not the same compared to the conventional counterparts. To achieve the desired signal addition and cancelation, the operation principle of the proposed coupler

is mathematically formulated, and the design methodology is developed. A -20 dB MCW backward directional coupler at 10 GHz is fabricated to demonstrate the proposed method.

4.1.1 Coupler Operation Principle

In a conventional two-hole directional coupler design, propagation constants in the two coupled waveguides are mostly identical ($\beta_I = \beta_{II}$, as shown in Figure 4.3). The coupling operation can be achieved in both forward and backward directions by properly choosing the hole distance and the aperture phase relation [23].

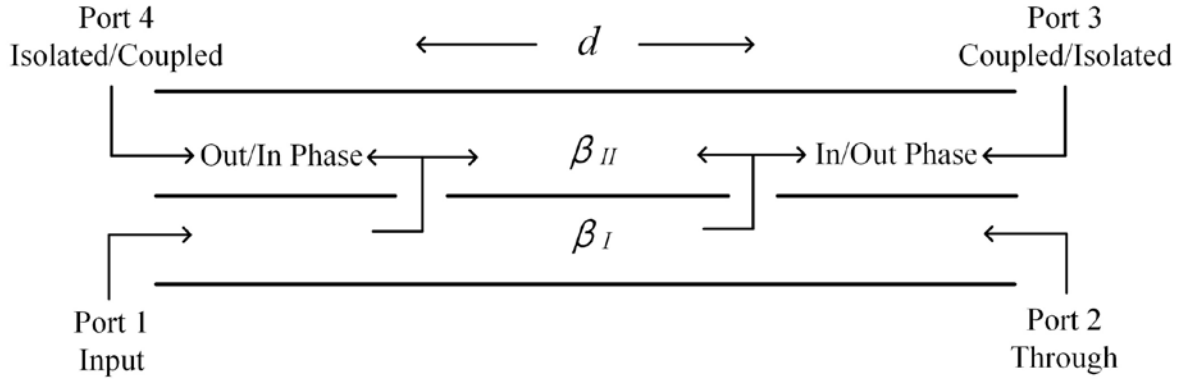


Figure 4.3: Diagram of a general two-hole directional coupler.

For the proposed MCW directional coupler, however, both modes and propagation constants of the inner ($\beta_I = \beta_{in}$) and outer ($\beta_{II} = \beta_{out}$) waveguides are different. In [19], SIW directional couplers with the same modes but different propagation constants were discussed. In this work, the MCW directional coupler operation principle is discussed and studied under its dual mode propagating scenario. To realize the power summation and cancellation required for coupling operation, the design equations of the MCW forward directional coupler are

$$\beta_{out}d + \beta_{in}d = (2N_1 + 1)\pi \quad (3.1)$$

$$\beta_{out}d - \beta_{in}d = 2N_2\pi \quad (3.2)$$

where $N_1 = 0, 1, 2, 3, \dots$, $N_2 = 0, 1, 2, 3, \dots$, and $N_1 \geq N_2$.

In equation (4.1), the two backward coupled signals are 180° out of phase, creating the signal isolation at port 4. And in equation (4.2), the two forward coupled signals are in phase, creating the signal summation at port 3. The condition $N_1 \geq N_2$ guarantees a physically realizable solution with positive propagation constants for both the inner and outer waveguides.

Similarly, the MCW backward directional coupler can also be realized by satisfying the phase conditions in the coupler design equations with the backward operation. The MCW backward directional coupler design equations are

$$\beta_{out}d + \beta_{in}d = 2N_1\pi \quad (3.3)$$

$$\beta_{out}d - \beta_{in}d = (2N_2 + 1)\pi \quad (3.4)$$

where $N_1=1, 2, 3, \dots$, $N_2=0, 1, 2, 3, \dots$, and $N_1 > N_2$.

In equation (4.3), the two backward coupled signals are in phase, creating the signal summation at port 4. And in equation (4.4), the two forward coupled signals are 180° out of phase, creating the signal isolation at port 3. The condition $N_1 > N_2$ guarantees a physically realizable solution with positive propagation constants for both the inner and outer waveguides.

4.1.2 Coupler Analysis and Design

To demonstrate the proposed method, a MCW backward directional coupler at 10 GHz is designed. Similar to MCW, the coupler is also constructed on three layers of 0.508 mm thick Rogers 6002 substrate using multilayer substrate integrated technique. Once the operation frequency and substrate are selected, the outer waveguide propagation constant can be calculated by

$$\beta_{out} = 2\pi f \sqrt{\mu\epsilon} \quad (3.5)$$

where μ and ϵ are the permeability and permittivity of the substrate, and f is the operation frequency.

By solving equations (4.3) and (4.4) for the backward coupler operation, the other two design parameters β_{in} and d can be acquired. Table 4.1 shows the design parameters for both forward and backward MCW directional couplers.

Table 4.1: Design parameters of MCW forward and backward directional couplers.

MCW Forward Directional Coupler				
N_1	N_2	$\beta_{out} (rad/m)$	$\beta_{in} (rad/m)$	$d (mm)$
1	1	359	72	8.92
2	1	359	154	30.61
3	1	359	200	39.34
2	2	359	40	39.34
3	2	359	98	48.08
MCW Backward Directional Coupler				
N_1	N_2	β_{out}	β_{in}	$d (mm)$
1	0	359	120	13.1
2	0	359	216	21.84
3	0	359	257	30.61
2	1	359	51	30.61
3	1	359	120	39.34

In theory, there exists infinite pairs of N_1 and N_2 that can satisfy the coupling and isolation conditions, and the first several pairs of index which give the smallest distance parameter d are listed. The selection of coupler index N_1 and N_2 is a trade-off between the coupler size (related to d) and operation bandwidth (related to β_{in}). When larger N_1 and N_2 are selected, the calculated hole distance will increase, thus increasing the coupler physical size. While, when smaller N_1 and N_2 are selected, the calculated cutoff frequency of the inner waveguide will shift towards the operation frequency, thus decreasing the operation bandwidth. In our case, $N_1=2$ and $N_2=0$ are selected (shown in bold in Table 4.1) to solve equation (4.3) and (4.4).

When the index N_1 and N_2 are determined, the hole distance d and inner waveguide propagation constant β_{in} can then be calculated. The width of inner waveguide w is related to β_{in} as

$$\beta_{in} = 2\pi f \sqrt{\mu\epsilon} \sqrt{1 - \left(\frac{1}{2wf\sqrt{\mu\epsilon}}\right)^2} \quad (3.6)$$

Based on the calculations of two propagation constants of the inner and outer waveguides, a MCW backward directional coupler is designed as shown in Figure 4.4, where the coupler dimensions are: $D_{hole}=2.49 \text{ mm}$, $d=21.84 \text{ mm}$, $L_{tot}=45.72 \text{ mm}$, $W_{ms1}=1.32 \text{ mm}$, $L_{ms1}=12.33 \text{ mm}$, $D_{ms}=4.06 \text{ mm}$, $L_{slot}=10.29 \text{ mm}$, $W_{slot}=0.3 \text{ mm}$, $D_{slot}=1.47 \text{ mm}$, $W_{ms2}=0.76 \text{ mm}$, $L_{stub}=4.67 \text{ mm}$, $L_{ms2}=6.38 \text{ mm}$, $L_{b1}=1.02 \text{ mm}$, $L_{b2}=1.27 \text{ mm}$, $L_{ms3}=7.87 \text{ mm}$, $W_{ms3}=2.21 \text{ mm}$, $L_p=4.70 \text{ mm}$, $L_{to}=4.57 \text{ mm}$, $W_{to}=6.37 \text{ mm}$, $W_o=12.95 \text{ mm}$, $W_i=10.92 \text{ mm}$, $W_{ti}=2.41 \text{ mm}$, $L_{ti}=5.08 \text{ mm}$, $L_{adp}=6.35 \text{ mm}$, $W_m=0.25 \text{ mm}$, $W_{vo}=0.76 \text{ mm}$, $W_{vi}=0.25 \text{ mm}$, $L_{gap}=0.25 \text{ mm}$, $L_{via}=2.54 \text{ mm}$, $H_o=1.52 \text{ mm}$, $H_i=0.51 \text{ mm}$.

The power coupling between the inner and outer waveguides is achieved through two circular slots, where the power level can be controlled by adjusting their diameters. The levels of coupling power at different diameters of circular slots are simulated at 10 GHz as shown in Figure 4.5. According to the simulated design curve, the diameter of circular slots $D_{hole}=2.49 \text{ mm}$ is selected to achieve the -20 dB coupling between the inner and outer waveguide.

The fundamental modes of the inner and outer waveguides are TE_{10} and TEM modes, and the first two higher-order modes of the outer waveguide are folded TE_{20} I and folded TE_{20} II modes. Using the coupling slots at the top of inner waveguide, both the desired TEM and unwanted higher order modes will be excited in the outer waveguide.

To suppress the unwanted higher order modes, the type II joint feeding network is used for the excitation of the coupler. The simulated outer waveguide fundamental and higher order modes excited by the joint feeding network is shown in Figure 4.6, where the folded TE_{20} I mode is suppressed by 30 dB and folded TE_{20} II mode is suppressed by 54.4 dB at 10 GHz.

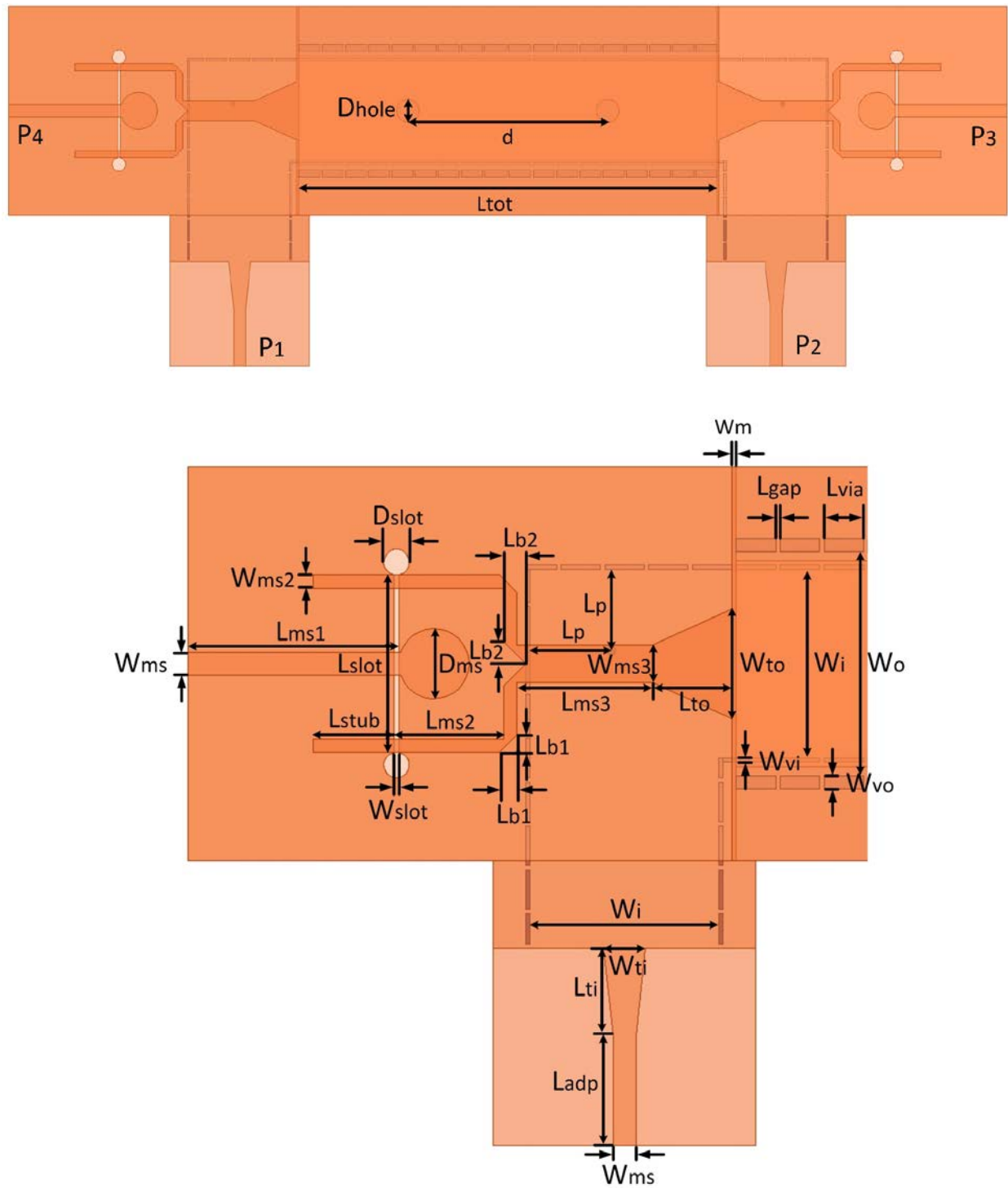


Figure 4.4: Dimensions of MCW backward directional coupler and its joint feeding network.

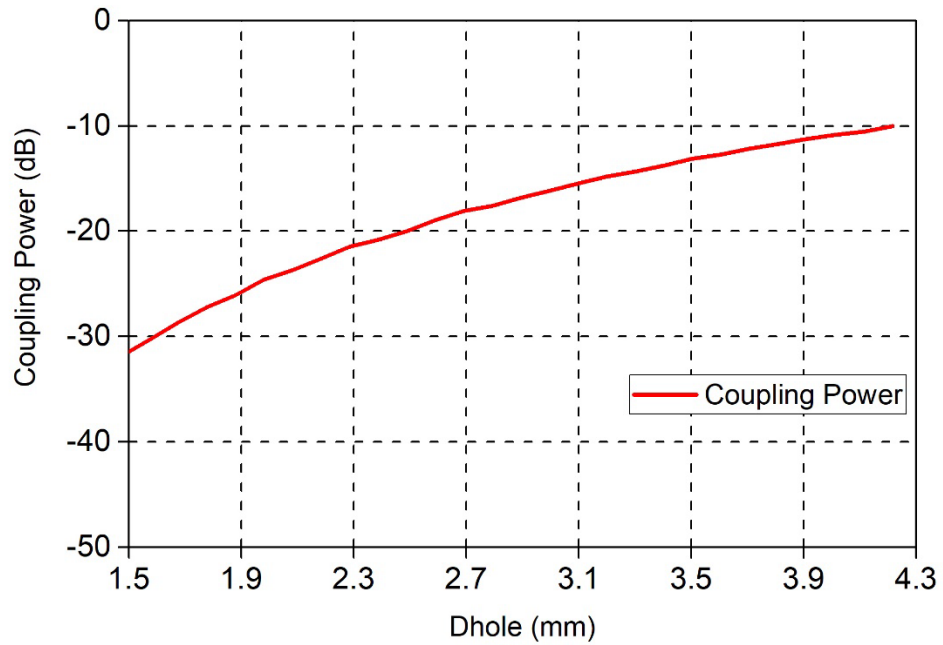


Figure 4.5: Simulated coupling power levels at different diameters of the circular slot at 10 GHz.

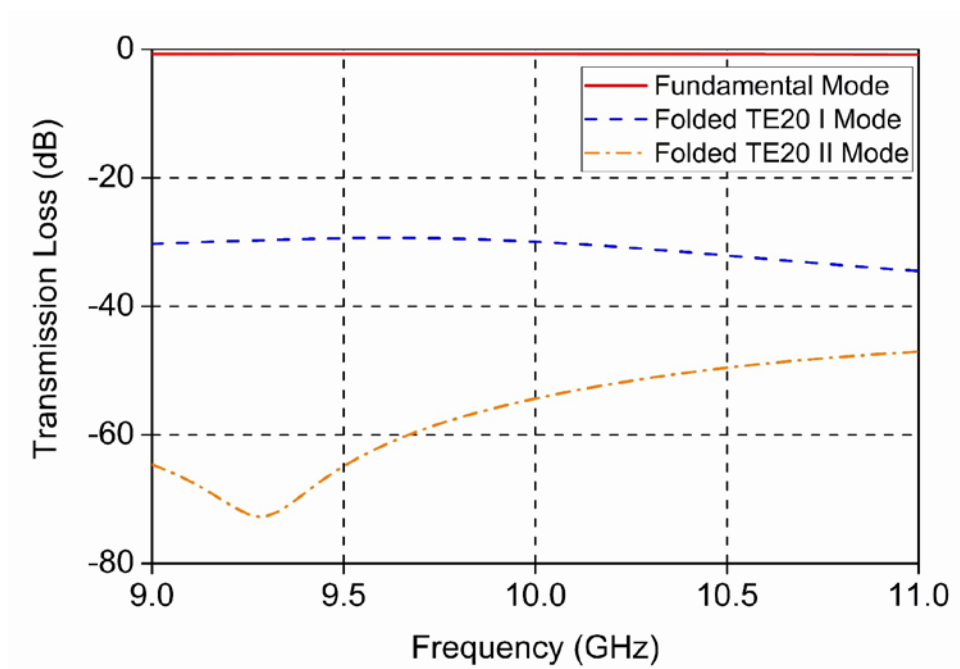


Figure 4.6: Simulated feeding network transmission loss of the outer waveguide's fundamental and higher order modes.

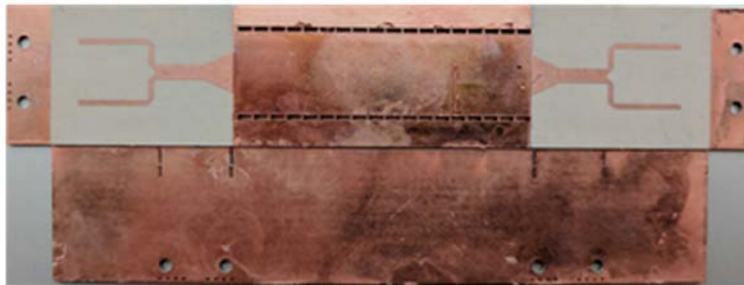
This higher-order mode suppression is achieved by creating different load conditions for each mode at the outer waveguide transition. For the fundamental TEM mode, it sees a through line at the transition, and the signal can go directly to the input and output ports. While for the folded TE₂₀ I mode and folded TE₂₀ II mode, they see an open at the transition, and the signals are completely reflected.

By adjusting the taper parameters L_{to} and W_{to} for outer waveguide and inductive post position parameter L_p for inner waveguide, the feeding network can be matched to the dimensions of the MCW used in the coupler. The final dimensions of the proposed MCW backward directional coupler are shown in Figure 4.4, and its corresponding parameters are also listed. The coupler is symmetrical from left to right, so only the dimensions of the left part are presented.

4.1.3 Fabrication and Measurement



(a)



(b)

Figure 4.7: Pictures of fabricated MCW backward directional coupler: (a) top view, (b) bottom view.

The fabricated MCW backward directional coupler is shown in Figure 4.7, where the left and right are the outer waveguide ports and bottom are the inner waveguide ports. Extra screw holes and edge vias are used for Southwest end launch connection, and TRL calibration is used to de-embed the connector effects.

Measured and simulated results of coupler insertion and return losses, as well as coupling and isolation are compared in Figure 4.8 and Figure 4.9, respectively. In Figure 4.8, good matching ($S_{11} < -20$ dB) is achieved in measurement during the operation frequency. In Figure 4.9, the fabricated coupler exhibits -20 dB power level coupling and the maximum measured isolation of -50 dB. Good agreement between the measurement and simulation is observed, and the difference is mainly caused by the fabrication tolerance of the triple layer circuit. In the fabrication, the three layers are glued together under high pressure, where the effects of the glue and possibly small air gap in between the layers are considered ideal in the simulation.

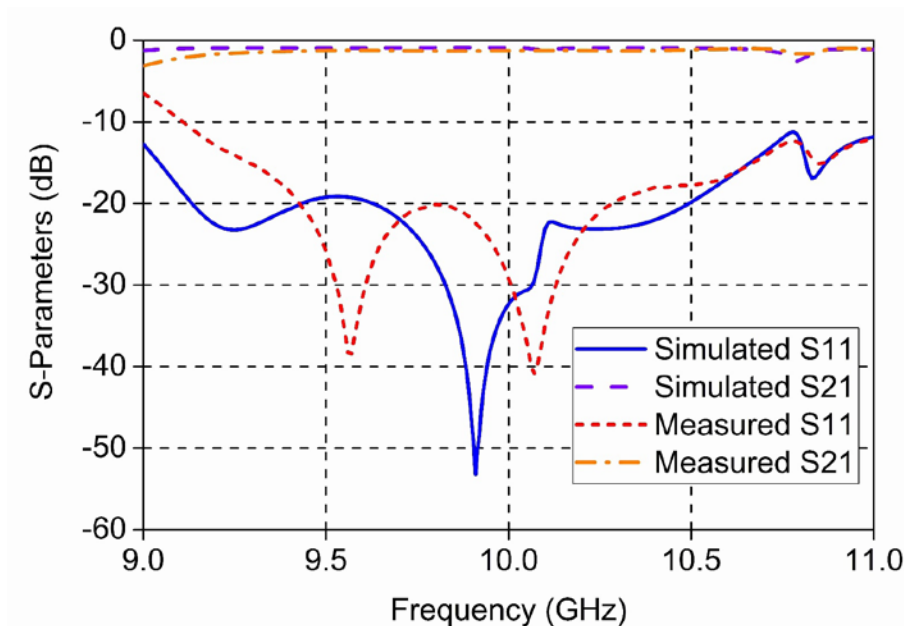


Figure 4.8: Comparison of measured and simulated MCW backward directional coupler return loss (S_{11}) and insertion loss (S_{21}).

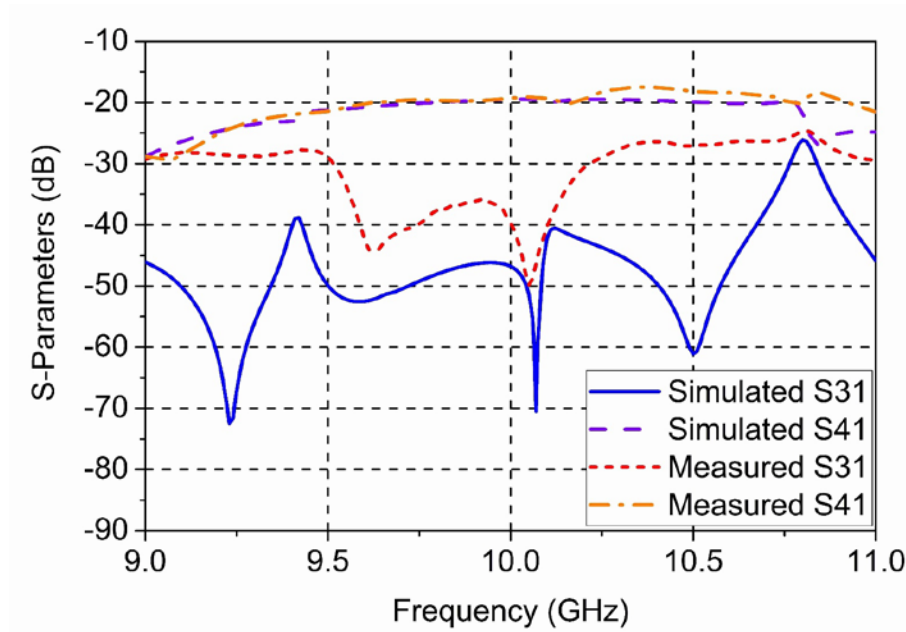


Figure 4.9: Comparison of measured and simulated MCW backward directional coupler isolation (S31) and coupling (S41).

4.2 MCW Dual-Mode Filter

Modern RF and microwave communication systems require high performance band-pass filters with low cost, compact size and sharp selectivity. Dual-mode filter provides a promising solution, which utilizes two degenerate modes within a single resonator to achieve size reduction as well as selectivity improvement. Compared to the conventional band-pass filters, the dual-mode filter usually exhibits lower loss, and can achieve similar performances using fewer resonators. Besides the expected size reduction, finite transmission zeros can also be achieved in the passband vicinity to improve the out of band selectivity, which can be done through a proper arrangement of the signal path phase relationship of the two degenerate modes. Depending on the choice of degenerate modes, the dual-mode filters have been widely implemented using circular or rectangular waveguides [37] [38] [39] [40]. Although waveguide filters have excellent performance, they are expensive and bulky compared to planar filters, which makes them difficult to integrate with other planar circuits. To resolve this integration issue, dual-mode filters implemented by SIW techniques were also investigated such as in [41] [42] [43].

The MCW has a duo wave-guiding structure, including inner rectangular waveguide and outer rectangular coaxial line, and is a promising candidate for dual-mode filter design for the following reasons. On one hand, the first two higher order modes in the outer waveguide are intrinsically two degenerate modes, which can be directly used to construct dual-mode resonator in filter design. On the other hand, the inner waveguide is completely enclosed by the outer waveguide in all four directions symmetrically, which largely facilitates the coupling structure design when the inner waveguide is used as the input/output feeding.

In this section, two types of MCW based dual-mode filters are designed at 10 GHz with fractional bandwidth of 2%. Both types of filters are different only in the design parameters of the input and output feeding. By properly adjusting these parameters, type I filter has one finite transmission zero at the left vicinity of the passband, while type II has one at the right.

4.2.1 Dual-Mode Filter Design

The fundamental modes of the inner and outer waveguides of MCW are TE_{10} and TEM mode, where their cross-sectional E -field distributions are shown in (a) and (b) of Figure 4.10, respectively. In this case, the width of MCW is much larger than its height, the first two higher order modes of the outer waveguide are folded TE_{20} I mode and folded TE_{20} II mode as shown in (c) and (d) of Figure 4.10, where the two modes are orthogonal to each other.

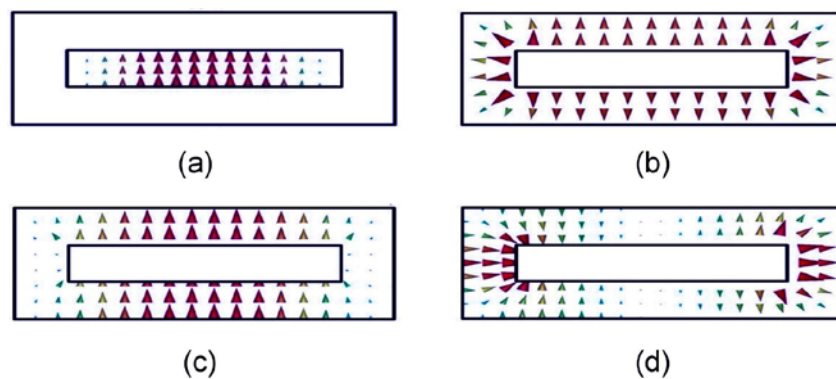


Figure 4.10: Fundamental modes of the inner (a) and outer (b) waveguides, and the first two higher order modes of the outer waveguide (c) and (d).

The dual-mode resonator is formed by terminating the outer waveguide by two electric walls at both ends with a distance of one wavelength. Though a half wavelength will be sufficient to form the resonator, one wavelength is used in this case to facilitate the design of input and outer feeding structures. The two degenerate modes in the resonator are folded TE₂₀₂ I mode and folded TE₂₀₂ II mode, following their waveguide mode notation. Simulated *E*-field distributions of the two degenerate modes are shown in Figure 4.11, and the simulated unloaded resonator quality factors for the folded TE₂₀₂ I mode and folded TE₂₀₂ II mode are Q_I=448 and Q_{II}=446, respectively.

The two modes' resonant frequencies can be calculated by

$$f_{202} = \frac{1}{\sqrt{\mu\epsilon}} \sqrt{\left(\frac{1}{W_{eq}}\right)^2 + \left(\frac{1}{L}\right)^2} \quad (3.7)$$

where L is the length of the resonator, and W_{eq} is the equivalent width of the rectangular waveguide which has the same cutoff frequency as the outer waveguide's higher order mode. Similar to rectangular waveguide, W_{eq} can be calculated by

$$W_{eq} = \frac{1}{f_c \sqrt{\mu\epsilon}} \quad (3.8)$$

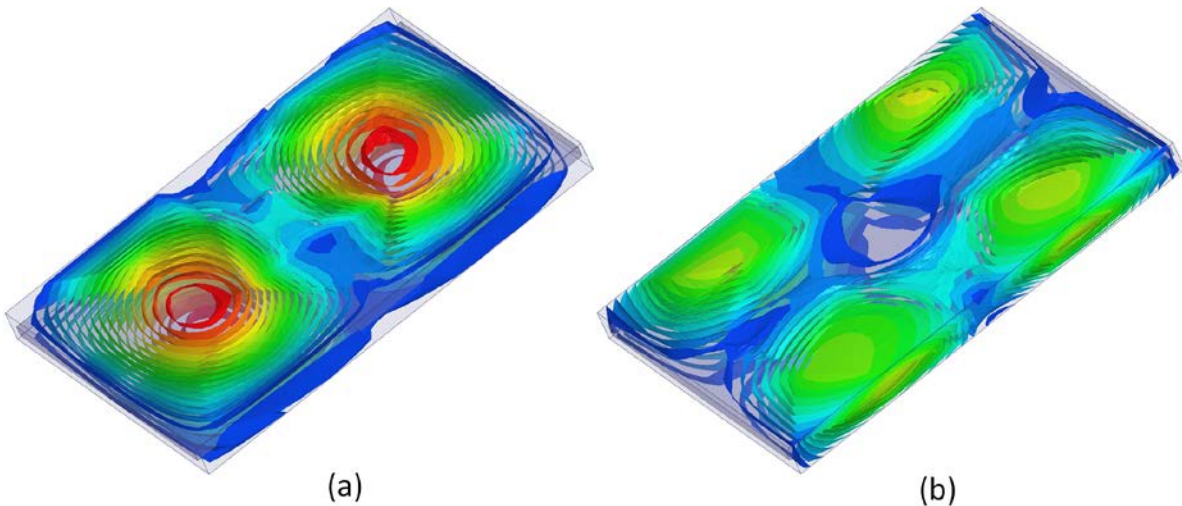


Figure 4.11: Simulated *E*-field distributions of the folded TE₂₀₂ I mode (a) and folded TE₂₀₂ II mode (b) in the dual-mode resonator.

where f_c is the higher order mode cutoff frequency of the outer waveguide. The cutoff frequencies of the two higher order modes of the outer waveguide can be calculated using transverse resonance method (TRM) as presented in chapter 2. Due to different reactive effects of the right-angle bends at the four corners, the cutoff frequencies of the two higher order modes of the outer waveguide are slightly different from each other. In the dual-mode filter design, this frequency split is used to control the filter bandwidth.

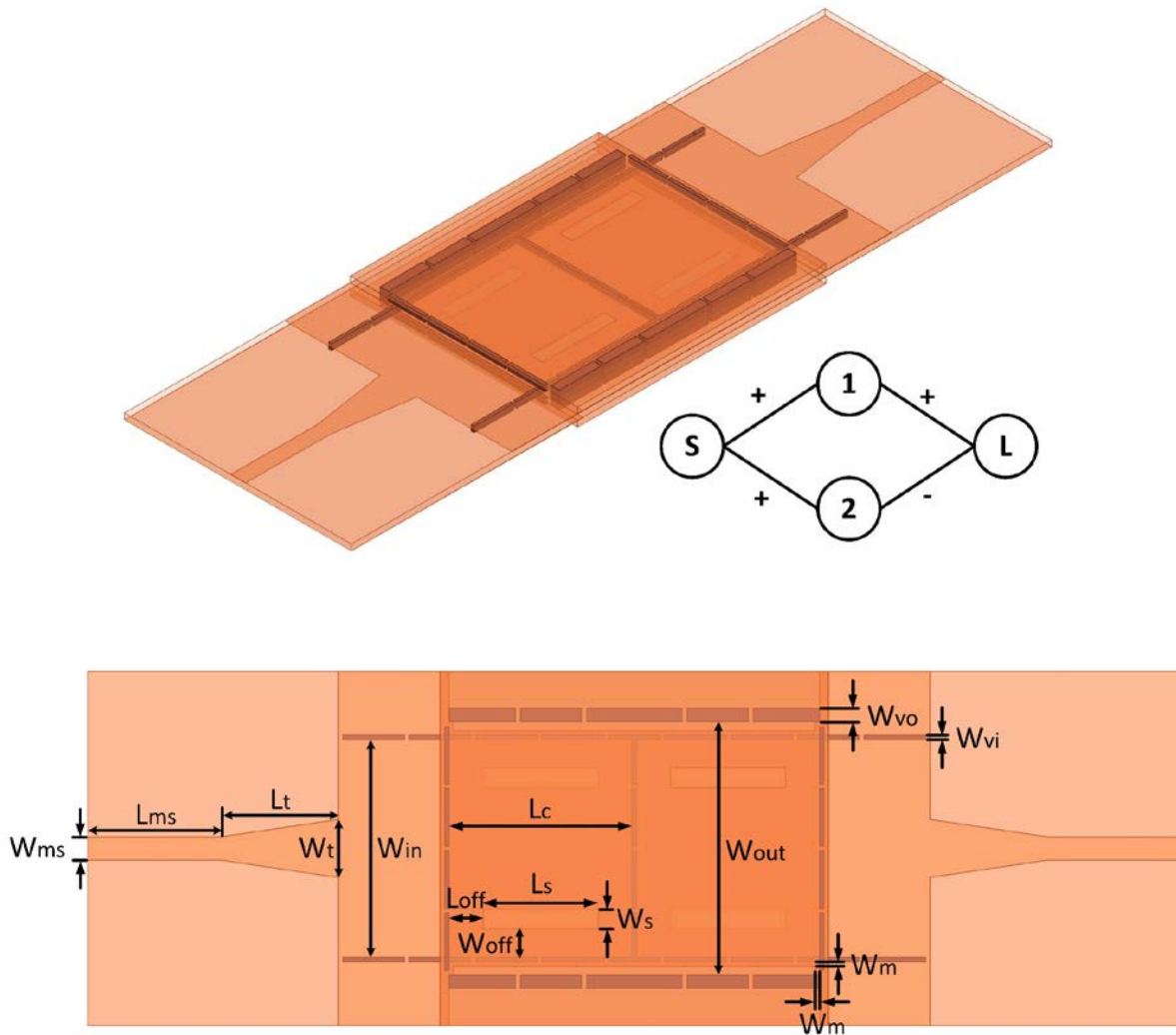


Figure 4.12: 3D view and dimensions of MCW based dual-mode filter and its corresponding resonator coupling scheme.

Two dual-mode filters are designed with type I filter having a finite transmission zero at the left side of the passband and type II filter at the right side. Both the dual-mode filters are constructed on three layers of 0.508 mm thick Rogers RT/Duroid 6002 substrates using multilayer substrate integration technique in our laboratory. The dual-mode filter geometry is described in Figure 4.12, where the design parameters of the two filters are listed in Table 4.2, respectively.

Table 4.2: Dimensions of type I and type II dual-mode filters.

Parameters	Type I Filter	Type II Filter	Parameters	Type I Filter	Type II Filter
W_{ms}	1.32 mm	1.32 mm	L_s	6.60 mm	7.92 mm
L_{ms}	7.62 mm	7.62 mm	W_s	1.12 mm	0.69 mm
L_t	6.73 mm	6.73 mm	L_{off}	1.94 mm	1.26 mm
W_t	3.30 mm	3.30 mm	W_{off}	1.63 mm	1.42 mm
W_{in}	12.5 mm	12.5 mm	W_{vi}	0.25 mm	0.25 mm
L_c	10.49 mm	10.44 mm	W_{vo}	0.76 mm	0.76 mm
W_{out}	14.5 mm	14.5 mm	W_m	0.25 mm	0.25 mm

The inner waveguide is used for both the input and output feedings, where the isolation between the input and output is achieved by inserting an electric wall at the middle layer. The input feeding is made through two rectangular slots at the top right and bottom left of the input inner waveguide, while the output feeding is made through two rectangular slots at the top left and bottom right of the output inner waveguide, respectively (shown in Figure 4.12). By arranging the input and output coupling slots in this alternative way, the desired phase difference between the two signal paths from source to load can be realized for finite transmission zero generation, where its corresponding coupling scheme is also shown in Figure 4.12. This 180-degree phase difference in the two degenerate mode signal paths causes the transmission path to vanish, thus creating a finite

transmission zero. This transmission zero can be placed at either the left or right side of the passband by adjusting the feeding parameters.

From Table 4.2, the two types of dual-mode filters are different only in the value of parameters W_s , L_s , W_{off} , L_{off} and L_c . The change of slots offsets (W_{off}) alters the excitation of each degenerate mode, thus changing its finite transmission zero location. The change of slots dimensions (W_s and L_s) alters the input and output coupling of filter to achieve good matching and minimize return loss. The change of resonator length (L_c) is needed to compensate the slight resonant frequency shift due to the change of input and output coupling parameters.

The parametric study of the effect of slot offset W_{off} on the transmission zero location is conducted for both the type I and type II filters. For the type I filter in Figure 4.13, its left transmission zero shifts toward the passband as W_{off} increases. In contrast for the type II filter in Figure 4.14, its right transmission zero shifts away from the passband as W_{off} increases. This shift property of the dual-mode filter is useful in achieving the desirable transmission zero location in the filter design.

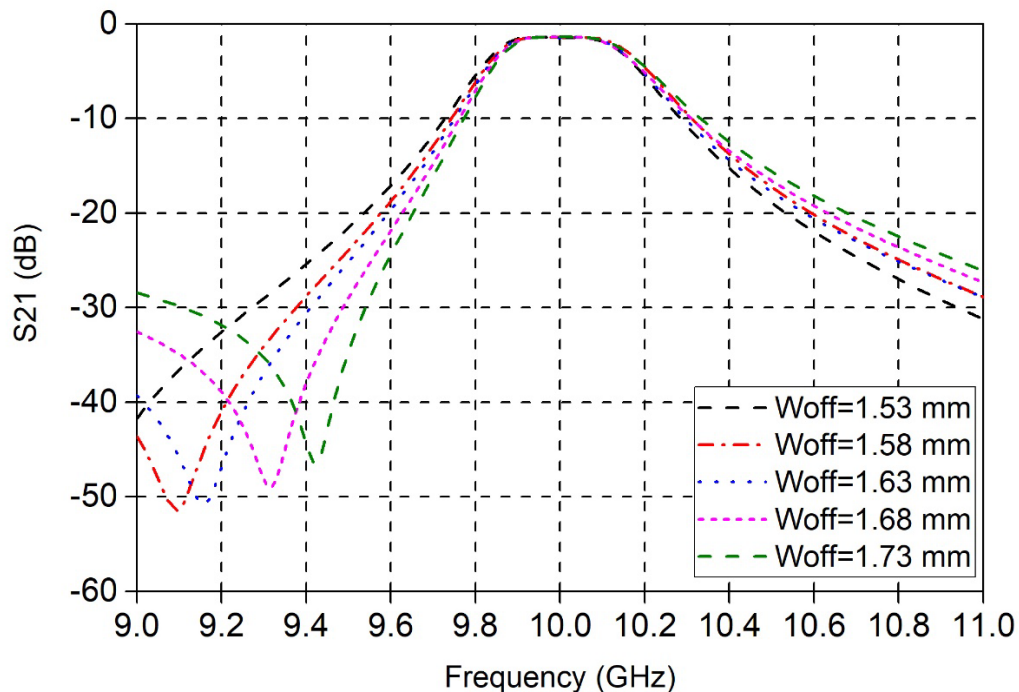


Figure 4.13: Simulated S21 of type I filter, exhibiting its left transmission zero location at different slot offset.

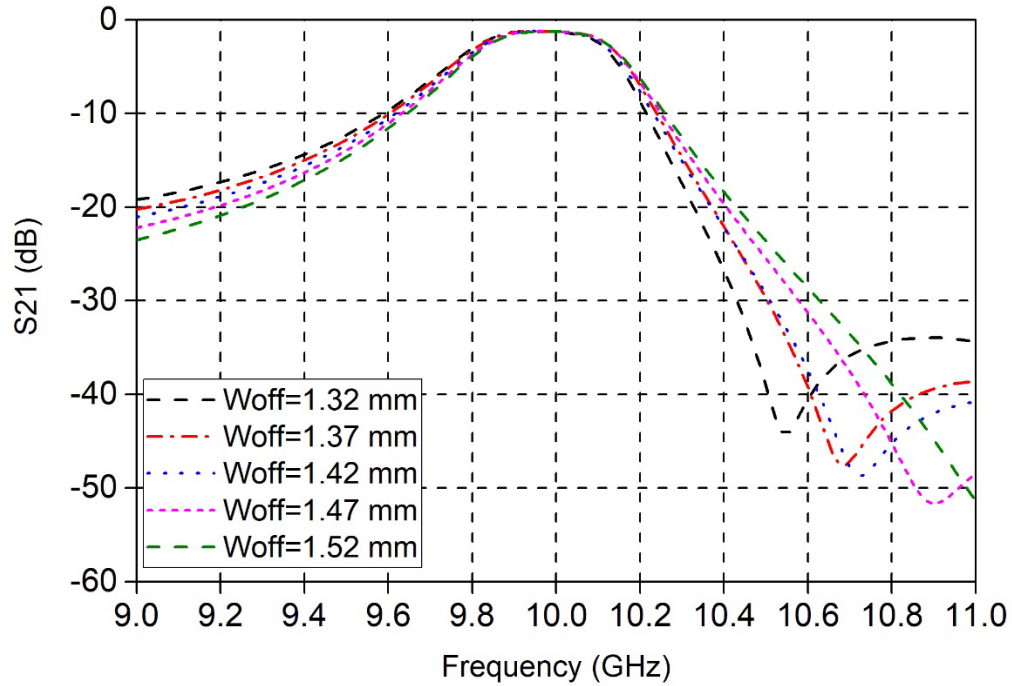


Figure 4.14: Simulated S21 of type II filter, exhibiting its right transmission zero location at different slot offset.

Simulated S-parameters of the two types of dual-mode filter are obtained and shown in Figure 4.15. Two transmission poles and one finite transmission zero are observed in both the filters. The two transmission poles are used to control the bandwidth of the passband, and the one finite transmission zero is used to improve its out of band selectivity. Thanks to the generated finite transmission zero, type I filter exhibits a steeper lower side frequency response, while type II filter exhibits a steeper upper side frequency response, respectively. Depending on the selectivity requirements, this filter response can be reconfigured by adjusting input/output feeding parameters in design.

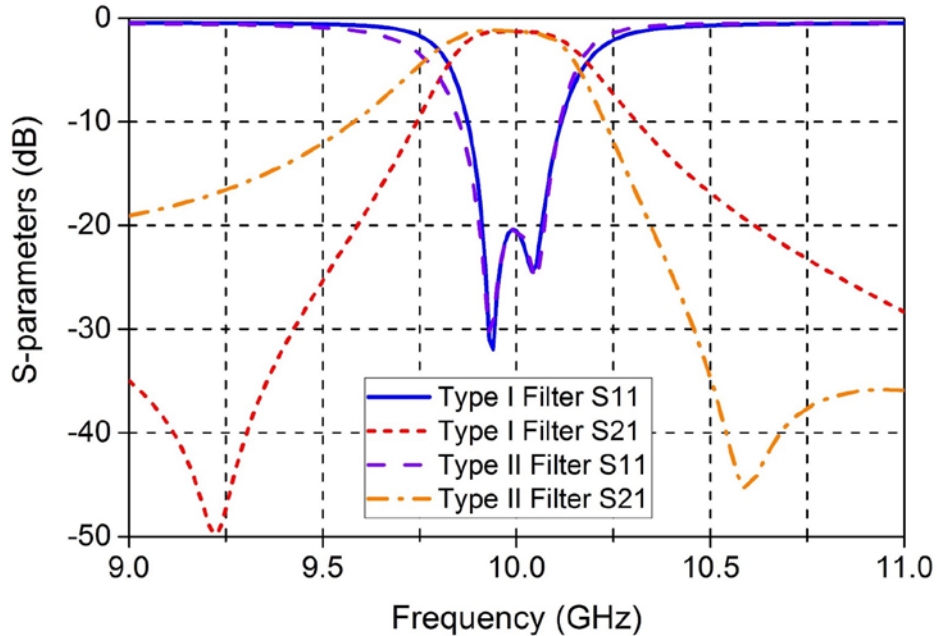


Figure 4.15: Simulated S-parameters of type I and type II dual-mode filters.

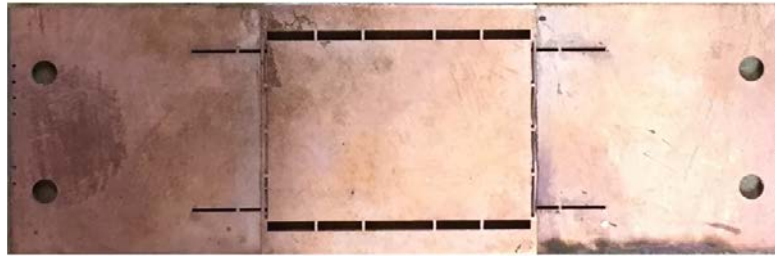
4.2.2 Fabrication and Measurement

The picture of the fabricated type I dual-mode filter with left finite transmission zero is shown in Figure 4.16, where the extra screw holes and edge vias are used for adaptor connection. The filter was measured using a two port VNA, where the TRL calibration is used to de-embed the connector effects.

Simulated and measured S-parameters of the type I dual-mode filter are displayed in Figure 4.17. The measured passband is from 9.88 GHz to 10.25 GHz with return loss better than -11 dB within the passband. One finite transmission zero on the left of passband at 9.36 GHz is identified as shown in Figure 4.17. The difference between the simulated and measured results is mainly caused by the tolerance issue in multilayer fabrication process. The dual-mode resonator is fabricated by gluing three layers of substrate under a high pressure with metalized vias on all four sides, where the losses introduced by glue and possibly air gap will decrease the resonator quality factor. This decrease in quality factor of resonator in turn increases the filter insertion loss as well as its passband bandwidth in the measurement results. However, the filter performance can be further improved using alternative fabrication techniques such as LTCC or 3D printing.



(a)



(b)

Figure 4.16: Pictures of the fabricated type I dual-mode filter: front side view (a) and back side view (b).

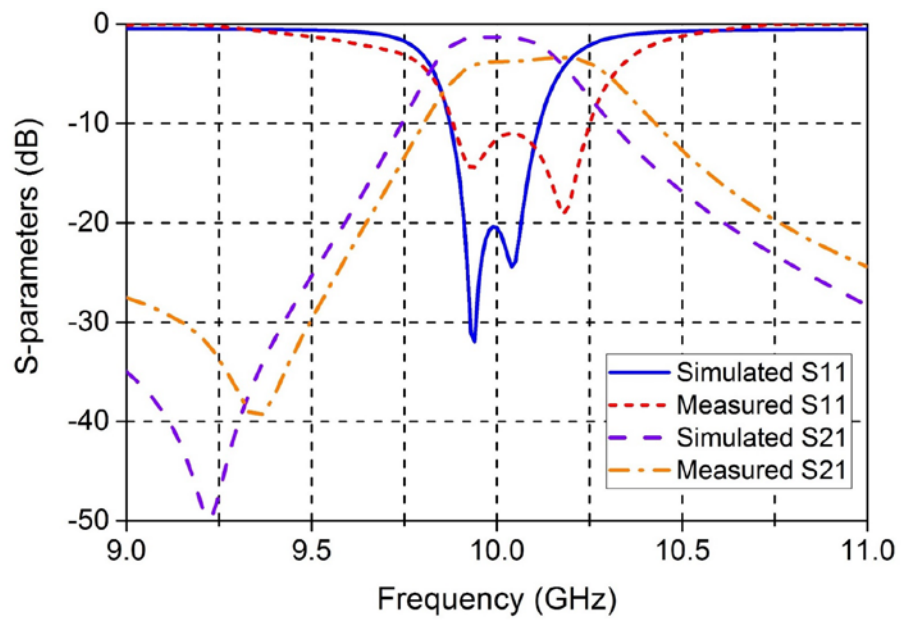


Figure 4.17: Simulated and measured S-parameters of fabricated type I dual-mode filter.

4.4 MCW Magic Tee

Magic tee is a microwave device widely used in power combiners and dividers, antenna feeding networks, balanced mixers and amplifiers, etc. [23]. Magic tee is composed of four ports, including one summation port, one difference port, and two output ports. When the signal goes into the summation port, two equally divided signals will come out from the two output ports completely in-phase. In contrast, when the signal goes into the difference port, two equally divided signals will come out from the two output ports with 180 phase difference. In a conventional waveguide magic tee design, the signal summation and difference is achieved using a 3D junction. Besides waveguide magic tee in 3D geometry, the planar magic tees are also proposed using microstrip-slotlines [44] [45] and SIWs [46] [47] [48]. In this section, a planar magic tee based on the MCW platform is proposed. In the magic tee design, the dual-mode nature of the inner and outer waveguides of MCW is explored to achieve the signal summation and difference.

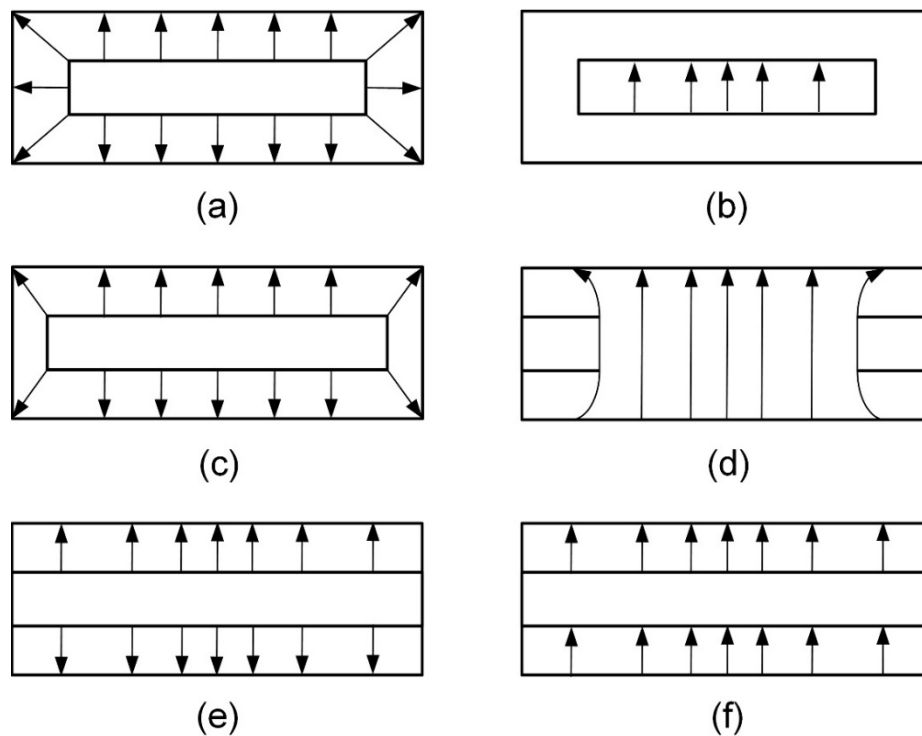


Figure 4.18: *E*-field transformation of outer ((a)->(c)->(e)) and inner ((b)->(d)->(f)) waveguides at magic tee junction.

4.4.1 Magic Tee Analysis and Design

For the MCW, the fundamental modes of the outer and inner waveguides are TEM and TE_{10} mode, where their E -field distributions at the cross-section are shown in (a) and (b) of Figure 4.18, respectively. In this work, the magic tee is also fabricated using three layers of substrates on the same platform as the MCW. For the outer waveguide TEM mode, the E -fields are mostly concentrated on the top and bottom layer with opposite orientation. In contrast, for the inner waveguide TE_{10} mode, all the E -field are oriented in the same direction.

By observing the mode difference of the outer and inner waveguides, this E -field orientation diversity can be used to achieve the signal summation and difference required in the magic tee design. If the signal in the inner waveguide can be coupled to the top and bottom layers through apertures on the middle layer, the excited signal at the top and bottom layers will also be of the same E -field orientation. The desired E -field transformation at the magic tee junction for signal summation and difference operation are shown in Figure 4.18, with (a)->(c)->(e) for outer waveguide and (b)->(d)->(f) for inner waveguide.

For the outer waveguide, as the inner conductor gradually increases the width until completely contacting the outer conductor, the outer waveguide coaxial mode is transformed into two TE_{10} modes at the top and bottom layers with opposite E -field orientation as shown in (a), (c), (e) of Figure 4.18. For the inner waveguide, the signal in the inner waveguide is first coupled to the top and bottom layers through two symmetrical coupling slots, and then transformed to two TE_{10} modes with the same E -field orientation as shown in (b), (d), (f) of Figure 4.18. The outer and inner waveguide mode transformations resemble the common-differential mode scenario in circuit, which are used to achieve the signal summation and difference of the magic tee operation.

The magic tee is constructed on three layers of 0.508 mm thick Rogers RT/Duroid 6002 substrates using multilayer fabrication process. To excite both the outer and inner waveguides of the MCW from microstrip lines, the type II joint feeding network is used for the magic tee design. And two identical taper transitions are used at the top and bottom layers to transform the two output ports into microstrip lines.

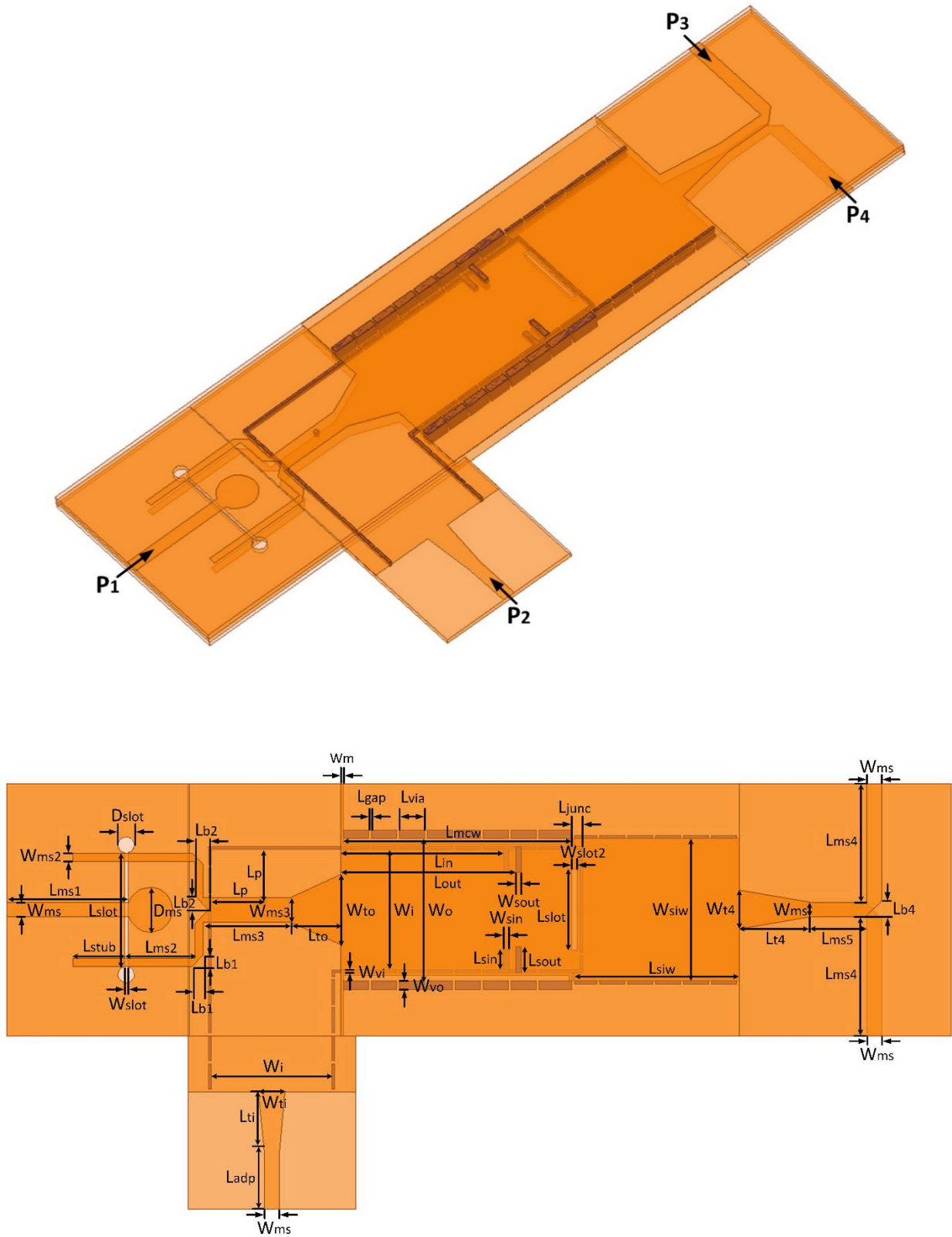


Figure 4.19: 3D view and dimensions of the MCW magic tee.

The dimensions of the magic tee together with the feeding networks are shown in Figure 4.19, where the design parameters are $W_{ms}=1.32$ mm, $L_{ms1}=11.06$ mm, $D_{ms}=4.06$ mm, $L_{slot}=10.29$ mm, $W_{slot}=0.3$ mm, $D_{slot}=1.47$ mm, $W_{ms2}=0.76$ mm, $L_{stub}=4.67$ mm, $L_{ms2}=6.38$ mm, $L_{b1}=1.02$ mm, $L_{b2}=1.27$ mm, $L_{ms3}=7.87$ mm, $W_{ms3}=2.21$ mm, $L_p=4.70$ mm, $L_{to}=4.57$ mm, $W_{to}=6.37$ mm, $W_o=12.95$ mm, $W_i=10.92$ mm, $W_{ti}=2.41$ mm, $L_{ti}=5.59$ mm, $L_{adp}=5.08$ mm, $L_{mcw}=20.7$ mm, $L_{in}=14.78$ mm, $L_{out}=15.93$ mm, $L_{sin}=1.83$ mm, $W_{sin}=0.51$ mm, $L_{sout}=2.34$ mm, $W_{sout}=0.51$ mm, $L_{slot2}=7.37$ mm, $W_{slot2}=0.51$ mm, $L_{junc}=1.02$ mm, $L_{siw}=14.99$ mm, $W_{siw}=12.95$ mm, $L_{t4}=6.48$ mm, $W_{t4}=3.56$ mm, $L_{ms4}=10.77$ mm, $L_{ms5}=5.08$ mm, $L_{b4}=1.47$ mm, $L_{gap}=0.25$ mm, $L_{via}=2.54$ mm.

At the center frequency of 10 GHz, the first two higher order modes of the outer waveguides may also be excited as analyzed before, and the higher order mode suppression is required. The simulated outer waveguide transition shows a higher order mode suppression performance of the folded TE₂₀ I mode by 30 dB and the folded TE₂₀ II mode by 54.4 dB at 10 GHz. This higher order mode suppression is achieved by creating different loading conditions for each mode at the outer waveguide transition. For the fundamental TEM mode, it sees a through line at the transition, and the signal can go directly to the microstrip line. While for the folded TE₂₀ I mode and folded TE₂₀ II mode, they see an open at the transition, and the signals are completely reflected.

Using two symmetrical coupling slots at the top and bottom conduct of the inner waveguide, the folded TE₂₀ I mode at the outer waveguide will be excited by the inner waveguide TE₁₀ mode, while the outer waveguide fundamental TEM will not be excited due to its opposite *E*-field orientation compared to the inner waveguide mode. This intrinsic mode isolation between the inner and outer waveguide modes is desirable for the summation and difference ports isolation of the magic tee.

For the signal coming into the difference port P_1 , the microstrip line mode signal is first transformed to the TEM mode in the outer waveguide through the microstrip-slotline transition. Then the signal is equally divided into the top and bottom SIW at the junction, with opposite *E*-field orientation. The coupling slots and the junction structure present certain reactance to the outer waveguide TEM mode. This reactance is matched by four symmetrical irises located at the four corners of the outer waveguide.

For the signal coming into the summation port P_2 , microstrip line mode signal is first transformed to the TE₁₀ mode in the inner waveguide through the taper transition. Then the signal is coupled

into the top and bottom layers through the two symmetrical slots on the middle layer. Due to the same E -field orientation, the folded TE_{20} I mode is excited at the outer waveguide. The microstrip-slotline transition on the left presents the open loading condition to the folded TE_{20} I mode, creating a total power reflection. Therefore, the coupled signal is then equally divided into the top and bottom SIW on the right at the junction, where the E -field orientation are the same. The coupling slots and the junction structure also present certain reactance to the inner waveguide TE_{10} mode. This reactance is matched by two symmetrical irises located at the inner waveguide.

The two output signals at the top and bottom SIW are further transformed to the microstrip lines through the taper transitions and right angle microstrip line bends at the top and bottom layers respectively.

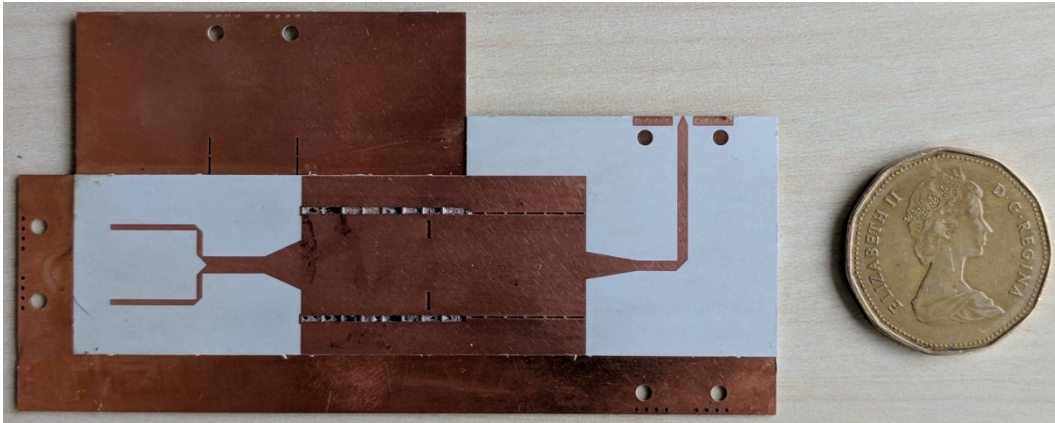
4.4.2 Fabrication and Measurement

The magic tee is measured using a VNA and four Southwest End Launch connectors, where TRL calibration is used to de-embed the connector effects. Pictures of the fabricated magic tee top and bottom views are shown in Figure 4.20, where extra length of microstrip lines and screw holes are fabricated to adopt the connectors.

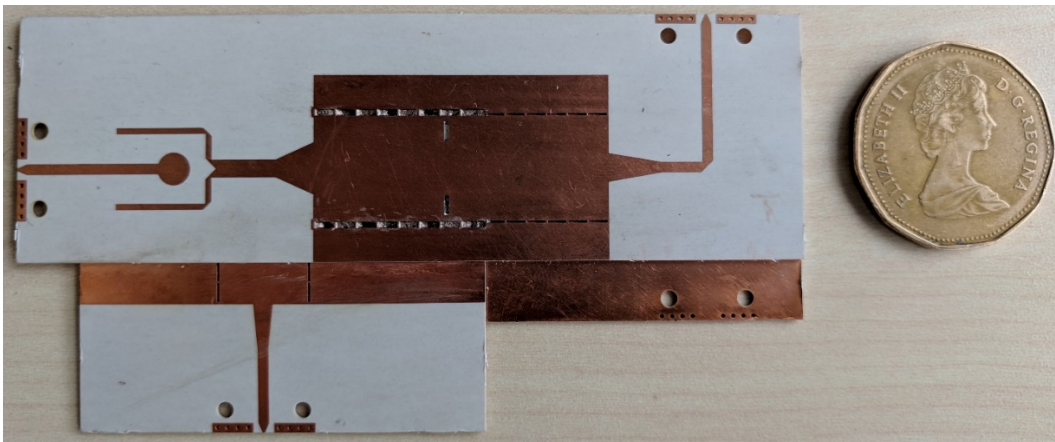
When the difference port P_1 is excited, the simulated and measured S-parameters from 9.5 GHz to 10.5 GHz are shown in Figure 4.21. In measurement, the matching of port P_1 is -21.7 dB, the isolation between port P_1 and port P_2 is -27.2 dB, and signals at the two output ports P_3 and P_4 are -4.7 dB and -4.4 dB respectively with a phase difference of 177 degree.

When the summation port P_2 is excited, the simulated and measured S-parameters from 9.5 GHz to 10.5 GHz are shown in Figure 4.22. In measurement, the matching of port P_2 is -25.4 dB, the isolation between port P_1 and port P_2 is -27.4 dB, and signals at the two output ports P_3 and P_4 are -5.6 dB and -5.4 dB respectively with a phase difference of 2 degree.

Good agreement between the measurement and simulation results is achieved, and the discrepancy is mainly caused by the fabrication tolerance of the multilayer processing. In the fabrication process, the three layers of substrates are glued together under high temperature and pressure, where these effects are considered ideal in the simulation.



(a)



(b)

Figure 4.20: Pictures of the front side (a) and back side (b) of the fabricated MCW magic tee.

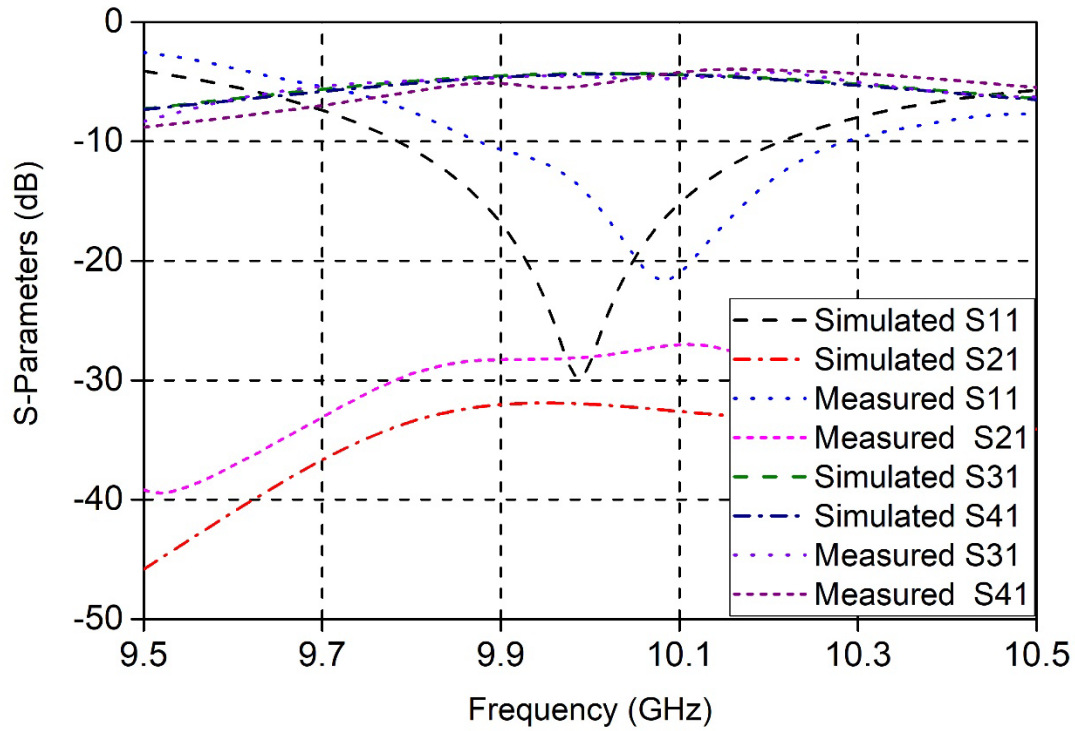


Figure 4.21: Simulated and measured S-parameters at the difference port P_1 of the magic tee.

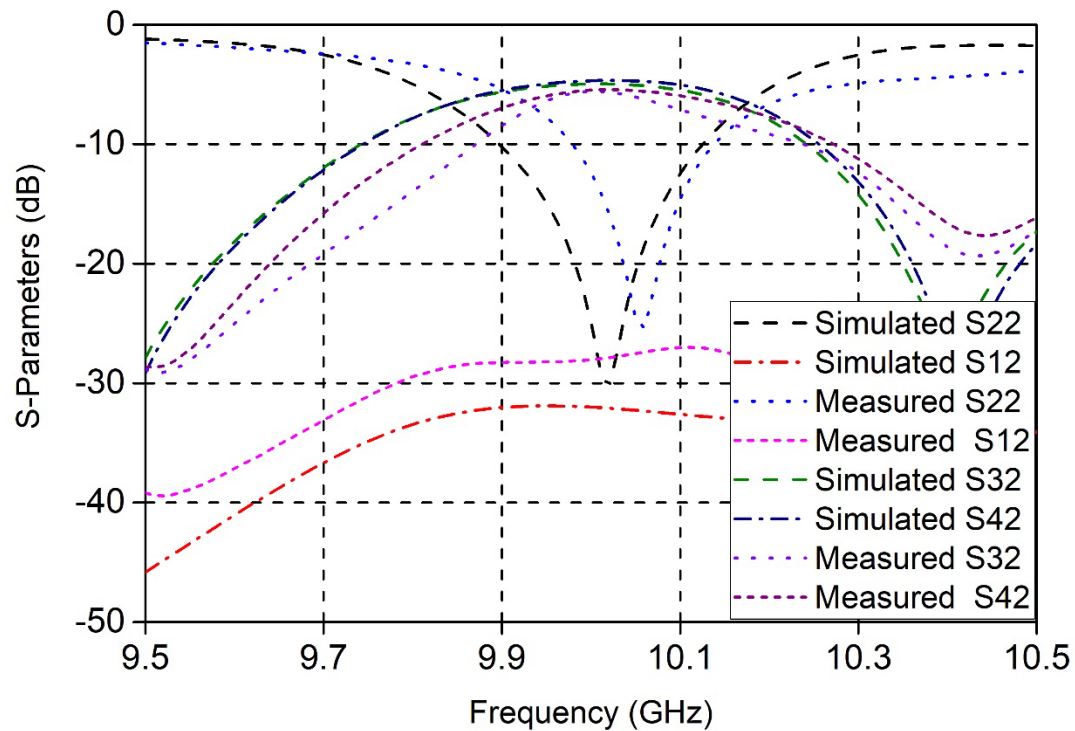


Figure 4.22: Simulated and measured S-parameters at the summation port P_2 of the magic tee.

4.5 Conclusion

In this chapter the unique propagation and mode properties of the inner and outer waveguides of MCW are explored. Applying these unique properties of MCW in different applications, various MCW based circuits such as directional coupler, dual-mode filter and magic tee are designed and experimented.

Firstly, a MCW directional coupler using the type II joint feeding network is proposed, taking advantage of the feeding network's higher-order modes suppressing nature. Due to the dual mode nature of the MCW, the mode conversion between the inner and outer waveguide during coupling is analyzed. The operation principle of coupler is mathematically formulated in achieving the required signal addition and cancelation, and a step-by-step design methodology is also presented. An MCW backward directional coupler at 10 GHz is fabricated to validate the proposed method. The desired coupling power of -20 dB and the maximum isolation of -50 dB are obtained in the coupler measurement.

Secondly, a MCW based dual-mode filter is proposed. This filter uses the inner waveguide of MCW as the input and output feedings, and the outer waveguide of MCW as the dual-mode resonator. The two degenerate modes in the outer waveguide resonator are used for the dual-mode filter operation, which generates two transmission poles and one finite transmission zero. The two transmission poles are used to control the filter bandwidth, and the finite transmission zero is used to improve the out of band selectivity. The generated finite transmission zero can be placed at either the left or right vicinity of the passband by adjusting the input and output feeding parameters. Two types of dual-mode filter are designed at 10 GHz with 2% fractional bandwidth. Type I filter exhibits a transmission zero at the left vicinity of the passband while type II filter exhibits one at the right. The type I dual-mode filter is fabricated and its measurement results agree with its simulations.

Finally, a MCW based planar magic tee is proposed. This magic tee uses the inner waveguide of MCW as the summation port, and the outer waveguide of MCW as the difference port in the operation. The different E -field orientation of the TE_{10} mode in the inner waveguide and TEM mode in the outer waveguide are used to achieve the signal summation and difference operation of the magic tee. The outer waveguide signal is equally divided and directly goes into the two output ports at the top and bottom layers out of phase, while the inner waveguide signal is coupled to the

two output ports at the top and bottom layers in phase through two slots on the middle layer. The reactance seen by the TE_{10} and TEM mode signals at the junction are matched with different irises in the inner and outer waveguides respectively. The MCW magic tee at 10 GHz is fabricated and its measurement results agree with its simulations.

CHAPTER 5 HALF-MODE COMPOSITE WAVEGUIDE

Taking advantages of the geometrical and mode symmetry, various waveguides can be structurally cut in half for half-mode operation to reduce the size. For example, the half-mode substrate integrated waveguide (HMSIW) was proposed in [49], where the cutting plane is equivalent to a perfect magnetic wall. Another example is the image substrate integrated non-radiative dielectric guide (iSINRD) proposed in [50], where the cutting plane is approximately equivalent to a perfect electric wall.

By carefully studying the fundamental modes in the inner and outer waveguides of MCW, we can find that both the modes have their symmetrical plane (equivalent to a perfect magnetic wall) at the center of the structure. Therefore, the MCW can also be cut in half along the center line to further reduce the structure size without altering the signal propagation. In this chapter, the half-mode composite waveguide (HMCW) is proposed, where its waveguide characteristics and design rules are studied and discussed. In addition, a joint feeding network for the HMCW is also proposed to facilitate measurements as well as its integration with other planar circuit.

5.1 HMCW Theoretical Analysis

The HMCW structure consists of an inner half open metallic structure and an outer half open metallic enclosure. The cross section of the HMCW is illustrated in Figure 5.1, as compared to its full size MCW. As shown in the figure, the open side aperture is closely equivalent to a magnetic wall with regards to both the inner and outer waveguides. For both the waveguides, the mode field distribution remains unchanged compared to the left part of the MCW, with the exception of a small amount of fringing field extending around the structure opening. Due to a large width-to-height ratio of the HMCW structure, the fringing effects of both the inner and outer waveguides are generally small [51]. A detailed analysis of the fringing effects on the HMSIW can be found in [52], where an empirical equation is derived for the equivalent width calculation.

With half the size reduction, the HMCW also inherits the advantages of the MCW as an effective broadband/multiband hardware design platform in support of simultaneous low and high frequency operation. In the HMCW, the outer waveguide supports quasi-TEM mode suitable for low frequency operation, while the inner waveguide supports quasi-TE_{0.5,0} mode suitable for high frequency operation. Like the MCW, the HMCW can also be fabricated using a multilayer substrate

integration technique such as a standard triple layer PCB process. This fabrication process makes use of three layers of substrate, with the middle layer to construct the inner waveguide and all the three layers to build up the outer waveguide.

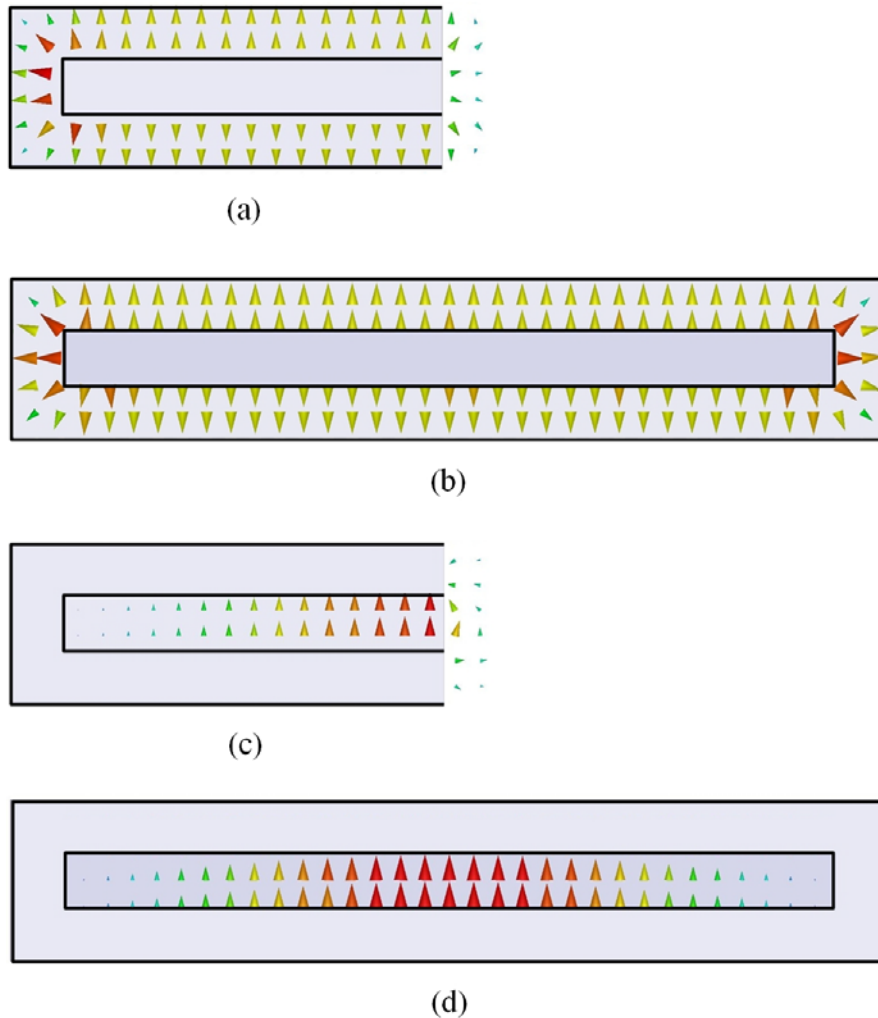


Figure 5.1: Cross section view and basic mode profile of HMCW and MCW structures with modes propagating in the inner and outer waveguides: (a) quasi-TEM mode, (b) TEM mode, (c) quasi- $TE_{0.5,0}$ mode, (d) TE_{10} mode.

The HMCW inner and outer waveguides are compared to other conventional transmission lines such as coaxial line, rectangular waveguide and microstrip line [23], where the comparison of performances in terms of loss, size, cost, etc., are listed in Table 5.1.

Table 5.1: Comparison of HMCW, waveguides and transmission lines.

	Coaxial Line	HMCW Outer Waveguide	Rectangular Waveguide	HMCW Inner Waveguide	Microstrip Line
Loss	Medium	Medium	Low	Low	Medium
Radiation	None	Low	None	Low	Medium
Size	Medium	Medium	Large	Medium	Small
Robustness	Medium	Medium	High	Medium	Low
Integration	Difficult	Medium	Difficult	Easy	Easy
Cost	Medium	Low	Medium	Low	Low

Compared to the coaxial line and rectangular waveguide, the HMCW has a better performance in terms of size, integration and cost. And compared to the microstrip line, the HMCW has a better performance in terms of loss, radiation and robustness. Furthermore, the HMCW also exhibits unique structural properties, as the inner waveguide is enclosed by the outer waveguide in all directions except for the opening. Using this property, the interaction between the inner and outer waveguides can be realized on the three sides through aperture coupling and/or on the opening through direct coupling. These extra degrees of freedom in design provide potential diversities in the future HMCW based circuit and antenna applications.

5.2 HMCW Parametric Study

The HMCW consists of the inner and the outer waveguides, along which the fundamental modes are quasi- $TE_{0.5,0}$ mode and quasi-TEM mode, respectively. As shown in Figure 5.1, although the inner and outer waveguides have openings on the same side, the two modes are intrinsically isolated from each other due to their field orientations, resembling a common-differential mode scenario in circuits. This isolation of the two fundamental modes allows the analysis of the inner and outer waveguides to be conducted independently.

The dimensions of an ideal HMCW in this parametric study, without considering the substrate integration process at this stage, are shown in Figure 5.2. To simplify the analysis, the side gap distance is selected to be the same between the inner and outer conductors as substrate thickness h , thus the total width and height of the HMCW are $w+h$ and $3h$, respectively. In our case, the HMCW width is much larger than the height, and the outer waveguide impedance is mainly determined by the capacitance between the top/bottom conductors and the inner conductor. Therefore, this simplification of side gap distance will not have a much effect on the outer waveguide impedance calculation.

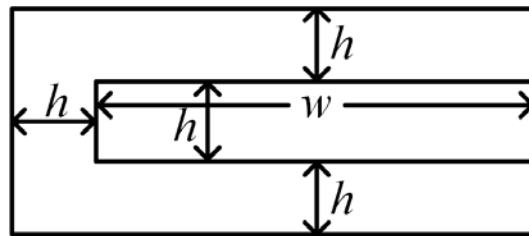


Figure 5.2: Dimensions of the HMCW inner and outer waveguides, where the distance between the inner and outer conductors is kept the same.

In our PCB processing, the choice of the height of HMCW is generally delimited by commercially available substrates, which are subject to certain discrete values provided by manufacturers. Of course, this is also dependent on processing techniques of interest. However, the selection of HMCW width is very flexible, and can be arbitrarily chosen by circuit designer. The width of HMCW determines both the cutoff frequency of the inner waveguide and the inner/outer waveguide impedances. In this work, the HMCW is constructed on three layers of 20 mils thick RT/duroid 6002 substrate ($\epsilon_r=2.94$), with a total height of $3h=1.524$ mm. In this case, both the inner and outer waveguide impedances at different w (width w is normalized by height h and central operating frequency of reference is at 25 GHz) are shown in Figure 5.5, and compared to its full size MCW counterpart (with width $w' = 2w$). In Figure 5.5, both the HMCW inner and outer waveguide impedances decrease as w increases, with the inner waveguide impedance decreasing at a faster rate compared to that of the outer waveguide.

The cutoff frequency of the HMCW inner waveguide is related to w , which can be determined in a similar way as the HMSIW as studied in [52]. The inner waveguide impedance increases

significantly when its operation frequency approaches to the cutoff frequency as the width decreases. Compared to the MCW, the HMCW has only half the size, and due to the size reduction, the impedances of the HMCW inner and outer waveguides are about twice higher (as described in Figure 5.5). In our case, this increase of the impedance actually facilitates the transition designs of both the HMCW inner and outer waveguides to a standard 50 Ω impedance system from the matching perspective.

In fact, the exact impedance value of both the HMCW inner and outer waveguides is slightly smaller than twice the value of its full-size counterpart, and this phenomenon is caused by the fringe field effects of both the HMCW inner and outer waveguides, which make their equivalent width slightly larger than the physical one. For the inner waveguide, its additional width Δw due to fringe effect normalized to the height h can be calculated using (5.1) as presented in [52].

$$\frac{\Delta w}{h} = \left(0.05 + \frac{0.30}{\varepsilon_r} \right) \cdot \ln \left(\frac{0.79w^2}{h^3} + \frac{104w - 261}{h^2} + \frac{38}{h} + 2.77 \right) \quad (4.1)$$

where ε_r is the relative permittivity of the dielectric filling, and w is the inner waveguide width.

For the outer waveguide, the quasi-TEM mode fringe effect can be analyzed using static electric field analysis similar to that of capacitor. The capacitor fringe effect are first calculated using Schwartz-Christoffel conformal mapping in [53], in which two different analytical models are provided after different approximation with different coefficient in the logarithmic term. However, the opening geometry of the outer waveguide is different from the capacitor, thus a new analytical model for the HMCW outer waveguide fringe effect is derived using the nonlinear least square method [54]. The analytical model derived in this work is shown in (5.2).

$$\frac{C_f}{C_0} = (0.96 + 0.042 / \varepsilon_r) \cdot \left(1 + \frac{1}{\pi R} + \frac{1}{\pi R} \ln(1.351R) \right) \quad (4.2)$$

where C_f is the outer waveguide per length capacitance including fringe effect, C_0 is the outer waveguide per length capacitance excluding fringe effect, ε_r is the relative permittivity of the dielectric filling, and R is the outer waveguide equivalent capacitor width to height ratio. Using the dimension parameters in Figure 5.2, the ratio R can be calculated as (5.3).

$$R = \frac{(2w + h) + (2w + 5h)}{2h} \quad (4.3)$$

where the equivalent capacitor width is the average value of the inner and outer conductor perimeters. The model consisting of two major terms, where the first term describes the relative permittivity relationship to the fringe effect, while the second term describes the geometry relationship to the fringe effect.

The fringe effect comparison of the calculated results using (5.2) and the simulated results using HFSS as the ratio R changes are shown in Figure 5.3, where $\epsilon_r = 3$ and $h = 0.508$ mm. When the width-height ratio increase, the more fields are confined into the waveguide, thus causing the percentage of the fringe capacitance to decrease as described in the second term of the model.

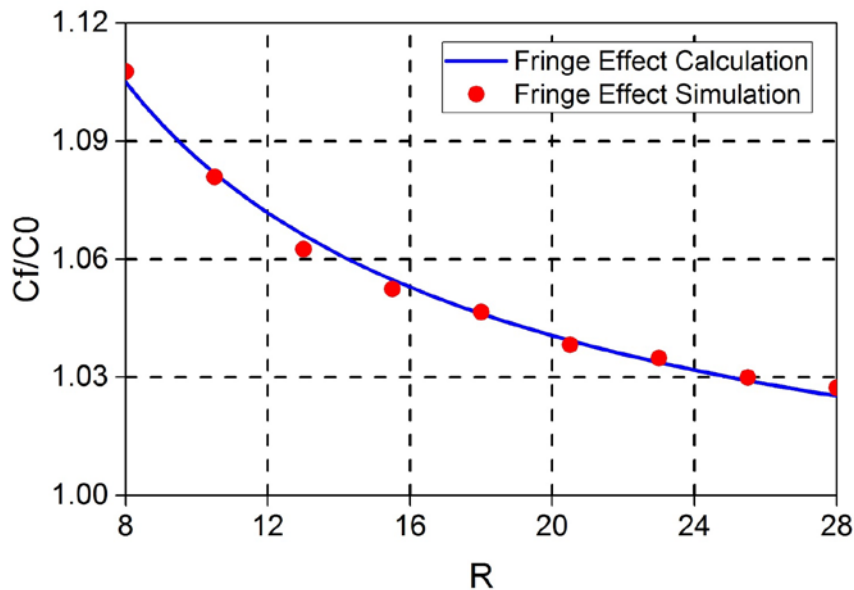


Figure 5.3: Comparison of calculated and simulated fringe effect of the outer waveguide at different width to height ratio.

The fringe effect comparison of the calculation and simulation as the relative permittivity ϵ_r changes are shown in Figure 5.4, where $w = 7.62$ mm and $h = 0.508$ mm. When the dielectric filling relative permittivity increases, more fields are confined in the waveguide, and less fields will

extend into the air. This phenomenon will decrease the fringe effect as the relative permittivity increases, and is described in the first term of the model.

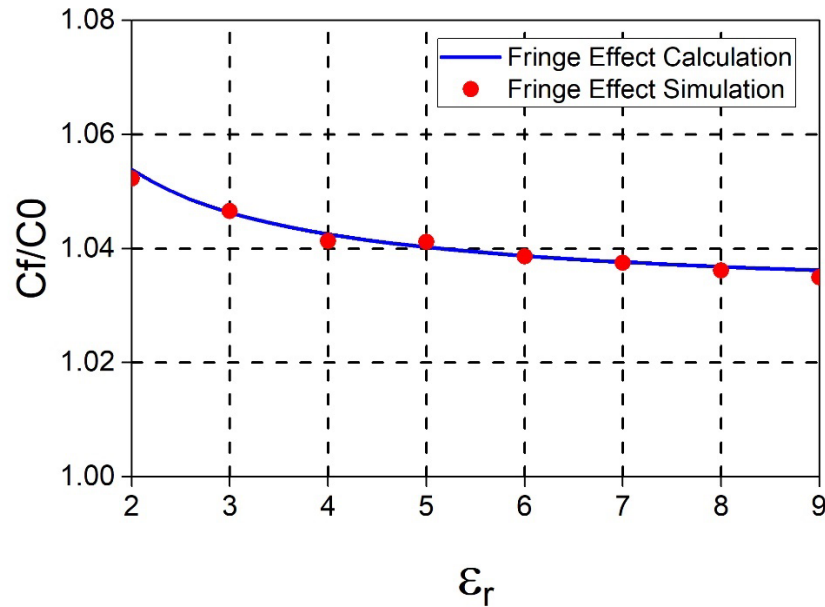


Figure 5.4: Comparison of calculated and simulated fringe effect of the outer waveguide at different relative permittivity.

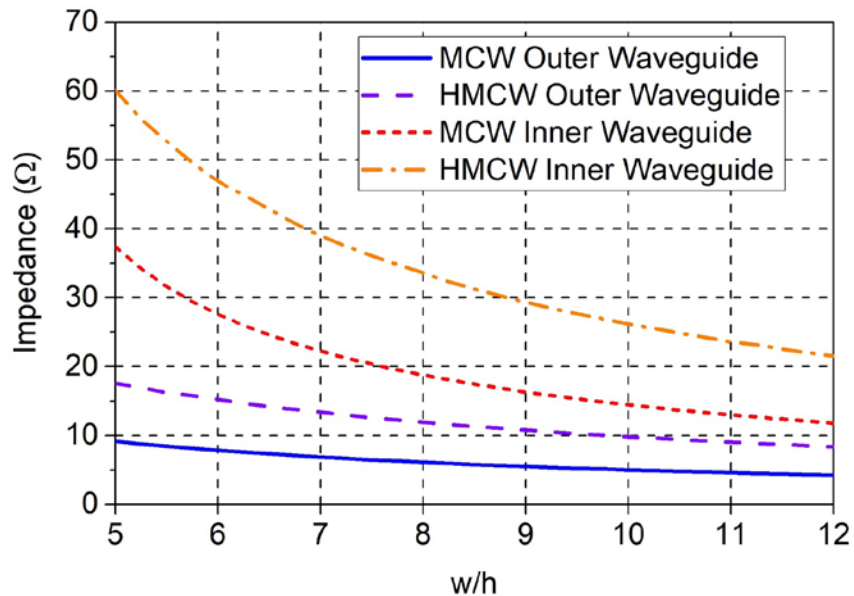


Figure 5.5: Comparison of simulated HMCW and MCW inner and outer waveguide impedances versus normalized width.

Based on the operation frequency for both inner and outer waveguides, the width of the inner waveguide is selected to be $w=3.64$ mm. The simulated total losses (including conductor, dielectric and radiation losses) of both the HMCW inner and outer waveguides versus operation frequency are shown in Figure 5.6, and also compared to those of the full size MCW. Both the HMCW outer and inner waveguide losses increase as frequency increases, and are generally comparable to that of the MCW. Due to the additional radiation loss introduced by the half open structure, the losses of both the HMCW inner and outer waveguides are slightly higher than that of the MCW, in which no radiation loss exists.

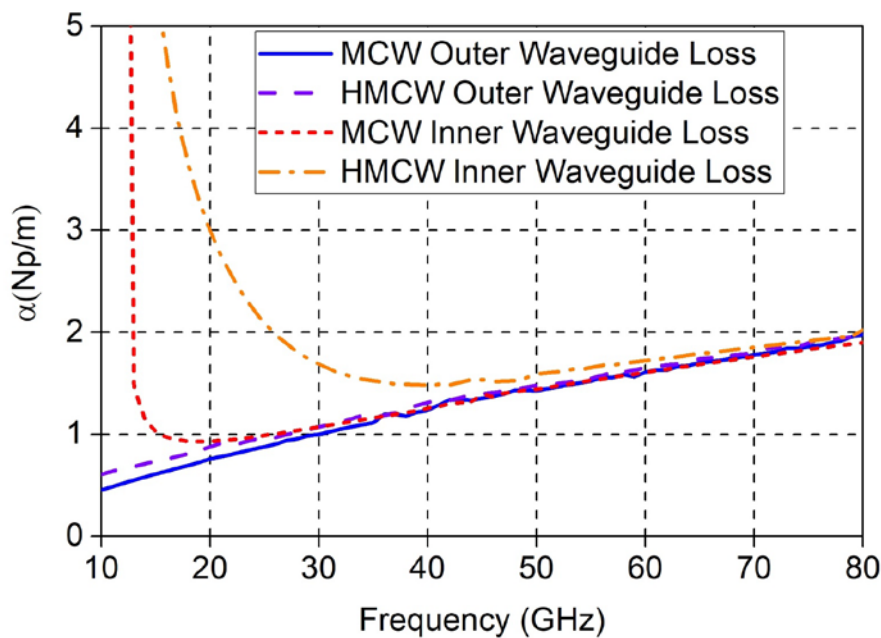


Figure 5.6: Comparison of simulated HMCW and MCW inner and outer waveguide losses as a function of frequency.

Over a lower frequency region, a significant loss increase of both the MCW and the HMCW inner waveguides can be observed. For the MCW, the loss increase is due to a large inherent attenuation of the cutoff effect as the signal approaches the cutoff frequency. However, the loss increase mechanism of the HMCW is different from the MCW. This loss increase is related to the fact that at low frequency region, the HMCW inner waveguide is operating in its leaky-wave region ($\beta_g < K_0$, where β_g and K_0 are the propagation constants in the waveguide and air respectively), and

most of power is leaked into the air rather than confined in the inner waveguide. This leaky phenomenon is similar to that of the HMSIW, where a detailed explanation can be found in [55].

Like the MCW, both the HMCW outer and inner waveguides may also support higher order modes. Using the same dimensions as in the HMCW loss analysis, the higher order modes in the HMCW outer and inner waveguides are shown in Figure 5.7 and Figure 5.8, respectively.

The HMCW outer waveguide's 1st higher order mode is the folded TE₁₀ mode, and its field distribution is shown in Figure 5.7. Compared to the MCW outer waveguide's (with twice the physical width and the same height) 1st and 2nd higher order modes (folded TE₂₀ I and II modes), the folded TE₁₀ mode has a slightly lower cutoff frequency. The cutoff frequency downshift is due to the fringing field effect at the outer waveguide opening, which slightly increases the equivalent width of the HMCW outer waveguide.

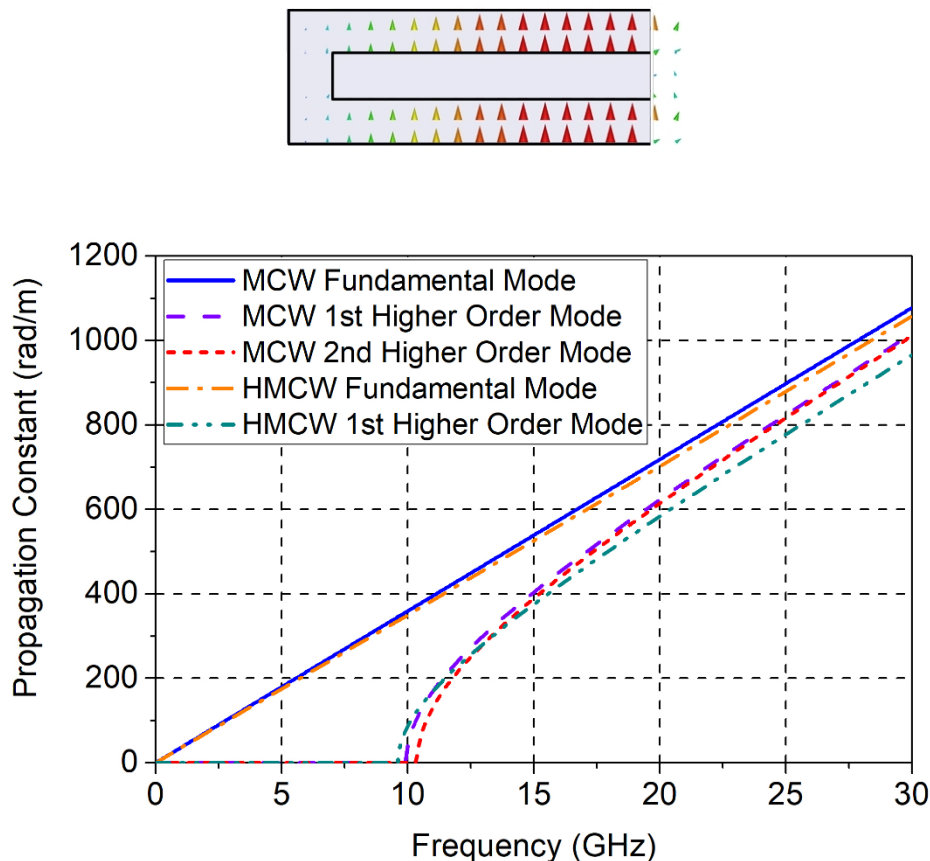


Figure 5.7: Field distribution of the 1st higher order mode of the HMCW outer waveguide and comparison of simulated outer waveguide dispersion diagram of the HMCW and the MCW.

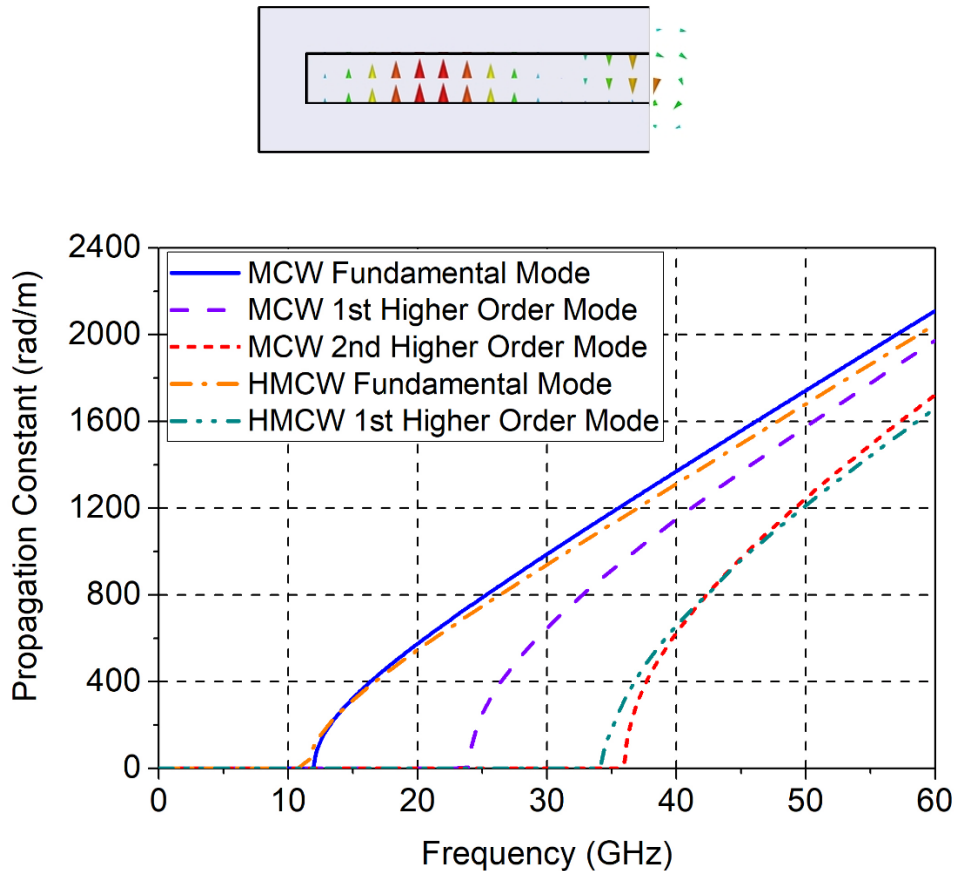


Figure 5.8: Field distribution of the 1st higher order mode of the HMCW inner waveguide and comparison of simulated inner waveguide dispersion diagram of the HMCW and the MCW.

Also, it is observed that the propagation constant of the folded TE_{10} mode is slightly lower than the folded TE_{20} I and II modes at the higher frequency region. This is because the HMCW outer waveguide is a half open structure, its effective permittivity is smaller than that in the MCW. The folded TE_{10} mode is the half-mode version of the folded TE_{20} I mode, and the folded TE_{20} II mode does not have its corresponding half-mode counterpart because of the boundary condition at the outer waveguide opening.

The HMCW inner waveguide's 1st higher order mode is the $TE_{1.5-0}$ mode, and its field distribution is shown in Figure 5.8. Compared to the MCW outer waveguide's 2nd higher order mode or the TE_{30} mode (the MCW 1st higher order mode is TE_{20} mode), the $TE_{1.5-0}$ mode also has a slightly lower cutoff frequency due to the fringing field effect of the inner waveguide opening.

The propagation constant of the $TE_{1.5-0}$ mode is also slightly lower than the TE_{30} mode at the higher frequency region, due to its half open dispersive nature. The TE_{20} mode does not have its corresponding half-mode counterpart because of the boundary condition at the inner waveguide opening.

5.3 Joint Feeding Network Design

Based on the previous analysis of the operation frequency, waveguide impedance, and transmission loss, the final dimensions of the fabricated HMCW are shown in Figure 5.9. To measure the HMCW using the conventional fixture and demonstrate its capability to integrate with other planar circuits, a joint feeding network is also proposed and demonstrated in this work, where both the HMCW inner and outer waveguides can be excited from microstrip lines in a simultaneous manner. In Figure 5.9, only the dimensions of the left part of the circuit is presented due to its horizontal symmetry.

To excite the HMCW outer waveguide from the microstrip line feeding, the signal is first equally divided into the top and bottom layers with 180 phase difference through a multilayer power divider proposed in chapter 3. Then, the two divided signals are fed into the outer waveguide through a two-stage dual taper structure from both the top and bottom layers simultaneously. The two-stage dual taper structure is identical on the top and bottom layers, and is used to achieve both the impedance and mode matching. The first stage of the dual taper structure is used for the impedance matching, where the microstrip line taper parameters L_{to} and W_{to} are used to gradually lower the microstrip line impedance to match with the outer waveguide impedance. Meanwhile, the second stage of the dual taper structure is used for the mode matching, where the outer waveguide taper parameters L_{tm} and W_{tm} are used to gradually conform the top and bottom layer microstrip line mode into the triple layer outer waveguide mode. This impedance and mode matching scheme can be verified by observing the field transformation at each cross section of the two-stage dual taper structure as shown in Figure 5.10.

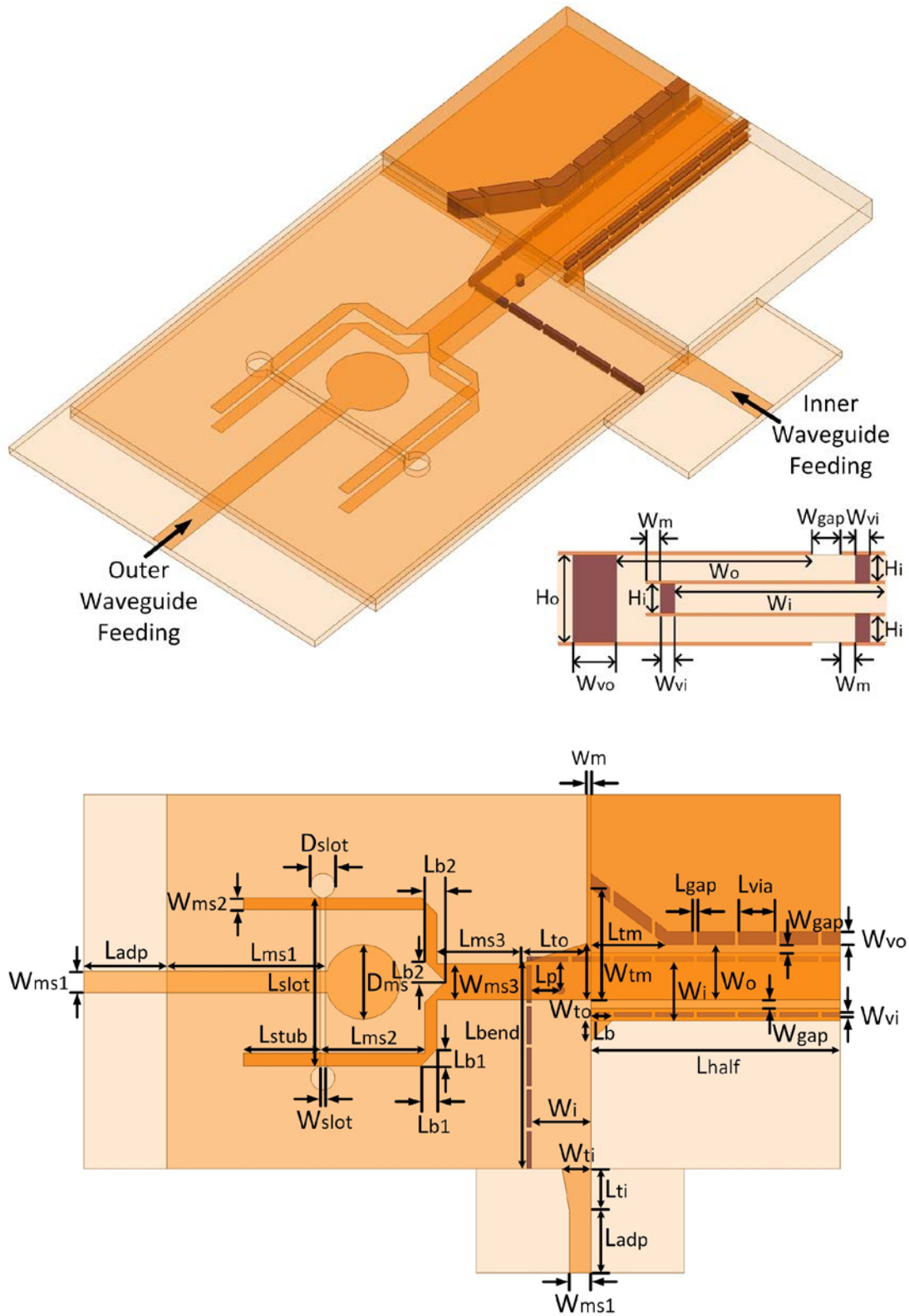


Figure 5.9 : 3D, cross-sectional and top views of the HMCW joint feeding network.

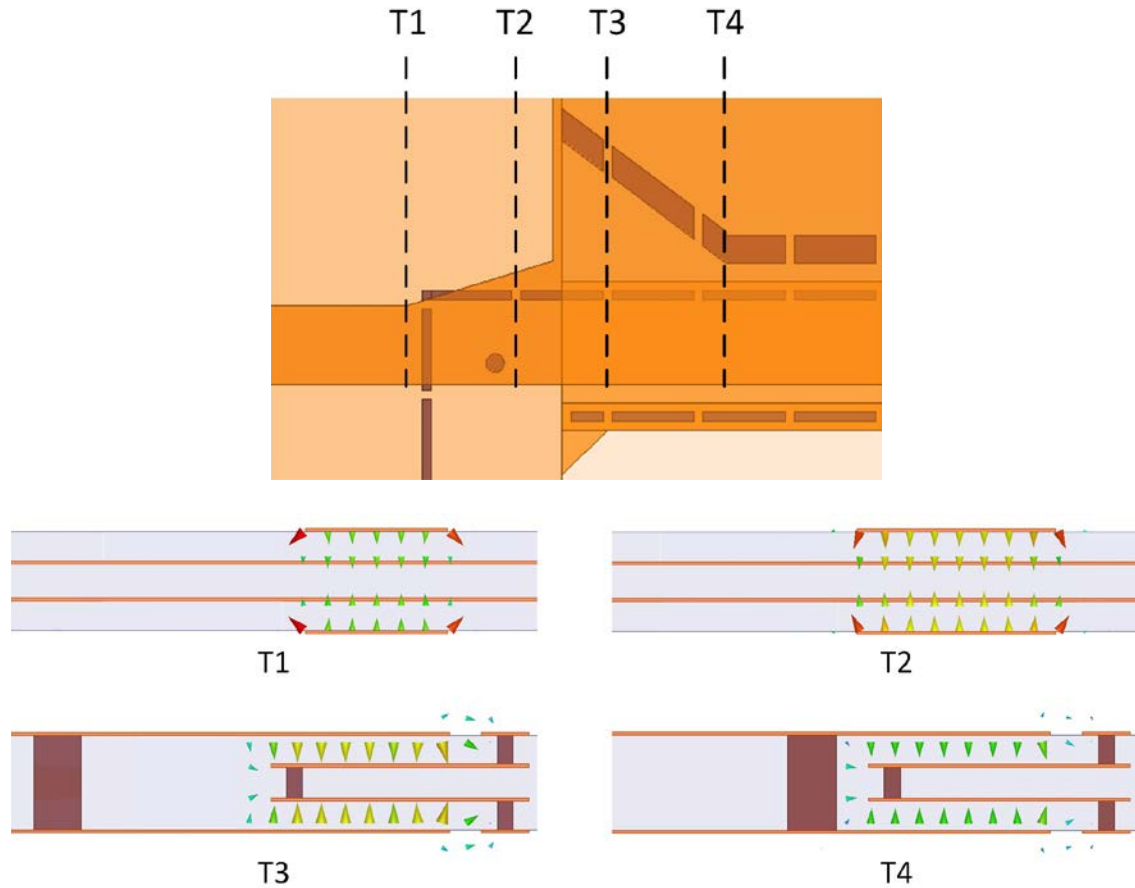


Figure 5.10: Mode transformation of a two-stage dual taper structure of the HMCW outer waveguide feeding network with E field distribution at each denoted position.

To excite the HMCW inner waveguide from the microstrip line feeding, the signal is first matched to the inner waveguide through a taper structure. Then a right angle inner waveguide bend is designed to allow the side entry of the feeding network. Good matching performance of the HMSIW bend is more difficult to achieve than the conventional SIW bend, due to its radiation loss at the bend discontinuity. In [56], 90 and 180-degree HMSIW bends were proposed, where large arcs with radius of several guided wavelengths are used to gradually turn the waveguide in achieving a good matching performance.

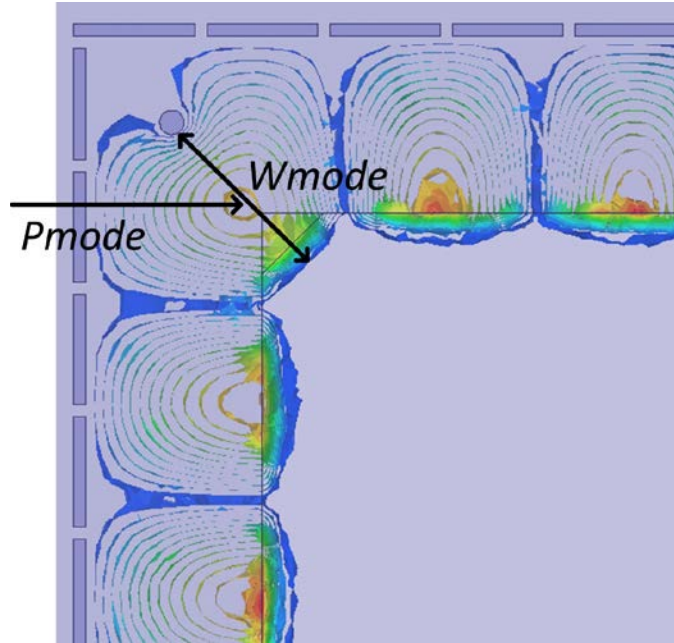


Figure 5.11: Mode transformation of a super compact right angle bend of the HMCW inner waveguide feeding network with E field distribution.

However, this large arc bend structure for the HMSIW requires a lot of space on the substrate, and is not suitable for the HMCW joint feeding network. To solve this issue, a super compact right angle inner waveguide bend is proposed in this work as shown in Figure 5.11, which consists of an inductive post and a triangle structure at the inner corner of both sides of the waveguide (dimensions are: $W_{ms1}=1.32$ mm, $L_{adp}=5.08$ mm, $L_{ms1}=9.68$ mm, $D_{ms}=4.57$ mm, $L_{slot}=10.29$ mm, $W_{slot}=0.3$ mm, $D_{slot}=1.47$ mm, $W_{ms2}=0.76$ mm, $L_{stub}=4.67$ mm, $L_{ms2}=6.38$ mm, $L_{b1}=1.02$ mm, $L_{b2}=1.27$ mm, $L_{ms3}=5.08$ mm, $W_{ms3}=2.21$ mm, $L_p=1.78$ mm, $L_{to}=4.06$ mm, $W_{to}=3.44$ mm, $L_{tm}=4.57$ mm, $W_{tm}=6.82$ mm, $L_b=1.27$ mm, $L_{half}=15.24$ mm, $L_{bend}=12.7$ mm, $W_o=3.39$ mm, $W_i=3.64$ mm, $W_{gap}=0.51$ mm, $L_{ti}=2.54$ mm, $W_{ti}=1.78$ mm, $W_m=0.25$ mm, $W_{vo}=0.76$ mm, $W_{vi}=0.25$ mm, $L_{gap}=0.25$ mm, $L_{via}=2.29$ mm, $H_o=1.52$ mm, $H_i=0.51$ mm). To achieve a good matching for the bend, both the impedance and the mode have to be matched simultaneously at the structure discontinuity. As shown in Figure 5.11, at the bend, the mode width parameter W_{mode} is used to control the impedance matching, while the mode's maximum E field position parameter P_{mode} is used to control the mode matching during turning. The two parameters W_{mode} and P_{mode} of the proposed bend structure provide two degrees of freedom in the design, thus the optimal bend performance with a

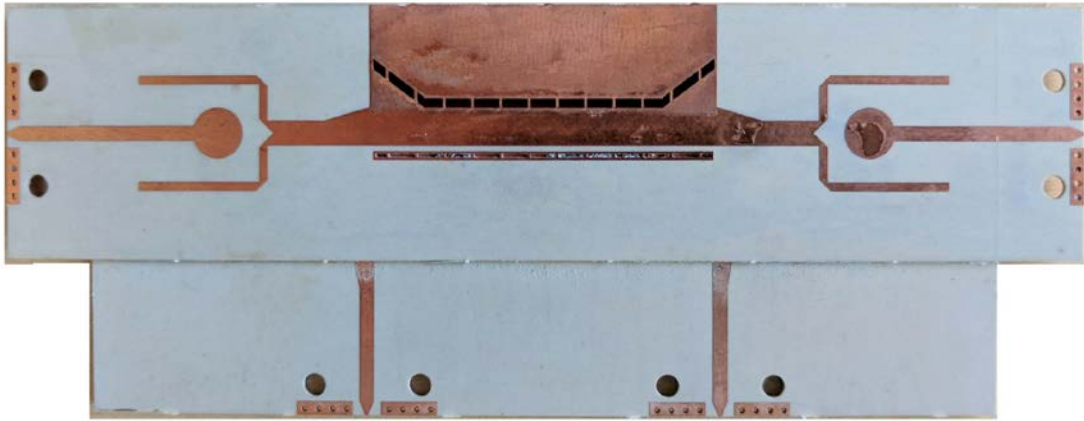
simultaneous impedance and mode matching is theoretically attainable. By optimizing the position of the inductive post and the dimensions of the triangle structure together, the realization of the optimal matching performance is guaranteed.

By combining the outer and inner waveguide feeding networks into a single integrated structure, the joint feeding network for the HMCW can be constructed as shown in Figure 5.9. In this joint feeding network, the outer waveguide feeding network is constructed using the top and bottom layers except for the dumbbell shaped slot of the multilayer power divider; while the inner waveguide feeding network is constructed using the middle layer. Under this arrangement, the two inner and outer feeding networks can be independently designed and optimized, as long as the dumbbell shaped slot is placed beyond the inner waveguide bend structure. In this excitation scheme, the inner and outer waveguide feeding networks are geometrically isolated from each other, which significantly facilitates the design process of each feeding network.

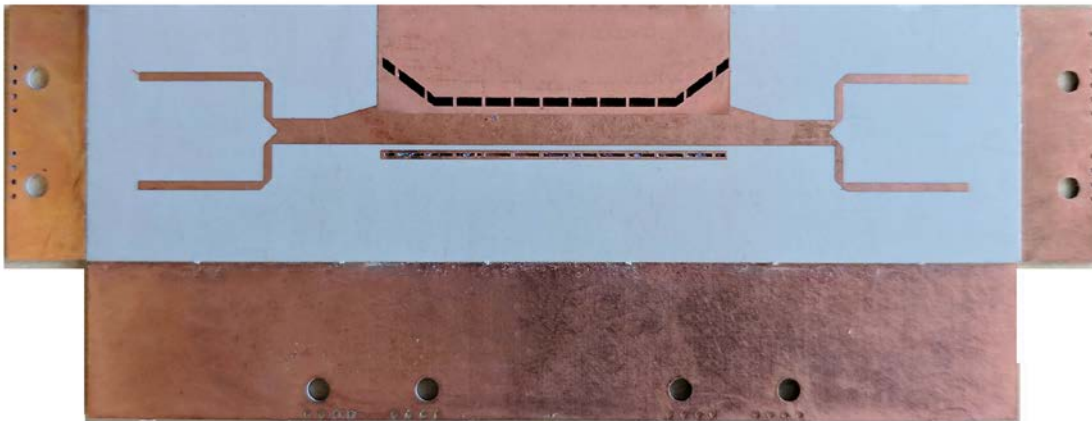
5.4 Fabrication and Measurement

As observed from the cross-sectional view in Figure 5.9, the HMCW is also constructed on three layers of substrate using multilayer substrate integration technique. The metal width on each metalized via is slightly extended by $W_m=0.25$ mm to fulfill the via metallization requirement in our lab. Both the inner and outer waveguide's metalized vias are arranged in a periodic fashion along the longitudinal direction with via length $L_{via}=2.29$ mm and via gap $L_{gap}=0.25$ mm. The smallest allowable via gap in our lab is chosen so to minimize the gap leakage loss. Though there is no coupling between the inner and outer waveguides fundamental modes, the undesired coupling between the $TE_{0.5-0}$ mode in the inner waveguide and the folded TE_{10} mode in the outer waveguide may exist under certain conditions. To further reduce this coupling, two extra rows of vias are fabricated on the top and bottom layers next to the outer waveguide opening, as shown in the cross-sectional view of Figure 5.9.

The fabricated HMCW joint feeding network is shown in Figure 5.12. In the measurements, a back-to-back setup is used for the HMCW joint feeding network, where extra screw holes are fabricated at each port for the end launch connection, and TRL calibration is used to de-embed the connector effects.



(a)



(b)

Figure 5.12: Pictures of fabricated HMCW joint feeding network front side (a) and back side (b).

When the outer waveguide is excited from port P_1 and port P_2 at 9 GHz, the corresponding E field distribution in the joint feeding network is plotted in Fig. 11, where the quasi-TEM mode signal is excited, thereby propagating in the outer waveguide alone. The simulated and measured S-parameters results are also shown in Fig. 11, where both the outer waveguide feeding network's reflection (S_{11}) and transmission (S_{21}) losses agree well with the simulation results. In the measurements, a good circuit matching is achieved for the HMCW outer waveguide feeding network from 4.4 GHz to 11.2 GHz ($S_{11} < -10$ dB) with a relative bandwidth of 87.2%. The measured insertion loss varies from 1.7 dB to 2.3 dB within the operation band, which includes both the feeding network and outer waveguide in a back-to-back setup.

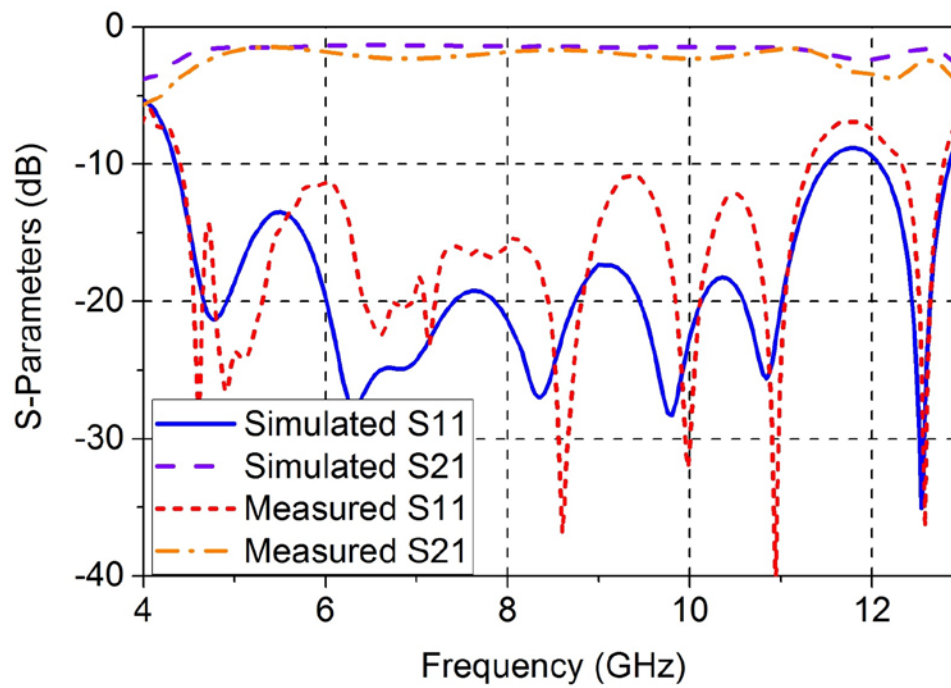
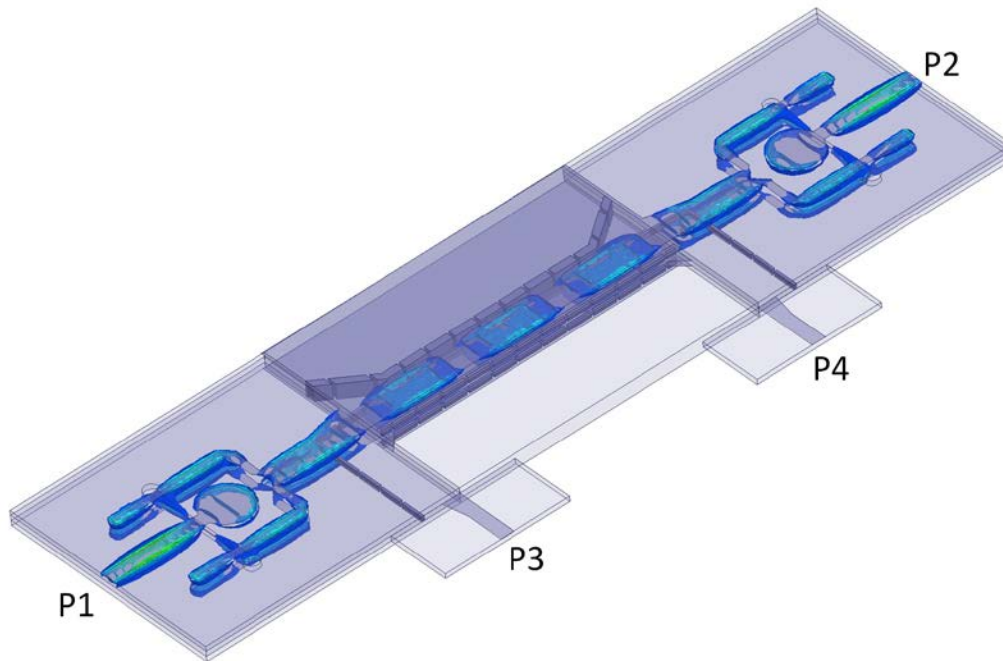


Figure 5.13: E field distribution in the outer waveguide at 9 GHz, and simulated and measured S-parameters of the back-to-back HMCW joint feeding network for low frequency operation.

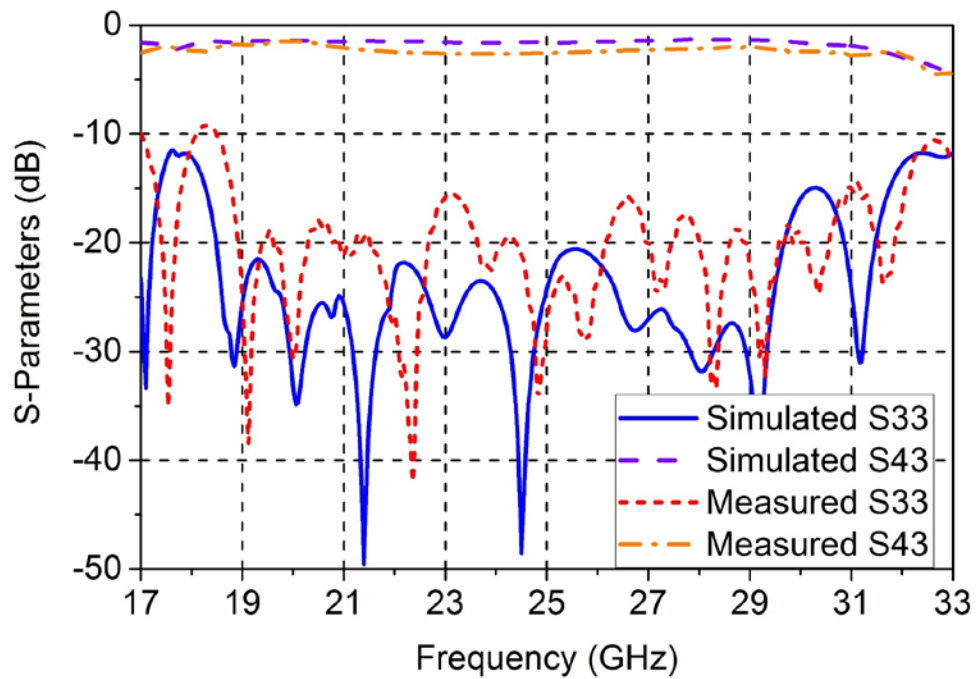
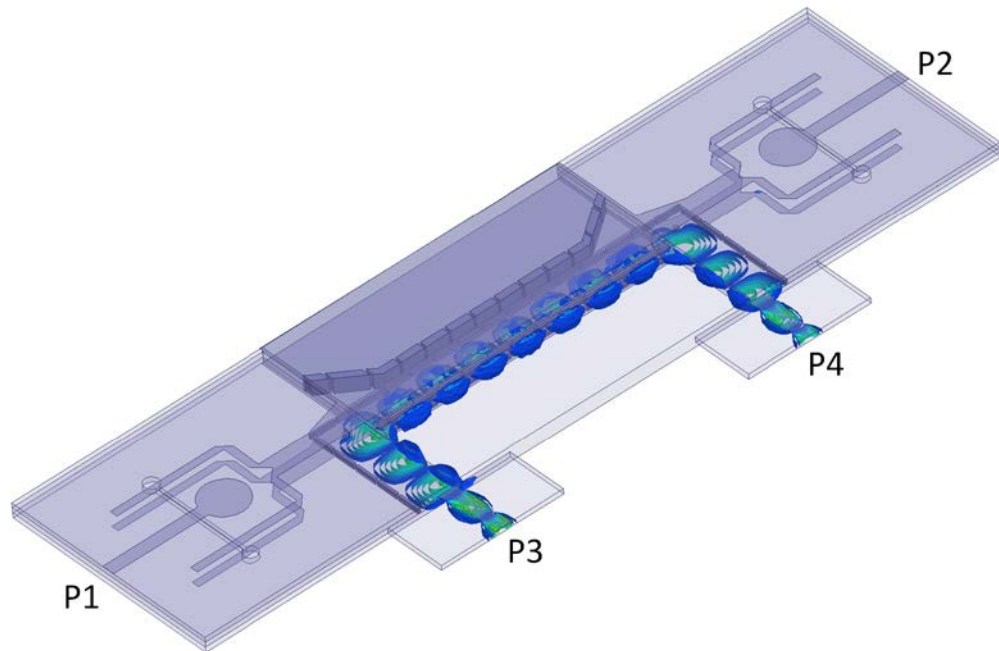


Figure 5.14: E field distribution in the inner waveguide at 25 GHz, and simulated and measured S-parameters of the back-to-back HMCW joint feeding network for high frequency operation.

Similarly, when the inner waveguide is excited from port P_3 and port P_4 at 25 GHz, the corresponding E field distribution in the joint feeding network is plotted in Figure 5.14, where the quasi- $TE_{0.5,0}$ mode signal is excited, which is then guided in the inner waveguide alone. The simulated and measured S-parameters results are also shown in Figure 5.14, where both the inner waveguide feeding network's reflection (S_{33}) and transmission (S_{43}) losses agree well with the simulation results. In the measurement, a good circuit matching is observed for the HMCW inner waveguide feeding network from 18.6 GHz to 32.6 GHz ($S_{11} < -10$ dB) with a relative bandwidth of 54.7%. The measured insertion loss varies from 1.5 dB to 2.6 dB within the operation band, which includes both the feeding network loss and inner waveguide transmission loss in the back-to-back setup. The difference between the measurement and simulation results is mainly caused by the fabrication tolerance during the multilayer circuit fabrication processing.

5.5 Conclusion

In this chapter, a guided-wave structure, the HMCW is proposed and presented. Similar to the full-size MCW, the HMCW also has an inner and outer waveguide, each working in its half-mode operation, respectively. In the HMCW structure, the signal propagates in the inner waveguide with quasi- $TE_{0.5,0}$ mode and along the outer waveguide with quasi-TEM mode. The HMCW's half-mode operation principle, impedance, loss and propagation characteristics including higher-order modes are analyzed. Compared to its full-size counterpart, the HMCW only occupies half the space, when operating within the same frequency band. Simulated results show that transmission loss of the HMCW is comparable to that of the full size MCW. Thus, it is also suitable for both low and high frequency design and applications.

To measure and integrate the HMCW with other planar circuits, a joint feeding network for the HMCW is also proposed. Its circuit prototype is fabricated on three layers of substrate using a multilayer substrate integration technique. This joint feeding network can simultaneously excite the inner and outer waveguide, respectively in an independent manner. In measurement, good matching is achieved for both the inner and outer waveguide feeding networks, and the measured results agree well with the simulated results.

CHAPTER 6 MULTILAYER CIRCUIT AND ANTENNA

In this chapter, double layer circuit and antenna inspired by the MCW are developed using the multilayer substrate integration technique in our lab. Compared to single layer SIW, double layer SIW circuit provides extra geometrical diversity in design, where the signal propagating or coupling in E plane can be exploited.

6.1 Variable Propagation Constant Directional Coupler

Directional couplers are passive circuits widely used in various RF and microwave applications. The well-popularized SIW can synthesize a three-dimensional bulky rectangular waveguide into an integrated planar form, and therefore it is widely used in the design of various types of directional couplers. Due to its similarity to rectangular waveguide, the SIW inherits most of the advantages of rectangular waveguide such as fully-shielded structure, low loss and high quality factor. Based on the SIW technology, various single-layer and multi-layer SIW directional coupler were studied [57].

In this section, a class of double-layer SIW two-hole directional couplers with variable propagation constants are proposed. Compared to the conventional directional coupler, the proposed counterparts make use of variable propagation constants of waveguide as the extra degree of freedom in the design. In this case, the propagation constants in each waveguide are not kept the same as the conventional ones, rather they are carefully chosen as a key parameter in achieving the desired signal addition and cancelation. The operation principle of the proposed coupler is mathematically formulated, and the coupler design methodology is also developed. Two directional couplers with variable propagation constants (VPC) are designed and fabricated. Both the forward and backward coupling operations are demonstrated using the proposed method through each of the couplers respectively.

6.1.1 Coupler Operation Principle

For a conventional two-hole double layer forward directional coupler, the top and bottom waveguides have the same propagation constants ($\beta_{top}=\beta_{bottom}$) and the two holes are spaced at a quarter electrical wavelength ($d=\lambda_g/4$) to achieve signal coupling between the two waveguides [23]. Since they have the same propagation constants, the forward signals are in phase and combine at

the coupled port. However, for the backward signals, because the signal through the second hole travels a half electrical wavelength ($2d=\lambda_g/2$) more than the signal through the first hole, they are 180° out of phase and thus cancel out each other at the isolated port.

The design equation for the forward directional coupler is shown in (6.1), where N is mostly chosen as 0 to have the shortest physical length:

$$\beta d = (2N + 1) \frac{\pi}{2} \quad (5.1)$$

When the propagation constants of the two waveguides are different, the forward directional coupler design equations are generalized by

$$\beta_{bottom} d + \beta_{top} d = (2N_1 + 1)\pi \quad (5.2)$$

$$\beta_{bottom} d - \beta_{top} d = 2N_2\pi \quad (5.3)$$

where $N_1=0, 1, 2, 3, \dots$, $N_2=0, 1, 2, 3, \dots$, and $N_1 \geq N_2$.

Equation (6.2) ensures that the backward signals are 180° out of phase and cancel out each other at isolated port. And equation (6.3) ensures that the forward signals are in phase and add up to each other at coupled port. The condition $N_1 \geq N_2$ is enforced to ensure a physically realizable solution with both propagation constants being positive. Theoretically, there exist infinite pairs of N_1 and N_2 that can satisfy equations (6.2) and (6.3).

By comparing coupler design equations (6.1), (6.2) and (6.3), the aforementioned conventional forward directional coupler is only a special case of the generalized forward directional coupler, where equation (6.1) can be directly acquired from equation (6.2) and (6.3) by setting $\beta_{bottom}=\beta_{top}$.

Using the similar principle, the backward directional coupler can also be realized using variable propagation constants (VPC). The backward directional coupler design equations are generalized as follows:

$$\beta_{bottom} d + \beta_{top} d = 2N_1\pi \quad (5.4)$$

$$\beta_{bottom} d - \beta_{top} d = (2N_2 + 1)\pi \quad (5.5)$$

where $N_1=1, 2, 3, \dots$, $N_2=0, 1, 2, 3, \dots$, and $N_1 > N_2$.

Similarly, equation (6.4) ensures that the backward signals are in phase and add up to each other at coupled port. And equation (6.5) ensures that the forward signals are 180° out of phase and cancel out each other at isolated port. The condition $N_1 > N_2$ is enforced to ensure a physically realizable solution with both propagation constants being positive.

6.1.2 Coupler Analysis and Design

To demonstrate the proposed methodology for VPC coupler design, both forward and backward directional couplers at 24 GHz are designed and prototyped. The couplers are constructed on two layers of 0.508 mm thick Rogers 6002 substrate ($\epsilon_r=2.94$) using multilayer SIW technique.

For the forward directional coupler, the propagation constants and hole spacing parameters are first calculated by equation (6.2) and (6.3). In our case, $N_1=3$ and $N_2=1$ are selected, and the width of the bottom and top waveguides can then be calculated, respectively [23]. In our design, two rotated narrow rectangular slots are used as the coupling slots (shown in Figure 6.1), and its rotation angle is optimized to achieve a -20 dB coupling. In the final layout, both the top and bottom waveguides are further transitioned into 50Ω microstrip line for measurement.

The selection of coupler index N_1 and N_2 is a trade-off between the coupler physical size and bandwidth performance. When N_1 and N_2 increase, the distance between the two holes increases, which in turn increases the coupler physical size as well. However, when N_1 and N_2 decrease, the cutoff frequency of the waveguides shifts closer to the operation frequency, which will decrease the coupler bandwidth performance. So following a trade-off analysis, $N_1=3$ and $N_2=1$ are selected for the forward directional coupler parameter calculation.

Following the same methodology, a backward directional coupler is also designed using equations (6.4) and (6.5) instead. The coupler index of $N_1=4$ and $N_2=0$ are selected to maintain the same hole distance as the forward directional coupler. All the rest design parameters are then calculated following the similar procedure as discussed before.

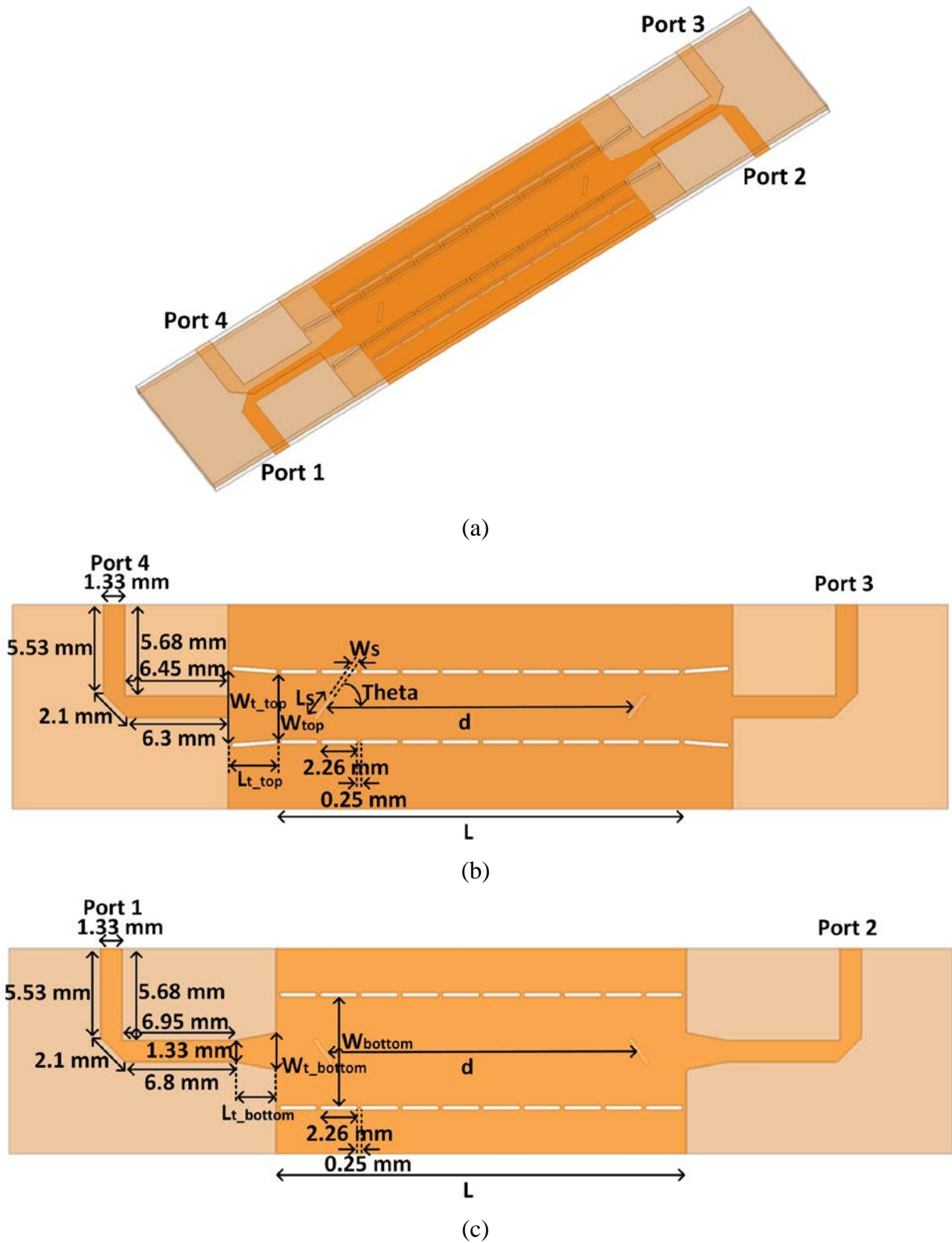


Figure 6.1: 3D view and dimensions of the proposed directional coupler (a) 3D view, (b) top view, (c) bottom view.

Table 6.1: Forward and backward directional coupler design parameters.

Coupler Type	Forward	Backward
Waveguide Parameters		
L	25.4 mm	25.4 mm
d	19.5 mm	19.5 mm
W_{top}	4.12 mm	4.81 mm
W_{bottom}	6.73 mm	6.73 mm
Slot Parameters		
L_s	1.83 mm	1.83 mm
W_s	0.25 mm	0.25 mm
θ	54°	46°
Top Transition Parameters		
W_{t_top}	4.57 mm	5.08 mm
L_{t_top}	3.05 mm	1.91 mm
Bottom Transition Parameters		
W_{t_bottom}	2.29 mm	2.29 mm
L_{t_bottom}	2.54 mm	2.54 mm

The final dimensions of the proposed directional couplers are shown in Figure 6.1 and the corresponding parameters for the forward and backward directional couplers are listed in Table 6.1, respectively. The coupler consists of two layers of substrates, and the two coupling slots are

etched on the common middle ground of both the waveguides. Because the coupler is symmetrical from left to right, only the dimensions of the left part are presented. Compared to the forward directional coupler, the backward directional coupler parameters are only different in W_{top} , θ , W_{t_top} and L_{t_top} . A different W_{top} gives the top waveguide a different propagation constant to satisfy different coupler design equations. A different θ is used to compensate a small coupling variation caused by the top waveguide width change to maintain the -20 dB coupling level. Different W_{t_top} and L_{t_top} are used in the transition to match the top waveguide after its width change.

6.1.3 Fabrication and Measurement

The fabricated forward and backward directional couplers are shown in Figure 6.2, where microstrip line right angle bends are used at all four ports to facilitate the adapters' connection.

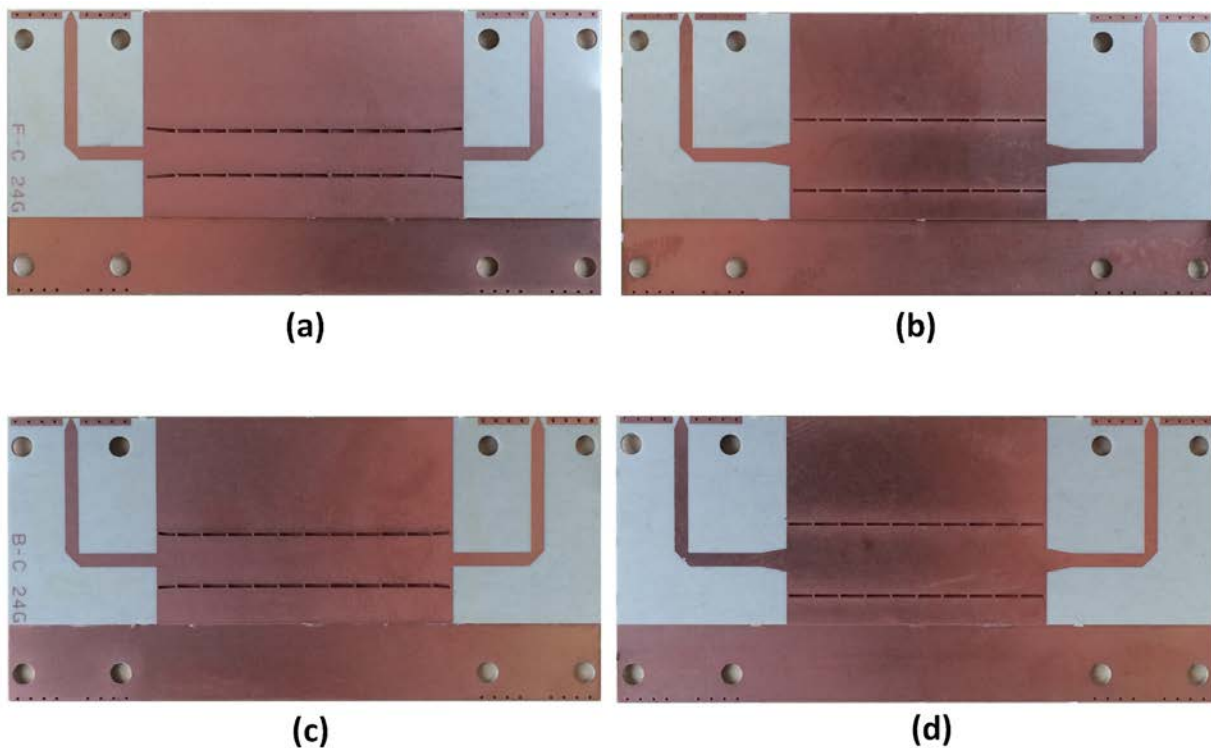
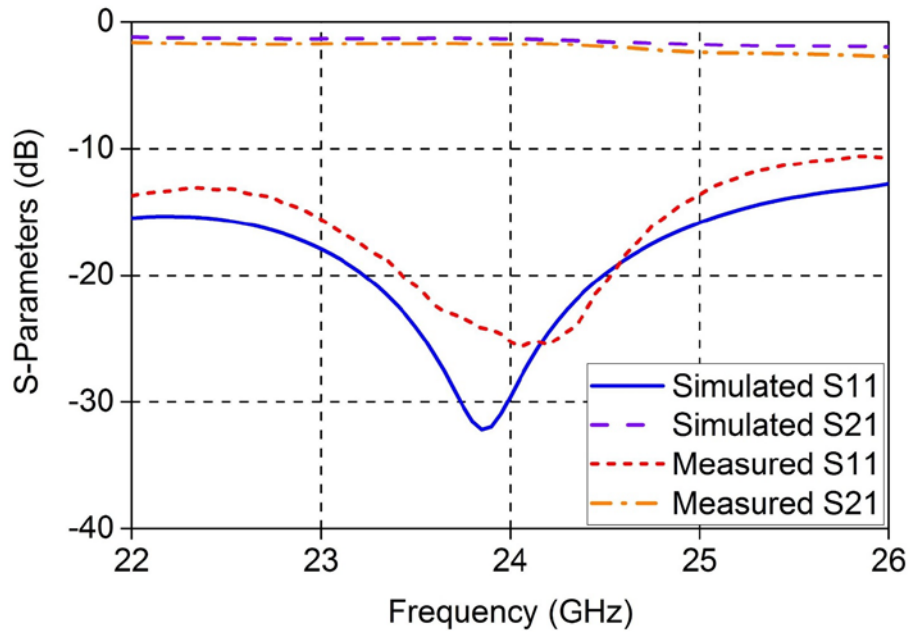
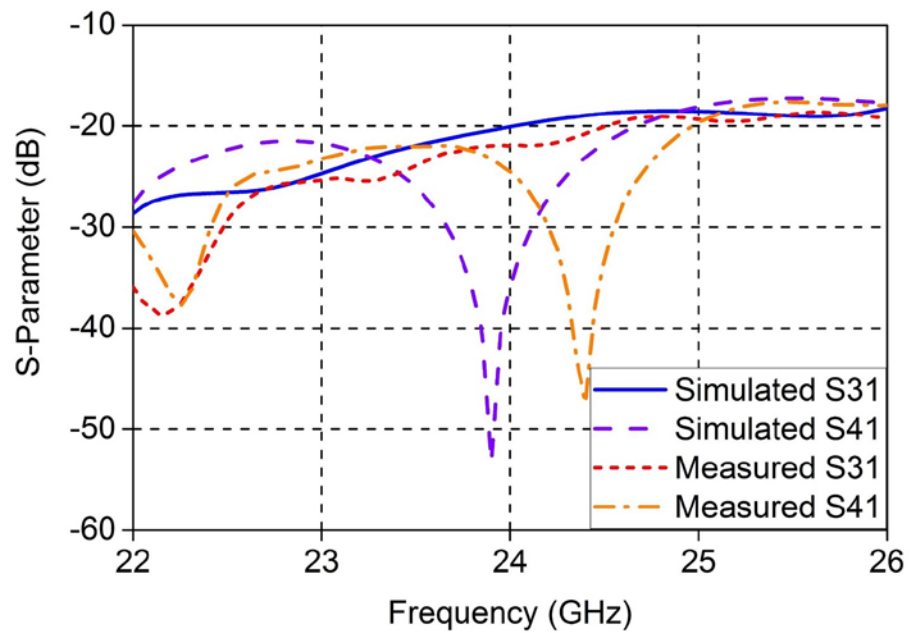


Figure 6.2: Pictures of fabricated forward and backward directional couplers: (a-b) top and bottom view of forward directional coupler, (c-d) top and bottom view of backward directional coupler.

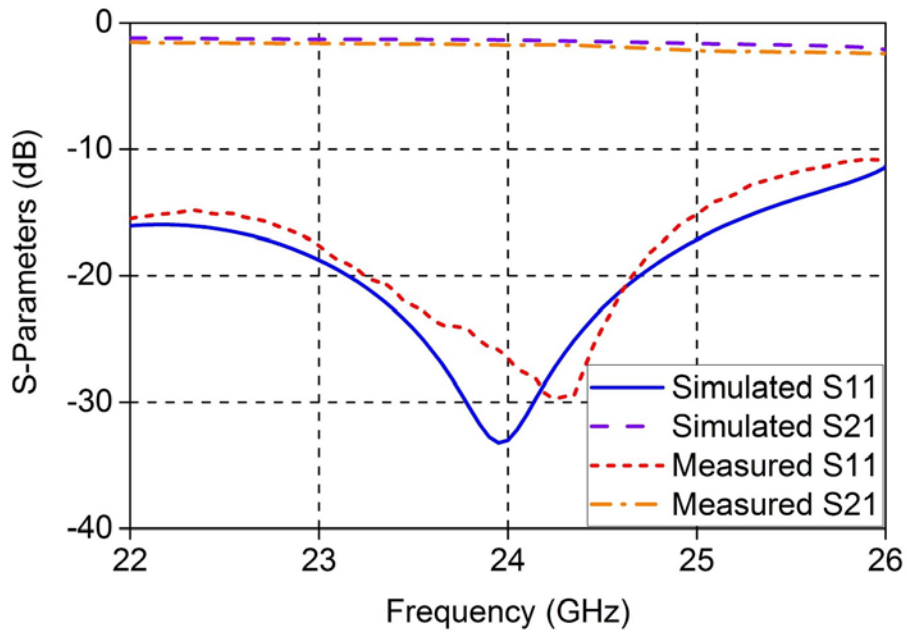


(a)

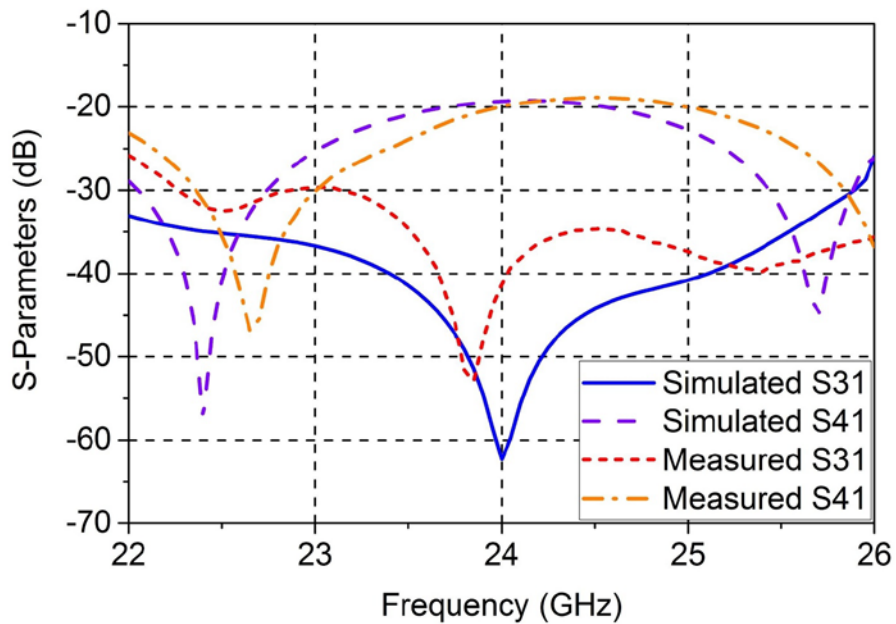


(b)

Figure 6.3: Measured and simulated forward directional coupler: (a) return loss (S11) and insertion loss (S21), (b) isolation (S31) and coupling (S41).



(a)



(b)

Figure 6.4: Measured and simulated backward directional coupler: (a) return loss (S11) and insertion loss (S21), (b) isolation (S31) and coupling (S41).

Measured and simulated results of the forward directional coupler are compared in Figure 6.3, where good matching (< -20 dB) is achieved at the operation frequency of 24 GHz. The -20 dB coupling and maximum isolations of -47 dB is achieved in measurement for the forward directional coupler.

Measured and simulated results of the backward directional coupler are compared in Figure 6.4, where good matching (< -20 dB) is achieved at the operation frequency of 24 GHz. The -20 dB coupling and maximum isolations of -52 dB is achieved in measurement for the forward directional coupler.

In both the forward and backward directional coupler measurements, observable differences are exhibited. The difference between the measurement and simulation is mainly caused by the tolerance issue in the double layer fabrication process, where the two layers are glued together under a high pressure. The existence of the glue and possibly a small air gap in between the two layers will increase the transmission loss and slightly change the actual permittivity of substrate. Therefore, in comparison, higher insertion losses and slight frequency shift are observed in both coupler measurements.

6.2 Balanced Antipodal Linear Tapered Slot Antenna

In modern microwave and mmW applications such as satellite communication, radar detection, remote sensing and microwave imaging, the stringent antenna performance requirements of wide bandwidth, high gain and low cross-polarization are usually desired [58]. Tapered slot antenna (TSA) [59], as an end-fire radiation antenna, is well-known for its high gain and wide bandwidth, which makes it very popular for the aforementioned applications. Different TSAs have been reported based on their taper shape, such as linearly tapered slot antenna (LTSA) [60], exponentially tapered slot antenna (Vivaldi) [61] and other non-linearly tapered slot antennas [62]. For different TSA, the tapers can be placed on either the same or the opposite side of substrate for different feeding networks. When the tapers are on the opposite side of the substrate, the antipodal antennas are realized such as antipodal Vivaldi antenna [63] and antipodal linearly tapered slot antenna (ALTSA) [64].

Besides the performance requirements, the low fabrication cost and easy antenna integration with circuits are also strongly desired in antenna designs. As frequency increases into mmW band,

the efficiency of planar transmission lines such as microstrip line and coplanar waveguide suffers from serious losses especially at bends and discontinuities [65]. Although the classical waveguide technology is low in loss at mmW frequency, it is not suitable for low cost fabrication, and is generally bulky and difficult for integration. To solve this issue, the concept of substrate integrated circuits (SICs) was proposed in [65], which bridges the performance gap between the planar transmission line and waveguide. The SICs inherit the advantages of not only the waveguides such as low loss, but also the planar transmission lines such as low cost and easy-to-integrate.

In this section, a balanced ALTSA is proposed, together with a multi-layer feeding network using SICs technology. The proposed feeding ensures the required out-of-phase characteristic over broadband range and allows the integrability of the antenna with planar circuits and components. This antenna not only inherits the advantages of conventional ALTSA, but also shows an improved cross-polarization suppression.

6.2.1 Balanced ALTSA Design

For all kinds of ALTSA, the antipodal nature of the antenna gives rise to a high level of cross-polarization, especially at millimeter-wave frequencies. Because the metal tapers reside on the opposite side of substrate with certain thickness, the excited E -field is tilted from the horizontal plane at the end of the antenna opening as shown in Figure 6.5 (a). After decomposition of the tilted E -field, the horizontal component is the co-polarization, while the vertical component is the undesired cross-polarization. To mitigate this cross-polarization, balanced structure can be used due to its symmetrical nature [66]. In our case, an extra layer of symmetrical ALTSA is added on top of a conventional one to form a balanced structure as shown in Figure 6.5 (b). In the balanced structure, the two decomposed horizontal E -field components are in the same direction and add up to each other, while the two decomposed vertical E -field components are in the opposite direction and cancel each other. The resulting E -field at the end of the slot is now oriented purely in the horizontal direction, completely eliminating the cross-polarization by theory.

Based on this principle, a double layer balanced ALTSA is designed for the cross-polarization suppression (shown in Figure 6.6). The ALTSA performance is sensitive to the choice of substrate thickness and its dielectric permittivity the antenna constructed upon as discussed in [67]. In the proposed antenna, two layers of substrate with relative permittivity of 2.94 and thickness of 0.508 mm are used. The detailed dimensions of the antenna are listed in Table 6.2.

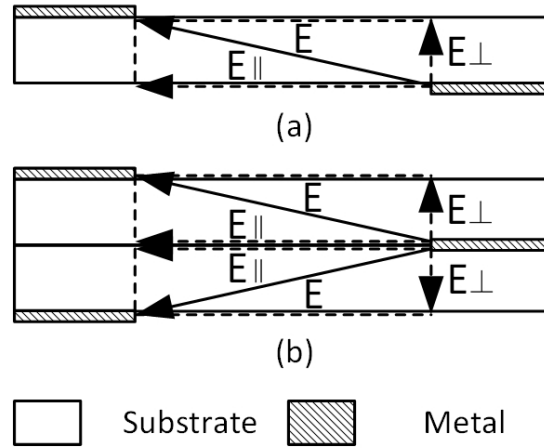


Figure 6.5: E -field distribution at the cross section: (a) conventional ALTSA, (b) balanced ALTSA.

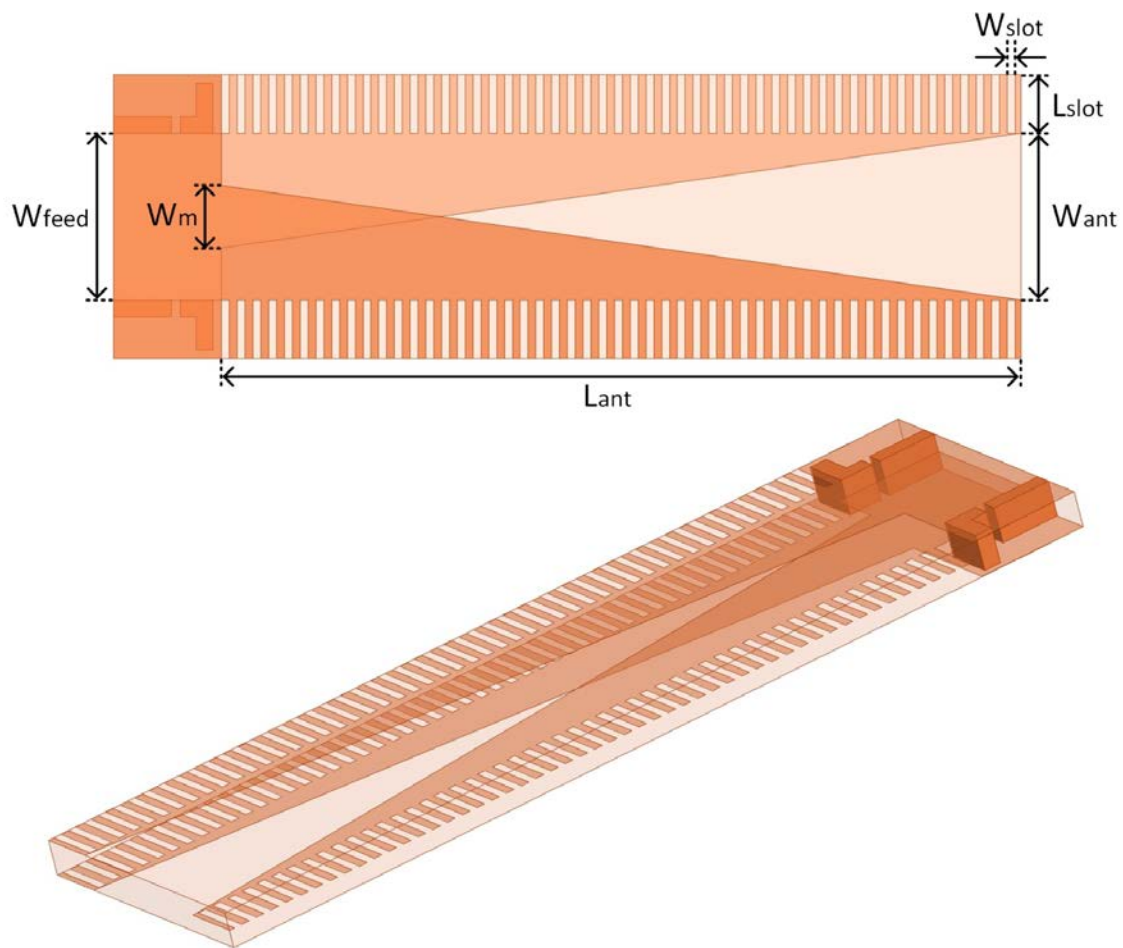


Figure 6.6: Top and 3D view of the proposed balanced ALTSA.

Table 6.2: Dimensions of balanced ALTSA.

W_{ant}	L_{ant}	W_{slot}	L_{slot}	W_m	W_{feed}
5 mm	24 mm	0.24 mm	1.75 mm	1.87 mm	5 mm

The antenna is fed by two identical SIWs with equal power magnitude and opposite E -field orientation. The antenna taper metallization on the top and bottom surfaces are flared in one direction, while the taper metallization in the middle is flared in the opposite direction to form the double layer tapered slots. Because the SIW feed and antenna tapering structure have different impedances and modes, a matching is needed to provide a smooth power transition. In this antenna, the overlap of the middle and two surface tapers (W_m in Figure 6.6) is used for matching.

Furthermore, the corrugation structure is used at the outer edge of all the three tapers to reduce the antenna size, as well as improve the gain and side lobe performance [67]. The length of slot is designed to be around a quarter wavelength in the dielectric substrate, and the width of slot is constrained by the fabrication process in our laboratory, where the smallest size is used here.

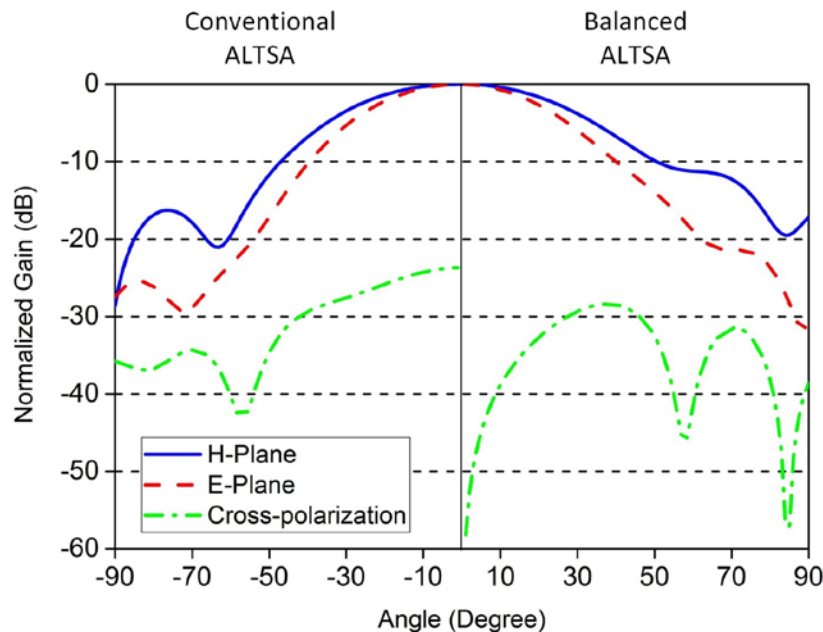


Figure 6.7: Simulated radiation patterns and cross-polarizations of conventional and balanced ALTSA at 28 GHz.

Figure 6.7 shows the comparison of simulated radiation pattern and cross-polarization of the proposed balanced ALTSA and its conventional ALTSA counterpart. Both the antennas have the same parameters, where the balanced antenna consists of two ALTSA with one stacking on top of the other and the middle taper coincides with each other. In comparison the balanced ALTSA achieves a further cross-polarization suppression of 35 dB at 0 degree compared to the cross-polarization of the conventional one, demonstrating the effectiveness of the balanced structure for cross-polarization suppression. For the same antenna length, the simulated gain for the conventional and balanced ALTSA are 12.8 dBi and 11.6 dBi, respectively.

6.2.2 Integrated Feeding Network Design

The balanced stripline antipodal antennas in [68] [69] are excited by connector soldered to the two sides of the sheet. The axial pin is connected to the central conductor and the ground to the two external ones. The coaxial connector and involved mechanical attachment parts complicate the fabrication process and on the other hand don't allow the integration of the antenna with other front-end passive and active components. Transition to CPW or microstrip lines is required to overcome those limitations.

To feed the antenna, a double layer SIW antenna feeding structure need to be further transitioned to the single layer transmission line for adaptor connection, where the grounded coplanar waveguide (GCPW) is used here for its low radiation loss. This transition is realized by first transform the GCPW to the SICL, and then further transform the SICL to the double layer SIW.

The first part of the transition is achieved by tapering out the inner conductor and vias of the GCPW to match the impedance of SICL. The vias connecting the top and bottom ground planes are used in the GCPW to suppress the higher order modes and improve the mode matching between the GCPW and the SICL. The width of the SICL is selected so that the higher order modes will not appear within the band of operation.

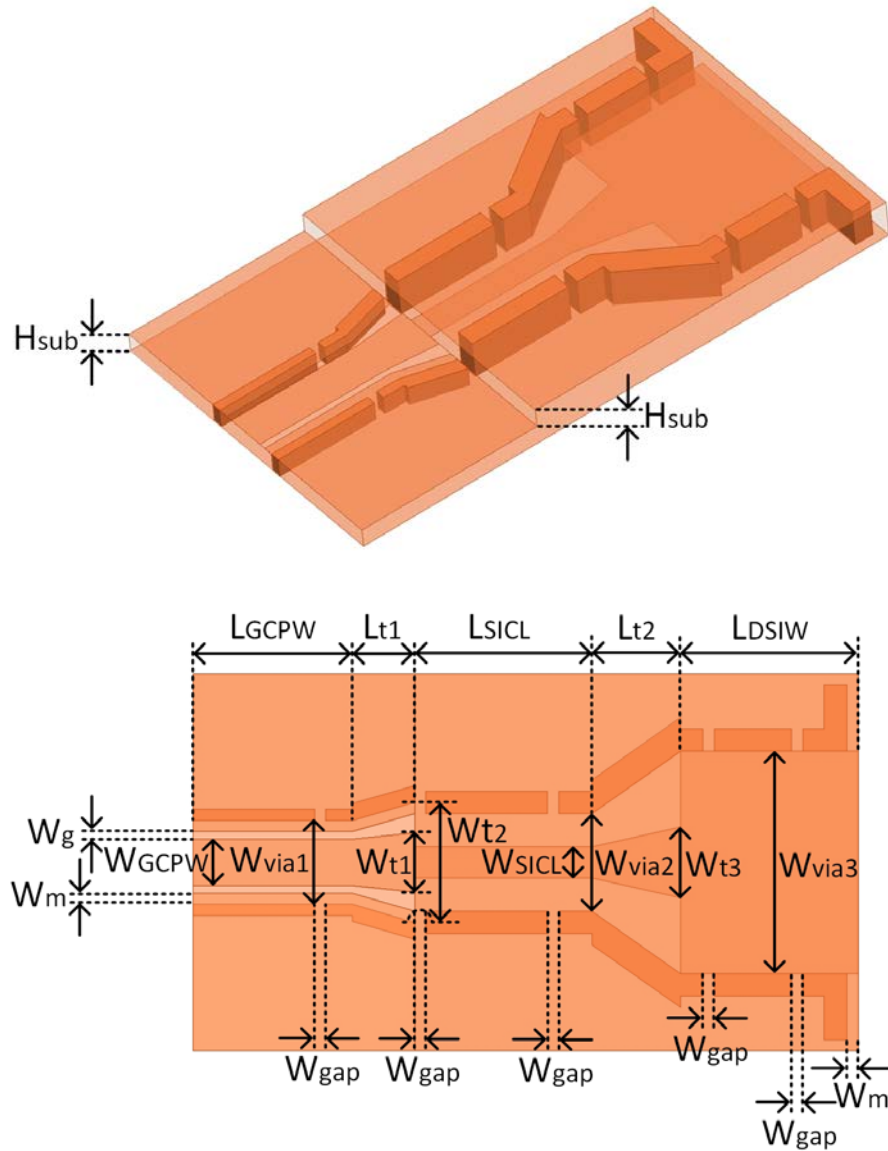


Figure 6.8: Top and 3D view of the proposed transition for antenna feeding.

The second part of the transition is achieved by tapering out the inner conductor and vias of SICL to match both the impedance and mode to the double layer SIW. This part acts as out of phase power divider with SICL as input and two SIW as outputs. Because the E -fields in the SICL point from inner conductor to outer conductor, the fields at top and bottom have opposite orientation. When equally divided into the top and bottom SIW, the orientation of the E -fields in the two SIW are intrinsically in opposite direction.

The proposed transition is shown in Figure 6.8, and the detailed dimensions of the transition are listed in Table 6.3. The simulated transition performance is shown in Figure 6.9, where the equal power division and 180 phase difference is achieved by the transition within the operation band from 22 to 34 GHz with perfect power division equality. This transition can be used as wideband out of phase two-way power divider.

Table 6.3: Dimensions of CPW to double layer SIW transition.

W_g	W_m	W_{GCPW}	W_{via1}	W_{t1}	W_{t2}
0.16 mm	0.25 mm	1.06mm	1.89 mm	1.35 mm	2.71 mm
W_{SIWL}	W_{via2}	W_{t3}	W_{via3}	W_{gap}	L_{GCPW}
0.7 mm	2.2 mm	1.6 mm	5 mm	0.25 mm	3.6 mm
L_{t1}	L_{SIWL}	L_{t2}	L_{DSIW}		
1.4 mm	4 mm	2 mm	4 mm		

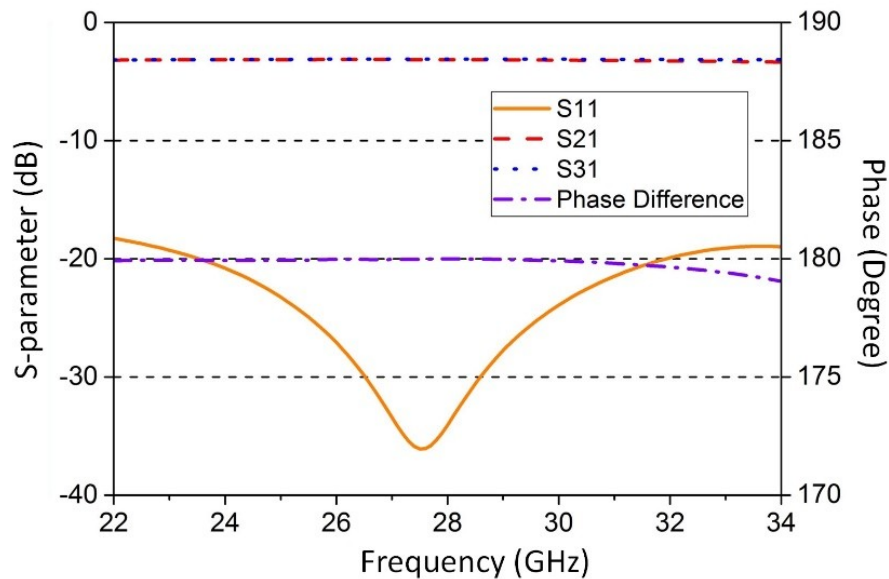
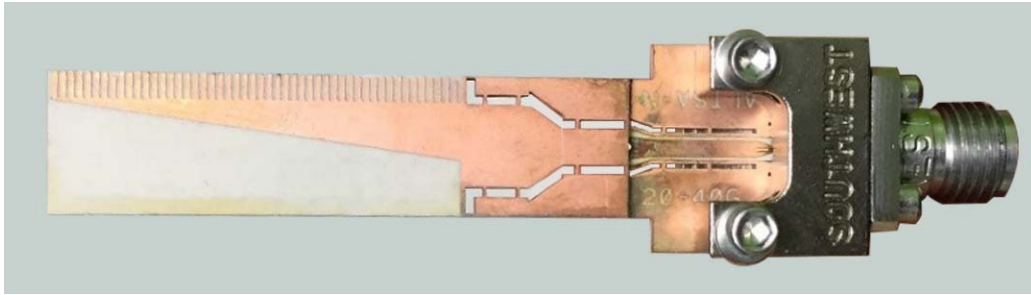


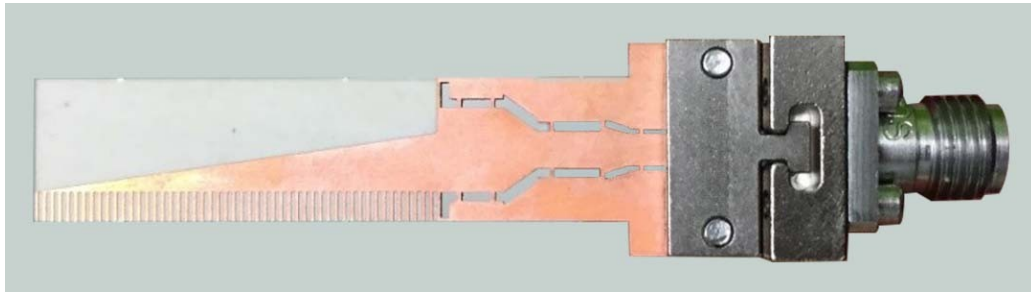
Figure 6.9: Simulated S-parameters and phase difference of the proposed transition.

6.2.3 Fabrication and Measurement

Combining the transition and antenna, the fabricated balanced ALTSA is shown in Figure 6.10. In picture, the GCPW feeding line is connected to a Southwest end launch connector for the measurement.



(a)



(b)

Figure 6.10: Top (a) and bottom (b) view of the fabricated balanced ALTSA.

The simulated and measured return losses of the proposed antenna are shown in Figure 6.11. Good return loss is achieved in the measurement within the band of operation, and it agrees well with the simulation result.

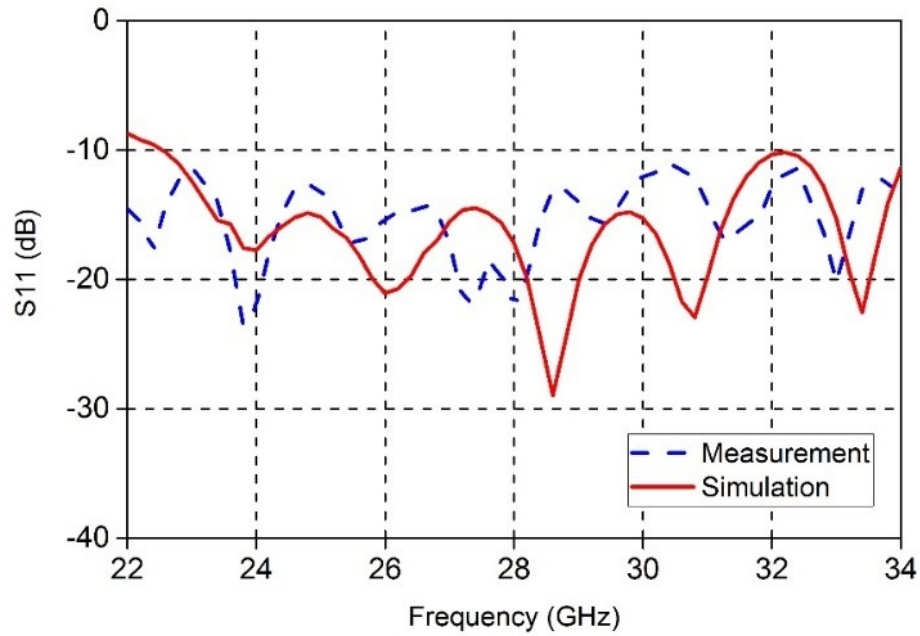


Figure 6.11: Measured and simulated antenna return losses.

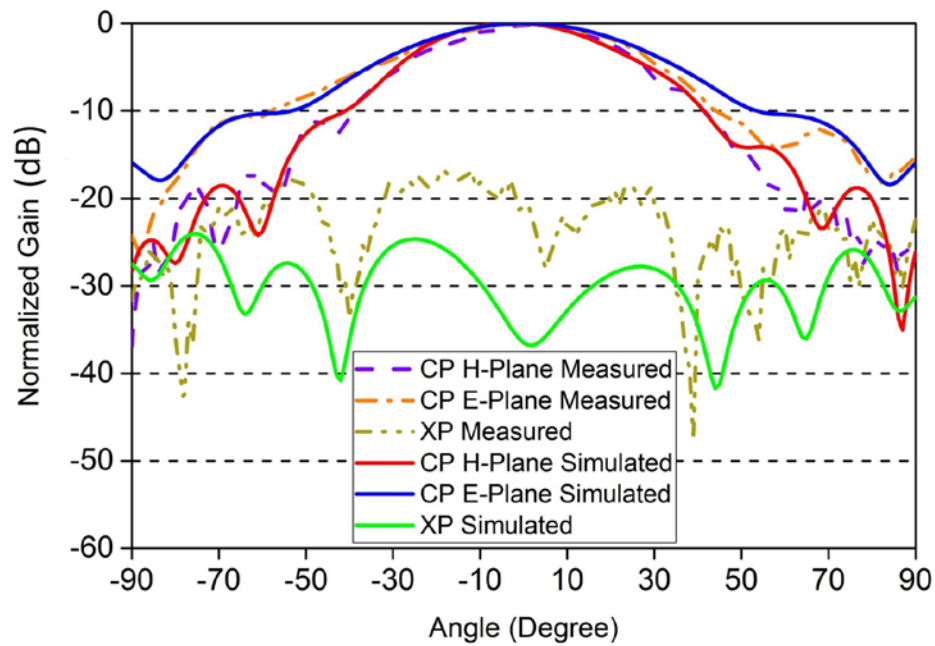


Figure 6.12: Measured and simulated radiation patterns and cross-polarizations at 28 GHz.

The simulated and measured antenna E -plane and H -plane radiation patterns, as well as the cross-polarization at 28 GHz are shown in Figure 6.12. The measured gain is 10.32 dBi and the 3 dB beamwidth is 45 degrees for the E -plane and 48 degrees for the H -plane. It can be seen that the measured results are in good agreement with the simulated ones for both E and H -plane radiation patterns. The cross-polarization suppression in the antenna propagation direction (around 0 degree) is observed in both measurement and simulation, where the measured cross-polarization is 28 dB lower than the co-polarization. The cross-polarization difference between measurement and simulation is mainly attributed to the radiation leakage from non-SIW part of feeding network and end launch connector, which alter the performance of the balanced ALTSA in term of cross-polarization. Furthermore, the antenna is characterized in a compact range anechoic chamber, and the energy diffracted on the different part of the measurement setup may further deteriorate the cross-polarization performance.

6.3 Conclusion

In this chapter, the VPC directional coupler is first proposed using double layer substrate integration technique. Compared to its conventional counterpart, the proposed coupler uses variable waveguide propagation constants as an extra degree of design freedom to achieve the required signal addition and cancelation. The operation principle is mathematically formulated and a step-by-step design methodology is presented. Two double layer two-hole SIW couplers, namely one forward directional coupler and one backward directional coupler, are fabricated to validate the proposed concept. A coupling of -20 dB is achieved in both couplers and the maximum isolation of -47 dB and -52 dB are obtained by the forward and backward structures respectively.

Furthermore, a balanced ALTSA using two layers of substrate is also proposed with improved cross-polarization performance. This antenna consists of two conventional ALTSAs with one stacked on top of the other, forming a balanced structure. By arranging the middle tapers in the same direction and coinciding with each other, the field components corresponding to the cross-polarization can be canceled, thereby improving the polarization purity. The antenna feeding network from the single layer transmission line to the double layer radiation structure is also presented. Measurement is in good agreement with simulation for both the return loss from 22 to 34 GHz, and the E and H -plane radiation patterns at 28 GHz. The measured antenna gain is 10.32 dBi, and the measured cross-polarization is 28 dB lower than the co-polarization. The proposed

antenna demonstrates the potential of using balanced structure in the ALTSA design for cross-polarization suppression.

CHAPTER 7 CONCLUSION AND FUTURE WORK

7.1 Conclusion

This PhD thesis proposed and investigated two types of broadband or multi-band hardware development platform, namely MCW and HMCW, respectively. Both hardware platforms can be deployed over an unprecedented wide UHF-to-mmW frequency range, consisting of an inner waveguide suitable for high frequency operation and an outer waveguide suitable for low frequency operation. For the MCW, the inner waveguide operates with the TE_{10} mode and the outer waveguide operates with the TEM mode. By contrast, the inner waveguide of the HMCW operates with the quasi- $TE_{0.5-0}$ mode and the outer waveguide operates with quasi-TEM mode. Various feeding networks and circuits are developed on the MCW or HMCW platforms, through the exploitation of their different properties.

The MCW and HMCW based circuits were fabricated on a triple layer PCB structure using the multilayer substrate integration techniques. In fabrication, the three layers of substrates are glued together under high pressure, where the effects of the existing glue and possibly small air gap in between the layers will introduce extra losses in measurement. Due to the uncertainties of the glue and air gap distributions between the layers, it's very difficult to model these multilayer fabrication effects accurately, and therefore are considered ideal in simulation. In comparison of simulation and measurement results, an extra insertion loss around 0.2 dB is usually observed in measurement, and this empirical value also slightly varies as the geometry of circuit varies.

The original contributions and highlights of this thesis work are summarized as follows:

- The MCW is proposed, and its waveguide parameters of the inner and outer waveguides are theoretically analyzed, including propagation constants, impedances, losses, and higher order mode cutoff frequencies, etc. Equations are summarized for each waveguide parameter of the inner and outer waveguides of MCW, respectively.
- The fabrication process of MCW is provided, which uses three layers of RT/duroid 6002 substrates with the multilayer substrate integration technique in our lab. The fabrication requirements and limitations are presented, and the MCW design rules based on the fabrication process are discussed, from the substrate selection to the choice of operation frequency bands.

- Two types of joint feeding networks for the MCW measurement and integration are developed. In both the type I and type II joint feeding networks, the triple layer MCW is transitioned into single layer microstrip lines, respectively. Type I joint feeding network exhibits good matching from 7.6 GHz to 10.6 GHz for outer waveguide and from 26 GHz to 38.2 GHz for inner waveguide respectively. Type II joint feeding network exhibits good matching from 6.9 GHz to 11.8 GHz for outer waveguide and from 13.5 GHz to 24.1 GHz for inner waveguide respectively.
- A MCW directional coupler is developed, where the mode conversion between the inner and outer waveguide during coupling is studied. Due to the dual propagation constants nature, equations specifically for the MCW are derived for the coupler in achieving the required signal addition and cancelation. A MCW backward directional coupler at 10 GHz is fabricated, and the desired coupling power of -20 dB and the maximum isolation of -50 dB are obtained in the measurement.
- A MCW based dual-mode filter is developed using the two degenerate modes of the outer waveguide higher order modes. The inner waveguide is used as the input and output feedings, and the outer waveguide as the dual-mode resonator. Two transmission poles and one finite transmission zero are realized by the filter, where the two transmission poles are used to control the filter bandwidth, and the finite transmission zero is used to improve the out of band selectivity. Two types of dual-mode filter are designed at 10 GHz with 2% fractional bandwidth, where Type I filter exhibiting a transmission zero on the left and type II filter on the right of the passband.
- A MCW based planar magic tee is developed, which uses the inner waveguide of MCW as the summation port, and the outer waveguide of MCW as the difference port in the operation. The outer waveguide signal is equally divided out of phase and the inner waveguide signal is equally divided in phase at the two output ports, respectively. The MCW magic tee is fabricated and measured at 10 GHz, and good matching of -21.7 dB and -25.4 dB are achieved for the difference and summation ports, respectively, with a difference-summation port isolation of -27.4 dB.
- The HMCW is proposed for the size reduction with its inner and outer waveguides each working in half-mode compared to the MCW, respectively. The HMCW's fundamental

modes of quasi- $TE_{0.5-0}$ mode in the inner waveguide and quasi-TEM mode in the outer waveguide are analyzed in terms of impedance, loss and propagation characteristics, under half-mode operation. Compared to its full-size counterpart MCW, the HMCW only occupies about half the space with comparable loss performance. A joint feeding network for the HMCW is also developed, which can simultaneously excite the half-mode operation of inner and outer waveguides. In measurement, good matching is achieved from 4.4 GHz to 11.2 GHz for the outer waveguide at low frequency, and from 18.6 GHz to 32.6 GHz for the inner waveguide at high frequency, respectively.

- Two double layer VPC directional couplers at 24 GHz are developed using variable waveguide propagation constants as an extra degree of freedom in design. By properly choosing the value of two propagation constants in coupler design, the desired signal addition and cancelation can be achieved for both the forward and the backward operations. In measurement, the power coupling of -20 dB is achieved for both couplers and the maximum isolation of -47 dB and -52 dB are obtained by the forward and backward couplers, respectively.
- A double layer balanced AL TSA antenna is developed with improved cross-polarization performance. The cross-polarization is suppressed by stacking two conventional AL TSAs on top of each other, forming a balanced structure. An integrated feeding network is also presented allowing the antenna excitation with a CPW feeding. Good matching is achieved from 22 GHz to 34 GHz, and at 28 GHz the measured antenna gain is 10.32 dBi, and cross-polarization is suppressed by 28 dB.

7.2 Future Work

The research contributions summarized in this thesis can be further extended in the following mentioned areas:

- The MCW and HMCW based circuits in this thesis are all fabricated using multilayer substrate integration technique in our lab. Although this multilayer fabrication process is low in cost, good in robustness and loss performance, it also has limitations in terms of circuit dimensions, material properties, etc. In the future development, the concept of MCW

and HMCW shall not be limited to the multilayer fabrication process, and other available technologies such as LTCC, RF CMOS and 3D printing can also be explored.

- The dual propagation constants property of the MCW and HMCW can be further explored for future dual-band circuit development. Dual-band passive components such as dual-band delay lines and phase shifters, dual-band couplers, dual-band power dividers and combiners can be developed.
- Compared to the fully enclosed structure of MCW, the HMCW is a partially open structure in achieving the size reduction. On one hand, to avoid potential power leakage from the opening, the HMCW requires extra considerations in design and has reduced operation bandwidth for the inner waveguide compared to MCW. On the other hand, the partially open structure of HMCW can also be used in a desirable way for the design of coupling or radiating structures. By properly designing the structure of opening, the power leakage can be controlled in a manageable way that power coupling of various levels can be realized precisely. Also, this partially open structure of HMCW can be used as radiating elements, where leaky wave antennas or antenna arrays can be developed.
- In this thesis, various transitions and joint feeding networks of the MCW and HMCW are developed. In these feeding networks, the MCW and HMCW are transitioned to microstrip lines for the convenience of measurement in our lab. In the future, the hybrid circuits using the combination of MCW and HMCW can be explored, where the transitions to waveguide, coaxial line, and from MCW to HMCW need to be developed.

REFERENCES

- [1] C. Cox, *An introduction to LTE: LTE, LTE-advanced, SAE and 4G mobile communications*. John Wiley & Sons, 2012.
- [2] Z. Pi and F. Khan, "An introduction to millimeter-wave mobile broadband systems," *IEEE communications magazine*, vol. 49, no. 6, 2011.
- [3] D. Deslandes and K. Wu, "Integrated microstrip and rectangular waveguide in planar form," *IEEE Microwave and Wireless Components Letters*, vol. 11, no. 2, pp. 68-70, 2001.
- [4] H. Tang, W. Hong, Z. Hao, J. Chen, and K. Wu, "Optimal design of compact millimetre-wave SIW circular cavity filters," *Electronics Letters*, vol. 41, no. 19, pp. 1068-1069, 2005.
- [5] M. Abdolhamidi and M. Shahabadi, "X-band substrate integrated waveguide amplifier," *IEEE microwave and wireless components letters*, vol. 18, no. 12, pp. 815-817, 2008.
- [6] D. Deslandes, "Substrate integrated waveguide leaky-wave antenna: Concept and design considerations," in *2005 Asia-Pacific Microwave Conf. Proc., Dec., 2005*, vol. 1, pp. 346-349.
- [7] F. Gatti, M. Bozzi, L. Perregrini, K. Wu, and R. G. Bosisio, "A novel substrate integrated coaxial line (SICL) for wide-band applications," in *Microwave Conference, 2006. 36th European*, 2006, pp. 1614-1617: IEEE.
- [8] Y. Zhang and Z. Song, "A compact substrate integrated coaxial line bandpass filter with extended rejection bandwidth," *Microwave and Optical Technology Letters*, vol. 56, no. 2, pp. 415-418, 2014.
- [9] P. Chu *et al.*, "Wide stopband bandpass filter implemented with spur stepped impedance resonator and substrate integrated coaxial line technology," *IEEE Microwave and Wireless Components Letters*, vol. 24, no. 4, pp. 218-220, 2014.
- [10] P. Chu, W. Hong, K. Wu, J. Chen, and H. Tang, "A miniaturized bandpass filter implemented with substrate integrated coaxial line," *Microwave and Optical Technology Letters*, vol. 55, no. 1, pp. 131-133, 2013.
- [11] S. Jun-Yu *et al.*, "High-directivity single-and dual-band directional couplers based on substrate integrated coaxial line technology," in *Microwave Symposium Digest (IMS), 2013 IEEE MTT-S International*, 2013, pp. 1-4: IEEE.
- [12] W. Liang and W. Hong, "Substrate integrated coaxial line 3 dB coupler," *Electronics Letters*, vol. 48, no. 1, pp. 35-36, 2012.
- [13] Q. Liu *et al.*, "A substrate integrated waveguide to substrate integrated coaxial line transition," *Progress In Electromagnetics Research C*, vol. 36, pp. 249-259, 2013.
- [14] J. Guo, T. Djerafi, and K. Wu, "Mode Composite Waveguide," *IEEE Transactions on Microwave Theory and Techniques*, vol. 64, no. 10, pp. 3187-3197, 2016.
- [15] J. Guo and K. Wu, "Joint feeding network for mode composite waveguide," in *Microwave Symposium (IMS), 2017 IEEE MTT-S International*, 2017, pp. 1274-1277: IEEE.
- [16] J. Guo and K. Wu, "Mode Composite Waveguide Directional Coupler," in *Accepted for publication in 2018 IEEE MTT-S International Wireless Symposium (IWS)*, 2018: IEEE.

- [17] J. Guo and K. Wu, "Mode composite waveguide filter with dual-mode operation," in *Microwave Symposium (IMS), 2017 IEEE MTT-S International*, 2017, pp. 1072-1075: IEEE.
- [18] J. Guo and K. Wu, "Half-Mode Composite Waveguide," *IEEE Transactions on Microwave Theory and Techniques*, 2018.
- [19] J. Guo and K. Wu, "Variable propagation constant directional coupler," *Electronics Letters*, vol. 53, no. 6, pp. 419-421, 2017.
- [20] J. Guo, T. Djerafi, and K. Wu, "Balanced Corrugated Antipodal Linear Tapered Slot Antenna with Integrated Feeding for Cross-Polarization Suppression," in *Accepted for publication in 17th International Symposium on Antenna Technology and Applied Electromagnetics (ANTEM), 2016* 2018: IEEE.
- [21] T.-S. Chen, "Determination of the capacitance, inductance, and characteristic impedance of rectangular lines," *IRE Transactions on Microwave Theory and Techniques*, vol. 8, no. 5, pp. 510-519, 1960.
- [22] K. Lau, "Loss calculations for rectangular coaxial lines," in *IEE Proceedings H-Microwaves, Antennas and Propagation*, 1988, vol. 135, no. 3, pp. 207-209: IET.
- [23] D. M. Pozar, *Microwave engineering*. John Wiley & Sons, 2009.
- [24] M. Bozzi, M. Pasian, and L. Perregrini, "Advanced modeling and design of substrate integrated waveguide components," in *Wireless Symposium (IWS), 2014 IEEE International*, 2014, pp. 1-4: IEEE.
- [25] N. Marcuvitz, *Waveguide handbook* (no. 21). Iet, 1951.
- [26] T.-H. Yang, C.-F. Chen, T.-Y. Huang, C.-L. Wang, and R.-B. Wu, "A 60GHz LTCC transition between microstrip line and substrate integrated waveguide," in *Microwave Conference Proceedings, 2005. APMC 2005. Asia-Pacific Conference Proceedings, 2005*, vol. 1, p. 3 pp.: IEEE.
- [27] C.-k. Yau, T.-Y. Huang, T.-M. Shen, H.-Y. Chien, and R.-B. Wu, "Design of 30GHz transition between microstrip line and substrate integrated waveguide," in *Microwave Conference, 2007. APMC 2007. Asia-Pacific, 2007*, pp. 1-4: IEEE.
- [28] E. D. Caballero, A. B. Martinez, H. E. Gonzalez, O. M. Belda, and V. B. Esbert, "A novel transition from microstrip to a substrate integrated waveguide with higher characteristic impedance," in *Microwave Symposium Digest (IMS), 2013 IEEE MTT-S International*, 2013, pp. 1-4: IEEE.
- [29] D. Deslandes, "Design equations for tapered microstrip-to-substrate integrated waveguide transitions," in *Microwave Symposium Digest (MTT), 2010 IEEE MTT-S International*, 2010, pp. 704-707: IEEE.
- [30] K. Song and Q. Xue, "Ultra-wideband out-of-phase power divider using multilayer microstrip-slotline coupling structure," *Microwave and Optical Technology Letters*, vol. 52, no. 7, pp. 1591-1594, 2010.
- [31] L. Xiao, H. Peng, and T. Yang, "Compact ultra-wideband in-phase multilayer power divider," *Progress In Electromagnetics Research Letters*, vol. 48, pp. 33-37, 2014.

- [32] A. Abbosh, "Ultra wideband inphase power divider for multilayer technology," *IET microwaves, antennas & propagation*, vol. 3, no. 1, pp. 148-153, 2009.
- [33] Y. Cassivi, D. Deslandes, and K. Wu, "Substrate integrated waveguide directional couplers," 2002.
- [34] T. Djerafi and K. Wu, "Super-compact substrate integrated waveguide cruciform directional coupler," *IEEE Microwave and Wireless Components Letters*, vol. 17, no. 11, pp. 757-759, 2007.
- [35] Z. Pourgholamhossein, R. Safian, and H. Pourghassem, "Wideband double layer substrate integrated waveguide directional coupler," in *Telecommunications (IST), 2010 5th International Symposium on*, 2010, pp. 328-331: IEEE.
- [36] P. Chen, G. Hua, D. T. Chen, Y. C. Wei, and W. Hong, "A double layer crossed over substrate integrated waveguide wide band directional coupler," in *Microwave Conference, 2008. APMC 2008. Asia-Pacific*, 2008, pp. 1-4: IEEE.
- [37] J. R. Montejo-Garai and J. Zapata, "Full-wave design and realization of multicoupled dual-mode circular waveguide filters," *IEEE transactions on microwave theory and techniques*, vol. 43, no. 6, pp. 1290-1297, 1995.
- [38] J. Lee, M. S. Uhm, and I.-B. Yom, "A dual-passband filter of canonical structure for satellite applications," *IEEE Microwave and wireless components letters*, vol. 14, no. 6, pp. 271-273, 2004.
- [39] J.-F. Liang, X.-P. Liang, K. A. Zaki, and A. E. Atia, "Dual-mode dielectric or air-filled rectangular waveguide filters," *IEEE transactions on microwave theory and techniques*, vol. 42, no. 7, pp. 1330-1336, 1994.
- [40] M. Guglielmi, P. Jarry, E. Kerherve, O. Roquebrun, and D. Schmitt, "A new family of all-inductive dual-mode filters," *IEEE Transactions on Microwave Theory and Techniques*, vol. 49, no. 10, pp. 1764-1769, 2001.
- [41] X. Chen, W. Hong, T. Cui, Z. Hao, and K. Wu, "Symmetric dual-mode filter based on substrate integrated waveguide (SIW)," *Electrical Engineering*, vol. 89, no. 1, pp. 67-70, 2006.
- [42] C.-Y. Chang and W.-C. Hsu, "Novel planar, square-shaped, dielectric-waveguide, single-, and dual-mode filters," *IEEE Transactions on Microwave Theory and Techniques*, vol. 50, no. 11, pp. 2527-2536, 2002.
- [43] Q. F. Wei, Z. F. Li, and H. G. Shen, "Dual-mode filters based on substrate integrated waveguide by multilayer LTCC technology," *Microwave and Optical Technology Letters*, vol. 50, no. 11, pp. 2788-2790, 2008.
- [44] U. Kongpop, E. J. Wollack, J. Papapolymerou, and J. Laskar, "A broadband planar magic-T using microstrip-slotline transitions," *IEEE Transactions on Microwave Theory and Techniques*, vol. 56, no. 1, pp. 172-177, 2008.
- [45] J. P. Kim and W. S. Park, "Novel configurations of planar multilayer magic-T using microstrip-slotline transitions," *IEEE transactions on microwave theory and techniques*, vol. 50, no. 7, pp. 1683-1688, 2002.

- [46] F. F. He, K. Wu, W. Hong, H. J. Tang, H. B. Zhu, and J. X. Chen, "A planar magic-T using substrate integrated circuits concept," *IEEE Microwave and wireless components letters*, vol. 18, no. 6, pp. 386-388, 2008.
- [47] W. Feng, W. Che, and K. Deng, "Compact planar magic-T using E-plane substrate integrated waveguide (SIW) power divider and slotline transition," *IEEE Microwave and wireless components letters*, vol. 20, no. 6, pp. 331-333, 2010.
- [48] M. Mansouree and A. Yahaghi, "Planar Magic-Tee Using Substrate Integrated Waveguide Based on Mode-Conversion Technique," *IEEE Microwave and Wireless Components Letters*, vol. 26, no. 5, pp. 307-309, 2016.
- [49] W. Hong *et al.*, "Half mode substrate integrated waveguide: A new guided wave structure for microwave and millimeter wave application," in *Infrared Millimeter Waves and 14th International Conference on Terahertz Electronics, 2006. IRMMW-THz 2006. Joint 31st International Conference on*, 2006, pp. 219-219: IEEE.
- [50] J. Attari, T. Djerafi, and K. Wu, "A compact 94 GHz image substrate integrated non-radiative dielectric (iSINRD) waveguide cruciform coupler," *IEEE Microwave and Wireless Components Letters*, vol. 23, no. 10, pp. 533-535, 2013.
- [51] H. A. Haus and J. R. Melcher, *Electromagnetic fields and energy*. Prentice Hall, 1989.
- [52] Q. Lai, C. Fumeaux, W. Hong, and R. Vahldieck, "Characterization of the propagation properties of the half-mode substrate integrated waveguide," *IEEE Transactions on Microwave Theory and Techniques*, vol. 57, no. 8, pp. 1996-2004, 2009.
- [53] H. B. Palmer, "The capacitance of a parallel-plate capacitor by the Schwartz-Christoffel transformation," *Electrical Engineering*, vol. 56, no. 3, pp. 363-368, 1937.
- [54] T. Sauer, "Numerical Analysis," *Upper Saddle River, NJ: Pearson Educ.*, pp. 230-235, 2006.
- [55] Q. Lai, C. Fumeaux, and W. Hong, "On the transition from radiating to guiding behavior of the half-mode substrate integrated waveguide," in *Microwave Conference Proceedings (APMC), 2010 Asia-Pacific*, 2010, pp. 1601-1604: IEEE.
- [56] W. Ma, K. Wu, W. Hong, and Y.-J. Cheng, "Investigations on half-mode substrate integrated waveguide for high-speed interconnect application," in *Art of Miniaturizing RF and Microwave Passive Components, 2008. IMWS 2008. IEEE MTT-S International Microwave Workshop Series on*, 2008, pp. 120-123: IEEE.
- [57] A. Doghri, T. Djerafi, A. Ghiotto, and K. Wu, "Substrate integrated waveguide directional couplers for compact three-dimensional integrated circuits," *IEEE Transactions on Microwave Theory and Techniques*, vol. 63, no. 1, pp. 209-221, 2015.
- [58] C. A. Balanis, *Modern antenna handbook*. John Wiley & Sons, 2011.
- [59] K. S. Yngvesson, T. Korzeniowski, Y.-S. Kim, E. L. Kollberg, and J. F. Johansson, "The tapered slot antenna-a new integrated element for millimeter-wave applications," *IEEE Transactions on Microwave Theory and Techniques*, vol. 37, no. 2, pp. 365-374, 1989.
- [60] S. Prasad and S. Mahapatra, "A new MIC slot-line aerial," *IEEE Transactions on Antennas and Propagation*, vol. 31, no. 3, pp. 525-527, 1983.

- [61] P. Gibson, "The vivaldi aerial," in *Microwave Conference, 1979. 9th European*, 1979, pp. 101-105: IEEE.
- [62] H. Sato, K. Sawaya, N. Arai, Y. Wagatsuma, and K. Mizuno, "Broadband FDTD analysis of fermi antenna with narrow width substrate," in *Antennas and Propagation Society International Symposium, 2003. IEEE*, 2003, vol. 1, pp. 261-264: IEEE.
- [63] E. Gazit, "Improved design of the Vivaldi antenna," in *IEE Proceedings H (Microwaves, Antennas and Propagation)*, 1988, vol. 135, no. 2, pp. 89-92: IET.
- [64] Z. C. Hao, W. Hong, J. X. Chen, X. P. Chen, and K. Wu, "A novel feeding technique for antipodal linearly tapered slot antenna array," in *Microwave Symposium Digest, 2005 IEEE MTT-S International*, 2005, p. 3 pp.: IEEE.
- [65] C. Yu Jian, W. Ke, and H. Wei, "Power Handling Capability of Substrate Integrated Waveguide Interconnects and Related Transmission Line Systems," *Advanced Packaging, IEEE Transactions on*, vol. 31, no. 4, pp. 900-909, 2008.
- [66] J. Langley, P. Hall, and P. Newham, "Balanced antipodal Vivaldi antenna for wide bandwidth phased arrays," *IEE Proceedings-Microwaves, Antennas and Propagation*, vol. 143, no. 2, pp. 97-102, 1996.
- [67] T. Djerafi and K. Wu, "Corrugated substrate integrated waveguide (SIW) antipodal linearly tapered slot antenna array fed by quasi-triangular power divider," *Progress In Electromagnetics Research C*, vol. 26, pp. 139-151, 2012.
- [68] J. Bourqui, E. C. Fear, and M. Okoniewski, "Traveling-wave antenna," ed: Google Patents, 2013.
- [69] A. Bayat and R. Mirzakhani, "A Parametric Study and Design of the Balanced Antipodal Vivaldi Antenna (BAVA)," in *PIERS Proceedings*, 2012, p. 778.